



# Chemical Vapor Deposition of Cuprous Halide Semiconductors and Polymer Dielectrics for Applications in Optoelectronics and Flexible Microelectronics

## Citation

Chang, Christina Marie. 2020. Chemical Vapor Deposition of Cuprous Halide Semiconductors and Polymer Dielectrics for Applications in Optoelectronics and Flexible Microelectronics. Doctoral dissertation, Harvard University, Graduate School of Arts & Sciences.

## Permanent link

<https://nrs.harvard.edu/URN-3:HUL.INSTREPOS:37365136>

## Terms of Use

This article was downloaded from Harvard University's DASH repository, and is made available under the terms and conditions applicable to Other Posted Material, as set forth at <http://nrs.harvard.edu/urn-3:HUL.InstRepos:dash.current.terms-of-use#LAA>

## Share Your Story

The Harvard community has made this article openly available.  
Please share how this access benefits you. [Submit a story](#).

[Accessibility](#)

Chemical Vapor Deposition of Cuprous  
Halide Semiconductors and Polymer  
Dielectrics for Applications in  
Optoelectronics and Flexible  
Microelectronics

A DISSERTATION PRESENTED

BY

CHRISTINA MARIE CHANG

TO

THE DEPARTMENT OF CHEMISTRY & CHEMICAL BIOLOGY

IN PARTIAL FULFILLMENT OF THE REQUIREMENTS

FOR THE DEGREE OF

DOCTOR OF PHILOSOPHY

IN THE SUBJECT OF

PHYSICAL CHEMISTRY

HARVARD UNIVERSITY

CAMBRIDGE, MASSACHUSETTS

DECEMBER 2019

© 2019 – CHRISTINA MARIE CHANG  
ALL RIGHTS RESERVED.

# Chemical Vapor Deposition of Cuprous Halide Semiconductors and Polymer Dielectrics for Applications in Optoelectronics and Flexible Microelectronics

## ABSTRACT

This dissertation presents the development of new chemical vapor deposition (CVD) processes, with an emphasis on imparting desired properties to thin film layers for next-generation devices. To this end, two research areas are described: CVD of metal halide semiconductors for optoelectronic devices, and CVD of dielectrics for 3-D microelectronic devices.

P-type semiconducting metal halide (MX) thin films are promising for use in optical coatings, imaging devices and optoelectronic devices like photovoltaics, but existing methods typically yield MX films of too poor quality (purity, continuity, and smoothness) to be used in these devices. CVD is one of the main techniques used in industry to fabricate device-quality films of other materials, because of its molecular-level control of the fabrication process. However, research efforts in the development of a CVD process to deposit continuous metal halide thin films have met several reactivity challenges. The few known metal halide CVD and ALD processes have been confined almost entirely to metal fluorides, and have typically required ancillary metal halides as the halide source. A more general route to metal halide vapor deposition, such as one using the hydrogen halides (HX) as the halide source, would be of considerable interest. Some researchers have succeeded in producing discontinuous “islands” of metal halides (e.g., CuCl, CuI) using HX as a precursor, but continuous thin films of metal chlorides, bromides, and iodides have remained elusive.

In response to this challenge, we have developed two vapor deposition methods that produce continuous CuX thin films. Chapter 2 of this dissertation discusses the vapor conversion of thin



films of copper sulfides and oxides to CuX by exposure to HX gas. Chapter 3 of this dissertation discusses CVD of CuBr thin films by reaction between HBr gas and vinyltrimethylsilane(hexafluoroacetylacetonato)copper(I). Our methods not only provide the desired device-quality films, but also expand the possibilities of metal halide CVD more generally. To the best of our knowledge, our method constitutes the first continuous, non-fluoride metal halide thin films deposited by CVD using the hydrogen halide as the vapor source. Our method provides a reaction pathway that may offer a more general route to CVD of metal halide thin films.

Finally, Chapter 4 of this dissertation describes work toward developing a CVD process to deposit a hybrid organic/inorganic dielectric material that is flexible, robust at elevated temperature, and highly tunable. This work is motivated by the emerging field of flexible electronics, which requires flexible dielectric materials. Polymers are widely used, but cannot withstand the extreme conditions required by some applications. Organic/inorganic hybrid dielectrics have the potential to provide both flexibility and stability to extreme conditions. However, the few existing hybrid dielectrics suffer from drawbacks such as limited tunability of the thickness or chemistry of the organic component. To begin to meet these challenges, a new hybrid dielectric is proposed, and several known vapor deposition processes for ceramics and polymers are implemented and assessed. Principally, we study the atomic layer deposition of alumina and aluminum silicate ceramic thin films, and the molecular layer deposition of parylene and polyimide thin films. These dielectric thin films are deposited on planar and wire substrates and characterized mechanically, thermally, compositionally, and electrically. Our results point toward promising next directions for research on hybrid dielectric thin films for flexible electronic devices.

# Contents

I	INTRODUCTION	I
I.1	Vapor Phase Thin Film Deposition Methods . . . . .	I
I.2	Techno-Economic Analysis Methodology . . . . .	3
I.2.1	Cost of Ownership for Individual Tools . . . . .	3
I.2.2	Cost of Device . . . . .	6
I.3	Scope of the Present Review . . . . .	7
I.4	Review of Vapor-Deposited Thin Film Techno-Economic Analyses . . . . .	9
I.4.1	Direct Manufacturing Costs Overview . . . . .	12
I.4.2	Material Costs . . . . .	15
I.4.3	Capital Equipment Costs . . . . .	16
I.4.4	Labor Costs . . . . .	22
I.4.5	Energy Costs . . . . .	23
I.4.6	Financial Inputs to the Models . . . . .	24
I.5	Presentation and Scope of Thesis . . . . .	25
	References . . . . .	30

2	VAPOR DEPOSITION OF COPPER(I) BROMIDE FILMS VIA A TWO-STEP CONVERSION PROCESS	31
2.1	Abstract . . . . .	32
2.2	Introduction . . . . .	32
2.3	Materials and Methods . . . . .	35
2.3.1	Film Growth . . . . .	35
2.3.2	Film Characterization . . . . .	36
2.4	Results and Discussion . . . . .	37
2.4.1	Ligand salt-contaminated film . . . . .	37
2.4.2	Growth and Characterization of Cuprous Sulfide Films . . . . .	37
2.4.3	Conversion to Cuprous Bromide . . . . .	41
2.5	Conclusion . . . . .	47
	References . . . . .	52
3	DIRECT CHEMICAL VAPOR DEPOSITION OF COPPER(I) BROMIDE THIN FILMS	53
3.1	Abstract . . . . .	54
3.2	Introduction . . . . .	54
3.3	Materials and Methods . . . . .	57
3.3.1	Diagram of the Reactor Setup . . . . .	57
3.3.2	Purification of Cu(hfac)(vtms) . . . . .	61
3.3.3	CVD Growth of CuBr and Cu . . . . .	64
3.3.4	Substrates . . . . .	66
3.3.5	Film Characterization . . . . .	67
3.4	Results and Discussion . . . . .	68
3.4.1	Screen of Substrates . . . . .	68

3.4.2	Film Composition Characterization . . . . .	69
3.4.3	Substrate Temperature Study . . . . .	76
3.4.4	Control Experiments . . . . .	77
3.4.5	Study of substrate oxidation over time . . . . .	84
3.4.6	Study of Growth Per Cycle . . . . .	84
3.4.7	Optical Characterization . . . . .	87
3.4.8	Electrical Characterization . . . . .	87
3.4.9	Contact Angle Analysis . . . . .	90
3.5	Conclusion . . . . .	96
	References . . . . .	100
4	TOWARD FLEXIBLE HYBRID POLYMER/CERAMIC DIELECTRIC THIN FILMS	101
4.1	Abstract . . . . .	101
4.2	Introduction . . . . .	102
4.2.1	Motivation for High-T Flexible Dielectric Coatings . . . . .	102
4.2.2	Requirements . . . . .	108
4.2.3	Existing Dielectric Coatings . . . . .	109
4.2.4	Specific Aims . . . . .	114
4.3	Rationale for Design of Hybrid Material . . . . .	115
4.3.1	Ceramic Processes Overview . . . . .	115
4.3.2	Polymers Overview . . . . .	118
4.3.3	Matching of Ceramic and Organic Process Parameters . . . . .	120
4.3.4	Selecting Organic Components . . . . .	123
4.4	Reactor Apparatus . . . . .	129
4.4.1	Reactor Design and Rationale . . . . .	129

4.4.2	Electronics and Software . . . . .	130
4.4.3	Manifold . . . . .	132
4.4.4	Chamber and Exhaust . . . . .	134
4.5	Materials and Methods . . . . .	134
4.5.1	Substrates . . . . .	134
4.5.2	Vapor Deposition of Aluminum Silicate Films . . . . .	135
4.5.3	Vapor Deposition of Parylene Films . . . . .	136
4.5.4	Vapor Deposition of Alumina Films . . . . .	137
4.5.5	Vapor Deposition of Polyimide Films . . . . .	138
4.5.6	Capacitor Devices . . . . .	138
4.5.7	Characterization Techniques . . . . .	139
4.6	Results and Discussion . . . . .	140
4.6.1	Commercial Wire Thermal Decomposition Characterization . . . . .	140
4.6.2	Organic Precursor Characterization . . . . .	141
4.6.3	Growth Characteristics of Aluminum Silicate Films . . . . .	144
4.6.4	Growth Characteristics of Alumina Films . . . . .	145
4.6.5	Growth of PMDA-TAEA Polyimide Films . . . . .	146
4.6.6	Growth of PMDA-ODA Polyimide Films . . . . .	148
4.6.7	Electrical Characterization of Dielectric Films . . . . .	150
4.6.8	Hybrid Films . . . . .	152
4.7	Conclusion and Future Work . . . . .	154
	References . . . . .	163

## Listing of figures

2.1	Contamination of film with acetamidinium bromide salt. . . . .	38
2.2	Cuprous sulfide film compositions beyond optimal temperature window. . . . .	39
2.3	Cuprous sulfide film growth optimization. . . . .	40
2.4	XPS depth profile of Cu <sub>2</sub> S film after HBr exposure at 60 °C. . . . .	42
2.5	XPS depth profile of Cu <sub>2</sub> S film after HBr exposure at 30 °C. . . . .	43
2.6	XRD of Cu <sub>2</sub> S film before and after HBr exposure. . . . .	44
2.7	SEM of Cu <sub>2</sub> S film after HBr exposure. . . . .	46
2.8	EDS of Cu <sub>2</sub> S film after HBr exposure. . . . .	47
3.1	Reactor diagram for CuBr depositions . . . . .	58
3.2	Piping & Instrumentation Diagram Legend. . . . .	59
3.3	Reactor tube furnace temperature reading calibration . . . . .	59
3.6	Purification of Cu(hfac)(vtms). . . . .	62
3.7	<sup>1</sup> H NMR spectrum of Cu(hfac)(vtms) after purification procedure. . . . .	63
3.8	<sup>1</sup> H NMR peaks of Cu(hfac)(vtms) after purification procedure. . . . .	63
3.9	SEM images of CuBr grown at 83.4 °C, high zoom . . . . .	70

3.10	SEM images of CuBr grown at 83.4 °C, medium zoom . . . . .	71
3.11	SEM images of CuBr grown at 83.4 °C, far zoom . . . . .	72
3.12	SEM images of CuBr deposited on Pt at a range of temperatures . . . . .	73
3.13	XPS depth profile of CuBr deposited on silicon nitride at 83.4 °C . . . . .	74
3.14	Fits of the Rutherford Backscattering Spectrometry data . . . . .	75
3.15	X-ray diffraction pattern of CuBr deposited on silicon nitride . . . . .	76
3.16	SEM images of CuBr grown on SiN <sub>x</sub> at a range of substrate temperatures . . . . .	78
3.17	SEM images of CuBr grown on SiN <sub>x</sub> at a range of substrate temperatures, wide zoom	79
3.18	SEM images of non-conductive substrates after control Cu depositions . . . . .	81
3.19	XPS depth profiles of non-conductive substrates after control Cu depositions . . . .	82
3.20	SEM images and XPS depth profile of Pt substrate after control Cu depositions . . .	83
3.21	SEM Micrograph of CuBr Deposited on SiN <sub>x</sub> at 1 foot from reactor inlet. . . . .	86
3.22	UV-Vis Spectrum of quartz . . . . .	88
3.23	UV-Vis Spectrum of 40 nm SiN <sub>x</sub> on quartz. . . . .	88
3.24	UV-Vis Spectrum of 120 nm CuBr on 40 nm SiN <sub>x</sub> on quartz. . . . .	89
3.25	Absorption coefficient versus energy for 120 nm CuBr on 40 nm SiN <sub>x</sub> on quartz. . .	89
3.26	Photograph of quartz, silicon nitride on quartz, and CuBr on silicon nitride on quartz	90
3.27	SEM Micrograph of CuBr sample used for Hall effect measurement. . . . .	90
3.28	Contact angle diagram . . . . .	91
3.29	Calculated polar and dispersive free energy components for several surfaces. . . . .	94
3.30	Calculated interfacial free energy components for CuBr films and substrates. . . . .	95
4.1	Stacked die system-in-package examples. . . . .	103
4.2	Draper Miniature Multiwire Systems Technology. . . . .	104
4.3	Draper Miniature Multiwire Systems Technology close-up. . . . .	105

4.4	Diagram of cross-sectional profiles of power and signal coax . . . . .	106
4.5	Coaxial cable before, during, and after the electric flame-off process. . . . .	107
4.6	Temperature-Young's Modulus tradespace for common dielectric materials. . . . .	110
4.7	ALD cycle to produce $Al_2O_3$ thin films . . . . .	118
4.8	MLD cycle of PMDA and EDA to produce polyimide thin films. . . . .	119
4.9	Proposed reaction scheme to produce hybrid material. . . . .	125
4.10	Polyimide-alumina tradespace and target material space . . . . .	128
4.11	Hybrid reactor diagram . . . . .	131
4.12	Pumping speed of a rotary pump as a function of pressure . . . . .	133
4.13	Several custom flat and wire substrate holders . . . . .	135
4.14	Wires on custom holder . . . . .	136
4.15	Metal-insulator-metal device configuration . . . . .	139
4.16	TGA data for PMDA and ODA . . . . .	142
4.17	TGA data for TAEA and ODA . . . . .	143
4.18	TGA data for 4AP . . . . .	143
4.19	Growth rate of aluminum silicate films . . . . .	144
4.20	SEM images depicting mechanical cracking of aluminum silicate films on Cu wires	145
4.21	Growth rate of alumina films . . . . .	146
4.22	Composition of alumina films . . . . .	147
4.23	Growth characteristics of PMDA-TAEA films . . . . .	148
4.24	FTIR spectra of PMDA-TAEA films . . . . .	149
4.25	Leakage current density through dielectric films as a function of applied bias. . . . .	152
4.26	Leakage current density through dielectric films as a function of applied field. . . . .	153
4.27	Rough estimate of predicted parameters for hybrid material. . . . .	155



# List of Tables

1.1	Total device cost model for five techno-economic analyses. . . . .	10
1.2	Direct manufacturing costs for thin-film devices . . . . .	12
1.3	Cost breakdown estimate for commercial CdTe modules . . . . .	14
1.4	Cost breakdown estimate for research-scale 3-J III-V Cells . . . . .	15
1.5	Materials price input parameters to vapor deposition techno-economic models. . .	17
1.6	Layer thicknesses for TE models . . . . .	18
1.7	Material utilization rates discussed in TE models. . . . .	19
1.8	Mole recovery fraction of materials not in film. . . . .	20
1.9	Deposition rates of thin film layers. . . . .	20
1.10	Device yield for various production processes. . . . .	20
1.11	Parameters to estimate tool uptime . . . . .	21
1.12	Capex of individual vapor deposition tools. . . . .	21
1.13	Total capex for solar techno-economic models. . . . .	22
1.14	Parameters to estimate labor and tool uptime . . . . .	22
1.15	Estimates of labor amount per solar production capacity. . . . .	23

1.16	Chemical vapor deposition equipment power usage . . . . .	23
1.17	Financial parameters for TEA analysis. . . . .	24
2.1	Parameters for Cu <sub>2</sub> S film conversions to CuBr. . . . .	48
4.1	Vapor methods for nanolaminates with non-polymer organic components. . . . .	112
4.2	Vapor methods for nanolaminates with polymers organic components. . . . .	113
4.3	Possible project options . . . . .	114
4.4	CVD processes to deposit AlN. . . . .	117
4.5	MLD processes to deposit polyimides . . . . .	120
4.6	MLD processes to deposit polymers. . . . .	121
4.7	Ceramic and polymer vapor deposition process temperature windows. . . . .	122
4.8	List of candidate linker molecules. . . . .	126
4.9	Proposed precursors for this project. . . . .	127
4.10	Decomposition onset temperature of 6 commercially available polymer wires. . . . .	141
4.11	Attempted depositions of PMDA-ODA polyimide. . . . .	151

TO MOM, DAD AND MATTHEW.

“She had studied the universe all her life, but had overlooked its clearest message: For small creatures such as we the vastness is bearable only through love.”

– Carl Sagan, *Contact*

“I tested the brackets by hitting them with rocks. This kind of sophistication is what we interplanetary scientists are known for.”

– Andy Weir, *The Martian*

# Acknowledgments

MY THESIS COMMITTEE members deserve the first thanks: Professor Roy G. Gordon, Professor Luke M. Davis, Dr. Caprice Gray-Haley, and Professor Michael J. Aziz.

As my thesis advisor, Roy graciously gave me the freedom to direct and develop my own interests, from my solar panel research and my independent proposal of my Draper-funded research project, to my professional interests like teaching and machine shop training. Roy always affirmed my work's value, agreeing whenever I pitched an opportunity, including applying to grants and filing a patent on our work together. Roy taught me how to use fundamental physical chemistry to construct powerfully simple scientific arguments. Beyond my technical work, Roy helped me develop my own leadership style within our lab.

I am incredibly grateful and proud to have been Luke Davis's first student. Luke figured out the delicate magic of helping a student become an original thinker. He supported me to follow my dreams without judgment. Luke has been my principal partner in scientific brainstorming and whiteboarding: he never hesitates to excitedly dig into questions together. Via this engagement, Luke helped shaped our joint projects, suggesting innovative and productive directions. I deeply

appreciated his initiative and immense ability to concretely move projects forward quickly. Luke taught me how to design experiments where something is learned no matter the outcome. Much of my development as an independent scientist and mentor I attribute to Luke.

Dr. Caprice Gray-Haley, my co-advisor for the past 2+ years through the Draper Laboratory Fellowship is a role model of a scientist-leader-mother who vulnerably acknowledges areas for growth, a quality that makes her that much more courageous. I learned from her how to lead a group by empowering individuals to own their work. She always believed that my work was far better than I ever thought it was, showing me that my own worth was greater than I realized.

Through his energy technology class and leadership of the HUCE Energy & Environment Consortium, Professor Mike Aziz devoted a huge amount of effort to developing Harvard students as energy technology thought leaders. I will never forget one particular interaction with Mike that spoke volumes to me. Soon after I delivered a presentation at the Harvard Energy Journal Club (HEJC) which I deemed to be subpar, I happened to have a meeting with him. I immediately apologized for my performance, and he responded that an HEJC presentation being “rough around the edges” is ideal – if it had been perfect, that would have meant I’d spent too much time on it. Mike gave me permission not to be perfect, and this comment proceeded to shape a new, more fearless and free approach to my innovative pursuits.

In addition to my four defense committee members, the faculty at Harvard and MIT who have served on my Graduate Advising Committee over the years have been attentive, thoughtful, and engaged: Professor Cynthia Friend, Professor Rafael Jaramillo, Professor Vinothan Manoharan.

I am grateful to several Harvard faculty mentors. I greatly respect and admire Professor Jenny Hoffman. Jenny’s career and professional advice is helpful because she thinks creatively. She taught me to stick up for myself with diplomacy, and ferociously supported me as a female scientist. I aspire to be like Jenny: her priorities are reflected in how she spends her time. She realizes that paying it forward as a mentor and role model is as important as scientific research objectives.

Professor Dan Schrag has been an incredibly supportive mentor. Early in my PhD, he advocated for me, introducing me to his network, and this connection was the main catalyst in my becoming a member and contributor within the U.S. cleantech ecosystem. Through sponsoring my various leadership activities – e.g. HEJC, energy technology social events, and the Nudging Toward a Cleaner Future Conference – Dan supported me unconditionally in my pursuit of sustaining the student and postdoc energy technology community here at Harvard. Worth far more than any budgetary dollar amount was the knowledge that he believed in supporting our learning, growth, and teamwork toward these important societal challenges. I also learned technical skills from him via the HUCE Consortium and his climate class: principally, how to separate signal from noise. Dan is a role model in his balance of technical depth and technical breadth along with policy, teaching, and being a supportive and kind presence in the community he helped create at HUCE. I aspire to this balance one day, having seen through Dan that it is possible.

I believe strongly in the course that Professor Jim Anderson designed, PSII. Jim has been a supportive mentor, recognizing, valuing and stating my worth not only as a Teaching Fellow but also as a scientist and a leader. Plus, I loved the day he let us test drive his electric car around the economics department parking lot.

I am grateful to my other faculty members in the Chemistry & Chemical Biology department, including Professor Ted Betley and Professor Dan Nocera, who both have been active Directors of Graduate Study and provided mentorship not only to me personally, but also to the wider CCB graduate student body, via “Prof Talks” that we co-organized.

I have been privileged to work with the Gordon Lab members. I am especially indebted to Dr. Rachel Heasley. My main experimental research mentor in the lab, Rachel taught me the essential hard skills of CVD work, from regulator fittings to changing pump oil to resetting the circuit breakers. Rachel was happy to pull late nights and early mornings and sometimes do more than 50% of the work: we developed a true partnership in the laboratory that was flexible, productive,

and greater than the sum of its parts. Beyond delivering results, Rachel made it all fun. On weekend mornings in the basement of CNS, I would pretend the SEM antechamber interlock was the airlock in a crucial outer space mission, and she would amusedly oblige my sci-fi. Between days in the XRD facility and hours on the floor tending to Pumpy the pump, we would celebrate our cuprous halide thin films with dances like no one was watching. And outside the lab, I couldn't ask for a more supportive friend.

My first long-term lab mentee, Eliza Spear helped me learn so much about effective mentoring, collaboration, and teamwork. She aggressively pushed both of our joint projects forward due to not only her incredible work ethic but also her creativity and alacrity to try new hard things, not giving up until they were completed. I loved collaborating with her for my final year in the Gordon lab. She enriched our projects by providing motivation, excitement, good questions, and excellent interpersonal skills. Eliza is also an outstanding office mate and friend. I aspire to her level of emotional support, validation, vulnerability, and compassion.

My labmate Dr. Lauren Hartle is always willing to help with everything, from teaching me way too much about fittings and cylinders, to being the only other person *ever* excited about Lab Cleanup Day. As an office mate and friend, Lauren made my experience in the Gordon Lab much more enjoyable and manageable. Her support and encouragement consisted of science and fun in equal measures, from a daylong pillow fort to serenading Teri with impromptu harmonized greeting songs, not once or twice, but nearly every time she walked into the office. I appreciated Lauren's support as a friend: we discussed difficult life decisions openly, and I've met few others happier to accompany me on my deep dives into productivity and organizational systems.

As the den mother of our lab, Teri Howard was supportive and protective of the Gordon lab both as researchers and as individuals. Though I was a student, she treated me with so much respect, taking my research and professional development seriously and thereby helping me to recognize my own value as a scientist. Teri was also a trusted partner in organizing the lab. She was incredibly de-



pendable, responsible, and principled; I always knew our joint initiatives were in extremely capable hands. Pattee McGarry joined the Gordon lab for my final year here, and she has been incredibly accommodating and kind, supporting me in whatever I wanted, be it research expenses or arranging my thesis defense logistics. Our emotional solidarity has been helpful and touching.

Robert Gustafson has been a close collaborator and fearless fellow solar CVD researcher, helping me with cylinder work, regulator testing, reactor troubleshooting, and numerous professional and personal machine shop projects. Beyond hands-on work, Bobby has been one of my closest thought partners. He is happy to regularly think critically with me about my project and make nuanced and well-informed suggestions for my work, both regarding experimental details and the big-picture level. Bobby and I have traded best practices and supported each other through professional decisions as we move into our independent scientific careers simultaneously. Beyond the lab, I've appreciated Bobby's warm and loyal friendship, including his advice and commiseration.

I have valued my close friendship with Dan Pollack. As a Gordon laboratory colleague, Dan has provided excellent suggestions, detailed critiques, enthusiastic engagement, thoughtful questions, curious inquiry, and an inspirational desire to drill down to the truth of complicated phenomena. As the Vice President of HEJC during my Presidency, Dan was incredibly organized, meticulous, professional, and simply a joy to work with. Beyond research and our scientific interests, Dan has been generous, helpful and delightful as a friend, from co-hosting French language soirees together to cheering each other through the many milestones of the PhD.

The only Gordon colleague in my same cohort year, Xian Gong has been a friendly collaborator. I have appreciated working with Xian, whose nose-to-the-grindstone work ethic was motivational to me, and which contributed to some of the experiments in this thesis.

Kathy Liu was my first formal mentee, and I enjoyed every single day we worked together during her summer as a Research Science Institute (RSI) intern. She was excited about our work, eager to learn, highly organized and coachable, and put in long hours with enthusiasm. Working with Kathy

was especially gratifying because we shared a research legacy as Rickoids of the Year, RSI interns, and RSI counselors, and I remain grateful for our special bond.

Thanushi Peiris was a delightful and easygoing mentee to work with, and I am so grateful that we were able to spend her RSI internship together, bonding over solar research, a shared love of chemistry, and cultural differences that made us laugh and brought us closer together.

Dr. Aykut Aydin led many aspects of the Gordon side of the A2P Draper collaboration, providing early thought leadership that contributed to my work on the MMS Draper collaboration. Dr. Lu Sun and I conducted some work together on dielectrics, and I appreciated her collaboration and cleanroom training. I am grateful as well to Emily Kerr, whose Schlenk line and NMR expertise facilitated the purification of a CVD precursor described in this thesis.

I gratefully acknowledge the rest of the Gordon Group for helpful discussion and advice both scientifically and professionally: Dr. Eugene Beh, Dr. Danny Ming Wei Chua, Dr. Jun Feng, Dr. Ashwin Jayaraman, Dr. Sang Bok Kim, Dr. Kecheng Li, Dr. Kaixiang Lin, Dr. Harbing Lou, Dr. Liuchuan Tong, Dr. Chuanxi Yang, Dr. Xizhu Zhou, Dr. Yunlong Ji, Dr. Yan Jing, Dr. Diana De-Porcellinis, Dr. Jaeyeong Heo, Dr. Marc-Antoni Goulet, Dr. Sunghwan Lee, Dr. Dawen Pang, Martin Shijian Jin, Min Wu, Mike Vogel, Alvaro Valle, Berenger Wegman, and Zhongqiang Hu.

Researchers at Draper Laboratory contributed to the results in this thesis through helpful conversations, expert advice, sample preparation, explanations of the device performance aspects of our collaborative work, and hands-on assistance with experiments. I gratefully acknowledge Henry Raczkowski, Dr. Morgan Pilkenton, Dr. Sara Barron, and Dr. Tara Sarathi, Dr. Jeff Delisio, and especially my advocate and mentor Dr. Amy Duwel. I am also grateful for the generous financial support of the Draper Fellowship and the internal research and development (IRAD) project at Draper Miniature-Multi-Wire Systems (MMS) which has served as the basis for one chapter of this dissertation.

Recalling the hours I spent in the Physics Machine Shop with Stan Cotreau will never cease to

bring a smile to my face. Beyond his simply excellent and intuitive training style that gave me the joy of building my own reactor parts, Stan was a solidly wonderful friend. Couched in his characteristic playful sarcasm, discussions with Stan were at once profound and instructive. I've never met anyone else whose snarky humor so obviously told you that he cared more than anything about your happiness, safety, and development as a student and as a person. I loved the atmosphere Stan created in the Machine Shop, which transformed it into a community.

Several staff members at the Center for Nanoscale Systems were instrumental to the results in this thesis. I am indebted to Mac Hathaway for both his helpful conversations about chemical vapor deposition and his encouragement of and belief in me as a researcher, scholar, and inventor. Dr. Philippe deRouffignac has been gracious throughout my time at Harvard, supporting my science through work together on his bespoke SiO<sub>2</sub> ALD tool and supporting my career via advice from his experience in the semiconductor industry. Greg Lin aided greatly in the XPS experiments described in this thesis and patiently troubleshooted both data and instrumentation. Dr. Arthur McClelland generously lent his time, expertise, and dry sense of humor in helping me troubleshoot UV-Vis optical measurements. Jason Tresback was a useful source of theory and hands-on knowledge regarding several characterization techniques used in this chapter.

Beyond the individuals at Harvard who directly impacted the scientific results in this thesis, the first thanks belong to my family: Mom, Dad, and Matthew. My father, Dr. Fred Chang, decreed when I was 6 years old that I'd be getting a PhD in science, and from that day I never once doubted this future would come to pass. He facilitated my brother's and my path into science from early in our childhoods, instituting family traditions like Chang Convention, in which each Christmas we practiced concise public speaking, curious inquiry, problem solving, critical dialogue and independent research. At every career juncture, he supported me to follow a scientific path, always believing in my ability to rise to any challenge. To quote Guy Patterson, "You are my biggest fan."

I can't imagine having reached this point in my life without the support of my mother, Carol

Chang. She was instrumental in turning my every dream into reality, supporting every initiative, project and activity I got excited about. She dedicated an absurd amount of time to helping me grow and flourish as a student, volunteer, and citizen. She taught me to believe in myself and showed me how to follow my passions. I remain inspired by her energy and compassion every single day.

Nothing I could write would do justice to my gratitude for my brother and best friend, Matthew Chang. He saw me through our rigorous upbringing with patience, humor, and the camaraderie that comes with sharing your entire life with someone you love. Moreover, he eagerly and surprisingly productively helped me as a thought partner on several research projects, with his dry wit and analytical, out-of-the-box thinking style. We often joke that he deserves a small piece of each degree I've earned and a minor author position on each paper I've published.

I have been grateful to my family-away-from-home during my PhD. Dr. Tom Schuhmann enriched my time here at Harvard, providing emotional support, technical advice, constructive feedback, the commiseration of our shared Harvard PhD experience, and treasured memories we made together outside the lab. The entire Glidden-Page family welcomed and adopted me during my PhD, and I will be forever touched by their warm support, love, and the example they set for the kind of person I want to become. Lindy Li has been a steadfast cheerleader, supporter, confidante and adopted sister: we thrive on each other's enthusiasm and passion for our fields, each celebrating the other's inspirational work. Dr. Teresa Williams has been an older sister to me, combining technical and professional expertise as my longtime scientific mentor with interpersonal and emotional depth as a confidante. My PhD process was made much richer by Teresa's pertinent advice, unwavering support, connected, empathetic mentorship style, her role modeling of following her own doctoral dream. Dr. Kathryn Santner has been an exceedingly supportive and selfless friend. Kathryn's kindness and our continued camaraderie since our graduate study at Cambridge University have been foundational to my development as a person. I am so lucky that we found each other! Haiyan Xu has helped me during my PhD more than I can adequately express. From her courage

and adventuresome spirit that propel her up 18-pitch climbs and through new trad climbing grades, to her active, conscientious attitude toward societal injustices from consumerism to sexism, Haiyan continually inspires me. Besides being one of the most thoughtful and attentive friends I have ever met, Haiyan has also brought so much color and depth to my life in Cambridge, from jamming in our music duo (the Cordlettes!) to being a supportive and steadfast climbing partner as we both progressed quickly and enthusiastically together as climbers.

Dr. Zamyła Chan was my first and closest new friend in our CCB cohort. Scientifically, we have relied on each other as a technical and professional sounding board, both in classes and in research. Beyond science, I have never met someone so dedicated and talented in so many important pursuits. I am continually learning from her balance, boundary-setting skills, and commitment to excellence. I have truly treasured our relationship, in which we have bonded through seeing each other through the highs and lows of our PhDs. From late nights supporting each other through science, to living out our dream of a trip to Harry Potter world, Zamyła has seen me through every challenge that has come my way and has celebrated me through every victory no matter how small.

Dan Strassfeld and I have a unique friendship that only comes through following a path together for over a decade – from Princeton’s chemistry department as undergrads, to the University of Cambridge for our Master’s, to pursuing our PhDs in chemistry here at Harvard, including sharing the same lifelong mentor, Professor Jeffrey Schwartz. I know nobody else with Dan’s winning combination of dark humor, sarcastic self-effacing commentary, profound philosophical introspection, and wicked quick intelligence that he’ll never earnestly acknowledge and I’ll always admire. Dan has a heart of gold and is one of the most generous people I know, putting others before himself without a second thought. I have been so fortunate to have him in my life.

I have been thrilled to have Zinan Zhang as a friend in my life as our paths have continued to bring us together, from Princeton’s chemistry department, to the University of Cambridge, and here at Harvard. Our free-ranging conversations about everything under the sun have enhanced my

perspective. He has been a close confidant, excellent travel partner, and constant in my life, and I have appreciated the breadth, nuance, and sense of adventure he has brought to our time together.

Cathy Zhang has been a steadfast friend since our first semester in grad school together, bringing her characteristic upbeat and creative nature to our every interaction. She and Stephen Giandomenico have added cheer and lightness to my PhD experience, from Friendsgiving food comas to saving the world many times via the Pandemic Legacy board game. Their companionship transcended my identity as a PhD student, rounding out my experience by reminding me of everything else important in life.

With Emma Rosenfeld, I had the singular experience of meeting someone and instantly knowing we were on the same wavelength. It has brought me great happiness to share so much with her: from unabashed enthusiasm for science and unapologetic celebration of each other's innovative capacity, to our shared curiosity and drive to explore problems that matter beyond our subfield. I have truly appreciated Emma's vulnerability, raw sense of humor, dynamic intellect, and compassionate support.

Few organizations have made me more proud than the Graduate and Postdoctoral Council (GPC) in Harvard's CCB Department. The officers and volunteers I worked with during my two years as GPC President poured their hearts into serving our community not for any professional credit, but because they felt it was the right thing to do. I especially thank Dr. Jeff Bessen, Dr. Joey Goodknight, Molly Huff, Dr. John Janetzko, Ethan Magno, Liz Johnson, Hope Flaxman, Dr. Eileen Moison, Andrew Bendelsmith, Victor Zhao, Matt Volpe, and Nathaniel Braffman.

Many members of the Harvard CCB community have been integral to my experience here. I am thankful for Elizabeth Lennox, Kathy Oakley, Barbara Anderson, Helen Schwickrath, Joe Lavin, and Susan Kinsella, whose effective work in administering our department resolved many of my headaches and never failed to put a smile on my face. I am grateful to Dr. Gregg Tucci and Dr. Lu Wang, who made my teaching experience in PSII one of the most enjoyable and rewarding experi-

ences of my graduate career.

Beyond the CCB department, I am grateful to the HUCE community, my second home at Harvard. Eric Simms, Jill Murphy, and Dr. Jim Clem at HUCE were incredibly supportive, responsive, and helpful. Five years of Harvard Energy Journal Club were formative for me. I was floored by the talent and insight of the members of HEJC, a group where I felt I had found “my people.” I was lucky to lead HEJC as President for five semesters, with two amazing Vice Presidents: Dan Pollack and subsequently Amos Meeks. I learned so much about leadership and analysis of critical energy issues from the former HEJC Presidents during my time at Harvard: Dr. Lauren Hartle, Dr. Jason Munster, Dr. Daniel Thorpe, Bobby Gustafson, and Andy Greenspon. I acknowledge several HEJC members who significantly contributed to my development into a more nuanced energy technology thinker: Carlo Amadei, Colleen Golja, John Harrold, Drew Wong, Eric Fell, Baptiste Lemaire, Ben Franta, Anna Shneidman, Andrew Bergman, Felix Barber, Lauren Kuntz, Jane Philbrick, Bob Kleinberg, Mandy Liu, Justin Teesdale, Toly Rinberg, Bridger Ruyle, Christian Holkeboer, Karen Yu, Doris Hoffmeyer, Jordan Wilkerson, Ed Birkett, Toby Egle, Kat Geddes, Kanchi Gandhi, Alex Clark, Tyler St. Germaine, Tim Menke, Yanina Barrera, Franklin Wolfe, Nico Sawaya, Henry Wilkin, and Jack Hensley. I am grateful to everyone I interacted with in the Energy & Environment Consortium, including Jonathan Moch, Yanpeng Sun, Shahir Masri, and my Nudging Toward a Cleaner Future Conference co-founders Cindy Hu and Shauna Theel. I found kindred spirits in Cindy and Shauna, who worked with me and with our incredible mentor, supporter, and co-sponsor Professor Max Bazerman, to organize a meaningful initiative. I am also grateful to have had many positive interactions within the welcoming broader energy community in Cambridge through Greentown Labs, and especially to have met Chloe Holzinger, whose passion, incisive intellect, go-getter attitude and thoughtfulness about her values have been inspirational and delightful as we have moved through our journeys in energy technology together.

My PhD experience would not have been complete without the delightful community of foreign-

language aficionados. First, I am profoundly grateful to my co-organizers of the Dudley House / GSAS Student Center language tables: Taylor Valley and Ilia Gelfat for Spanish; Emily Gehrels, Will Tilleczek, and Arthur Tsang for French. Several other language partners provided leadership and camaraderie at our gatherings: Dan Pollack, Marissa Kimsey, Cécile Guédon, Christophe Dupré, Marielle Remillard, and Max Ehrenfreund. These individuals each have more passion, patience, talents and interests than can fit in a single lifetime: I have been blown away by their immense capability for learning. They have all supported me in my love of languages and linguistics, my personal and professional quandaries, and helped me live out my dreams of creating a linguaphile community at Harvard where we laugh aloud constantly.

I gratefully acknowledge several other PhD friends with whom I have delighted to share time at Harvard. Aroop Mukharji is a talented author and musician and a thoughtful scholar, whose friendship which began in our time as Marshall Scholars solidified during our PhDs at Harvard. Dr. Pallav Kosuri supported me through the ups and downs of both my PhD and my climbing pursuits with warm positivity and natural, attentive compassion. Melinda Malley became a primary confidante during my PhD, and I am grateful for our close rapport in our personal journeys, her ability to calm me down and help me analyze situations when I am stuck or confused, and our compatibility as climbing adventure partners. Several other friends within the Harvard science community have brought balance, perspective, and camaraderie to my time here: Tessa Green, Jenny Bergner, Alexa Jackson, Emma Bertran, Tamara Pico, Carina Chittim, and Micheline Soley. I am also fortunate to have a close childhood friend, Alex Valiton, live so close to Boston during my PhD: it has been a pleasure to conduct our PhD work in parallel and to celebrate Alex's tenacity and her vivacious pursuit of science and of life.

Beyond Harvard, I consider myself incredibly lucky to have found the MIT Outing Club (MITOC). MITOC is a gem, unique in its camaraderie, inclusion, wealth of expert knowledge, emphasis on teaching and safety, and ability to empower individuals to do anything they dream, be it com-



pleting a big wall climbing objective or organizing a women's climbing retreat. Ben Kessel was my first outdoor climbing mentor, which is a unique relationship for any climber. Has always encouraged me to try hard climbs I would never have attempted otherwise. He took me on my first multi-pitch sport climb (Rock Du Jours, 5.9+) and, just half a year later, he led a trip where I swung leads on my first multi-pitch trad route (Endeavour, 5.7). I would never have thought myself capable of such progress and I simply cannot thank Ben enough for the camaraderie and deep friendship he has brought to my time in Cambridge and the way he has transformed my outlook on what I envision for myself. Alex Garcia and Dr. Chris Saulnier also believed in me before I ever believed in myself. Though I had only been climbing outdoors a few months and I hardly knew them, they expressly took me aside for a full day to teach me trad climbing, an activity I had always thought was too extreme for me. Not only did they make this climbing style approachable, fun, and safe, but also they empowered me to love trad climbing for myself. Beyond personally mentoring me, Alex has been a role model for me as a leader, as I have admired his inclusive, modest, and humble attitude. Chris and William "Blox" Bloxham also created space for life-altering growth for me: they led an intermediate ice climbing trip and encouraged me to show up – for the trip and for myself – though I was sure I wouldn't be skilled enough and I was insecure, hesitant to dive into winter sports in which (as a Texan!) I didn't feel I "fit in." I am especially grateful to Chris, who patiently belayed me as I dry-tooled my way up my first mixed rock/ice climbs, where I gratuitously yelled with every ice axe swing. Dr. Julian Kwan practically hauled me up multipitch crack climbs at Cathedral that were beyond my ability. He patiently honed my trad skills beyond the basics, to the point where I could lead my own trad trips, training for which I am incredibly grateful. Spending time with Julian, I never felt rushed or judged. After all, anyone who sees you pull out a Nalgene full of lasagna halfway up the wall and says, "good idea" is clearly a good person. As Climbing Chair, David Johnson emotionally and financially supported my every idea to make MITOC more inclusive, especially for women. These leaders have all thought exceptionally deeply about how to help women to love

climbing, a historically a male-dominated activity. They elevate my voice, take my safety suggestions seriously, invite me to lead others, encourage vulnerability, celebrate my strength, and appreciate the way I approach a climb, even when it's different from how they'd approach it. They have prompted me to rethink my relationship to the outdoors and my ability to do hard things. For all of this, I am more grateful to them than words can say.

In addition to my mentors, I have learned and benefited so much from my close MITOC climbing partners and friends. Haiyan Xu has been climbing outdoors with me almost from Day One, and I am so appreciative of her vulnerability and *joie de vivre*. Aileen Devlin has become a close climbing partner and friend, and I am continually inspired by her positive outlook, healthy life balance, insane productivity, and fearlessness in many aspects of life (including being happy to take lead falls!). I am floored by Alyssa Rudelis's character: her courage to speak her mind and especially to stand up for others and for her values inspires me continually. Dr. Alex Batchelor formally mentored Alyssa and me in our journey to advance as winter hikers and Winter School leaders; co-leading our "Feminists on Field" hike was a moving and empowering experience for me, helping me redefine and reclaim the outdoors in a deeply personal way. Evan Williams has inspired me with her leadership in MITOC and her personal progress as a climber. Evan has reminded me to reject the mold; rather, the only person who needs to give you permission to do anything is yourself. I have had so much fun spending time with David Chang, who is probably the best active listener I have ever met, and whose bold attitude toward many aspects of life has helped me see my own blind spots and form the image of the person I want to become. I am also grateful for the mentorship and friendship of Bekah Larsen: beyond her insane climbing ability and impressive work ethic, Bekah is such a kind soul and it has been so supportive to have her as a friend during our PhDs. I am so glad that Suzy McKinney found our MITOC family: her self-assurance and maturity made her an instant role model, and she has seen me through hard times with keen insight and perspective. Vince Casbarro has been a fantastic new climbing partner and friend, and I have learned so much from

his enviable knack for leading a wide life like nobody's watching. I am grateful to my Rock Season 2018 mentees, Jill Murphy and Chen Lu: we laughed, cried, stretched, dyno'ed, and trained so many pull-ups at Brooklyn Boulders, culminating in a co-organized Women's Climbing Retreat in May of 2019 with about 40 attendees, which represented a capstone for me in forming the "Belaydies" community. Overall, it is impossible for me to do justice in writing to these people who have profoundly changed my life.

My Harvard housemates have made my PhD experience easier and more enjoyable: I gratefully acknowledge Veronica Cardenas, Saha Saeed, Rajji Desai, Alethea Cook and Mary Bailey Kennedy. I am grateful to the Dancin' Fools community, whose weekly west coast swing dance nights expanded my experience here in Cambridge, especially Neal Klein, Jeff Wang, and Omer Gottesman.

Finally, I gratefully acknowledge several funding sources that contributed to work presented in this dissertation: the EPA-Marshall Scholarship, the A2P and MMS programs at Draper Laboratory, and the Draper Laboratory Fellowship.

# 1

## Introduction

### 1.1 VAPOR PHASE THIN FILM DEPOSITION METHODS

Thin film layers of materials (insulators, semiconductors, and metals) are used across industry, from optical devices and electrical coatings to virtually all electronic devices (e.g. energy storage, telecommunications). Many of these thin film layers are made by vacuum-based methods in which the active components of the thin film materials are transported to the substrate in the vapor phase.

Vapor-phase methods have some advantages over other, non-vacuum based approaches (e.g. solution-based coatings, electrodeposition). Vapor phase methods can often produce highly reproducible device-quality films of high purity because impurities do not enter the gas phase. Vapor phase methods can also produce films that are also highly uniform, because of the precision with which the deposition rate can be monitored and controlled.

Vapor phase methods can be broadly categorized into two different categories: physical vapor deposition (PVD) and chemical vapor deposition (CVD). In PVD methods, a “target” material is accelerated toward a substrate under vacuum, and directly becomes a thin film on the substrate. PVD methods include thermal evaporation, electron beam (E-beam) evaporation, pulsed-laser deposition (PLD), vapor transport deposition (VTD), close-space sublimation (CSS), and direct current (DC) or radio frequency (RF) magnetron sputtering.

Alternately, in CVD methods, “precursor” materials are thermally evaporated and released into a reactor chamber where they undergo a chemical reaction, producing the thin film of the desired material and gaseous byproducts that are purged or evacuated from the reactor. CVD variants include metalorganic CVD (MOCVD), atomic layer deposition (ALD), pulsed CVD (p-CVD), direct liquid injection (DLI-CVD), plasma-enhanced CVD (PECVD). CVD methods can be classified by operating conditions: atmospheric, low-pressure, or ultrahigh vacuum. CVD methods can also be classified by type of substrate heating: in hot wall CVD, the chamber is heated by an external power source and the substrate is heated, often by radiation (for example, from a heating coil) and optionally via heated substrate holder; in cold wall CVD, the chamber walls are at room temperature, and the substrate is directly heated either by induction or by passing current through the substrate or its holder.

## 1.2 TECHNO-ECONOMIC ANALYSIS METHODOLOGY

Vapor deposition processes have been optimized and better understood through not only experimentation but also physics- and chemistry-based modeling. This technical modeling and simulations are important because they enable us to predict and verify the science underpinning these processes. These studies include models of diffusion, radiative exchange, reactor flow, and deposition. They allow us to optimize reactor equipment design for a specific outcome like deposition rate, composition, or morphology. Many parameters can be tuned in this optimization: the geometry and materials used for thermal insulation, the gas injection design, the temperature in the reactor and its gradient, the substrate position, the gas flow rates, trap volumes, and the reaction initiation conditions (e.g. plasma discharge parameters). These simulations and technical models and their contributions to the literature and development of vapor deposition are reviewed elsewhere.<sup>1</sup> Early work in this area was championed by SEMATECH,<sup>2</sup> Sandia National Laboratory,<sup>3</sup> and others.

Beyond purely technical understanding and optimization, vapor deposition instruments exist in a commercial context. Thin film devices are made not only with device performance in mind, but also with the ultimate goal of delivering the device as a product to a customer. Cost is a key factor in determining the success of any new technology. In this context, when developing a vapor deposition technology with the ultimate goal of commercialization, economic factors must be considered. This Introduction provides a review of techno-economic modeling methodology in the context of vapor deposition methods.

### 1.2.1 COST OF OWNERSHIP FOR INDIVIDUAL TOOLS

Economic analysis of the factories and equipment to produce semiconductors dates back to a presentation given by G. Dan Hutcheson at the American Society for Engineering Education conference in 1981.<sup>4,5</sup> Hutcheson developed his factory-wide model in order to better understand whether

increasing capital investments were driving decreased profitability in the industry in the U.S. Moving beyond the classic financial analysis typically conducted at the time, Hutcheson incorporated in his model technical parameters, such as resolution and defect density, in order to calculate the cost per device that could be sold. Importantly, not all devices could be sold, because of reproducibility and quality control issues, so the inclusion of technological parameters contributed to the model's success. In particular, Hutcheson concluded that higher-cost factories were actually more profitable because they produced a higher yield of sellable devices, resulting in lower cost per sellable device. His model successfully predicted the continued rise of high-cost factories: capital costs of factories in the 1980s were approximately double that of the preceding generation.<sup>6</sup>

However, one downside of Hutcheson's model was its inclusion of hundreds of variables, and it thus was too complex to be practically useful for factory owners. Further work focused on simpler models at the equipment, instead of factory, level. These models are called Cost of Ownership (COO) models, and today these models are used to aid equipment selection and development choices in the industry. Perhaps the largest benchmark in the development and standardization of such models occurred in the mid-to-late 1980s, when the Japanese semiconductor industry had begun to surpass American semiconductor manufacturing.<sup>7</sup> In order to solve common manufacturing problems and regain competitiveness, the U.S. government partnered with 14 U.S.-based manufacturers in 1987 to form SEMATECH (loosely coined from "semiconductor manufacturing technology"), a not-for-profit consortium. SEMATECH championed techno-economic modeling. The SEMATECH COO model has become the de facto standard in the industry, creating a fair playing field of comparison between tools and techniques.<sup>8</sup> Versions of the The SEMATECH COO model were commercialized in 1993 (called COO and TWO COOL), and then SEMATECH jointly standardized with the global industry association SEMI, leading to the generation of the SEMI E35 standard, which was published in 1995. An Excel model, this SEMI 35 standard is voluntary, public, and widely used. It was available for roughly \$7k in 1995. Its history and features are reviewed

elsewhere.<sup>7</sup> It has up to 90 inputs and 210 output parameters. For illustrative purposes, the most common COO model in use in the semiconductor industry today is, at its simplest, exemplified by the following equation:<sup>9</sup>

$$COO = \frac{\text{Total cost of equipment over its lifetime (\$)}}{\text{Total number of good wafers produced}}$$

$$COO = \frac{F + L + R - S}{L \times T \times U \times Y}$$

where:

$F$  = fixed costs: initial purchase price and installation and training, the cost of moving equipment in the factory, etc.

$L$  = direct and indirect labor costs over the tool's serviceable lifetime

$R$  = recurring costs, including: costs of consumable materials, maintenance, and floor space over the tool's serviceable lifetime

$S$  = scrap value: the estimated number of unsellable parts multiplied by the value for which those parts can be re-sold as scrap, over the tool lifetime; this value thus represents money recovered

$L$  = serviceable lifetime of the tool

$T$  = theoretical maximum throughput of wafers per unit time, taking into account loading, processing, and unloading of wafers

$U$  = utilization, which is a fraction that modifies  $T$  with a practical estimate, taking into account downtime for maintenance, etc.

$Y$  = yield, representing the percentage of parts that pass quality control at the end of the process of this tool

Of course, many more factors are included in the extended SEMI 35 model; the reader is referred to the model for further detail. Although SEMATECH stopped support in April of 1995, it is avail-



able as TWO COOL from Wright Williams & Kelly, Inc. for a few hundred dollars per month per license.

### 1.2.2 COST OF DEVICE

Ultimately, the cost of a full device is the most useful quantity to model and predict. The device will contain one or more vapor-deposited thin films, each of which is deposited using an individual tool, whose COO can be modeled as discussed in Section 1.2.1. But cost modeling at the full stack level is more complex than just modeling the COO of the tools to make each layer of the device and adding the values together. In order to understand and predict the cost of a device, we may rely on techno-economic analysis (TEA), a methodology framework combining modeling, engineering design, and economic evaluation in order to analyze the performance of a product or process.

So-called “bottom-up” cost models represent the vast majority of all models to estimate the current costs of thin-film devices. Such models are common because their granularity makes them useful for process improvement. For example, using such models can highlight key cost drivers and enable a map to target device all-in cost, by helping to identify the research, development, manufacturing, and scaling challenges required to achieve this cost. Such analysis can inform R&D directions in industry, helping to answer questions about which new tools to purchase or develop. Bottom-up models can be used by researchers interested in testing price sensitivity of particular technology changes.

Among publicly available methodologies, arguably the state-of-the-art approach is that employed by the U.S. National Renewable Energy Laboratory (NREL). Though there are private cost model methodologies for thin film devices, the above methodology is the most thorough and sophisticated recent publicly-available one. The general methodology is here excerpted verbatim from Horowitz et al. regarding a solar cell technology the authors modeled:<sup>10</sup>

1. Determine a model device structure and manufacturing process flow based on academic literature, patents, and expert input, including interviews with current solar cell manufacturers.
2. Create total cost-of-ownership models for each step in the process flow, which include all materials, direct labor, electricity, equipment, manufacturing facility, and maintenance costs.
3. Collect input data for the cost-of-ownership models for each process step, including, for example, deposition rates and other elements of process or cycle time, consumables usage, material utilization rates, and pricing.
  - These data are collected from material and equipment suppliers, as well as solar cell manufacturers and other experts.
  - Fully burdened costs (\$/hr) and electricity prices (\$/kWh) are taken from Bureau of Labor Statistics<sup>11</sup> and the U.S. Energy Information Administration<sup>12</sup> respectively for each manufacturing location modeled.
4. Sum the costs for all process steps to calculate the total manufacturing cost.
5. Input results from the manufacturing cost model into a *pro forma* discounted cash flow (DCF) model to calculate a minimum sustainable price (MSP)<sup>13,14</sup> for the model device.
  - MSP assumes all overhead costs (R&D, sales, general, and administrative (SG&A)) can be covered, and investors can be paid back at the weight-average cost of capital (WACC).

### 1.3 SCOPE OF THE PRESENT REVIEW

Unfortunately, bottom-up cost models for thin-film devices are difficult to find. In the first instance, they are not often published, to protect cost competitiveness of the companies. Even when these

models are published, not all of the input data is published, making it impossible for readers to replicate the model. Another reason these models are difficult to find is that the literature on techno-economic analysis of vapor-deposited thin films is scattered: these models are often made in order to compare within, and not across, technologies. Thus, researchers using similar TEA methods to analyze different devices rarely reference each other. In this chapter, I review the publicly-available bottom-up cost models for thin-film devices across technologies. In particular, I tabulate and compare the methodology and the technical and financial parameters used across these studies. This compilation may aid other researchers interested in estimating the scaled cost of their thin film technology.

Specifically, the present review focuses on the present-day techno-economics of thin films used as optoelectronic functional material layers in device stacks like solar photovoltaics. I have specifically excluded techno-economic analyses of non-vapor methods to produce, for example, perovskite solar cells.<sup>15</sup> I have also excluded CVD methods to make non-electronic device materials like synthetic diamond<sup>16,17</sup> and carbon nanotubes.<sup>18,19</sup> I have also excluded techno-economic analysis of otherwise relevant materials and processes that are more than two decades out of date: for example, a 1998 techno-economic analysis of optical fibers using vapor deposition techniques<sup>20</sup> and a 1996 techno-economic analysis of APCVD of TiO<sub>2</sub> anti-reflective coatings<sup>21</sup> for silicon solar cells.\* Also excluded from this compilation are relevant, recent articles on vapor-deposited devices that either failed to provide values of input parameters at the vacuum deposition level of detail or utilized the same input parameter numbers as those given in prior work by the same author.<sup>22,23,24</sup>

Some cost models focus on the non-financial costs of the technology. The full cost of a technology over its lifetime includes both internal (financial and non-financial) and external (non-financial) costs. The non-financial internal costs are mainly composed of environmental health and safety

---

\*Modern solar cell anti-reflective coatings (ARCs) are indeed still made of alumina or titania, but today, sputtering is typically considered more cost effective than CVD for ARCs.

(EH&S) costs, i.e., those incurred by the semiconductor manufacturer that can result in not only process or tool problems, but also injury, illness, accidents, and environmental costs that must be paid by the manufacturer. External costs are the costs that are incurred by the society or environment, such as a decrease in water, air, and soil quality, health effects in people, fauna, and flora, the depletion or degradation of natural resources, etc. For internal costs, elements of EH&S can represent as much as 20% of the total costs of manufacturing.<sup>25</sup> Work has been done within the semiconductor manufacturing industry to segment wafer cost analysis through the lens of EH&S, considering internal costs.<sup>26,27,28</sup> External costs have been considered more recently, most commonly through the lens of Life Cycle Analysis.<sup>29,30,31,32,33,34,35,36</sup>

Other modeling and case studies have focused on input parameters external to the technology, such as subsidies, real estate price, the availability of experienced labor, absenteeism, reliability of suppliers for various potential factory locations, uncertainty around quality of supplied material, tariffs and fees associated with locating factories outside of the developed world<sup>37</sup> These broader studies and inventories considering costs beyond financial cost are beyond the scope of the present review.

#### 1.4 REVIEW OF VAPOR-DEPOSITED THIN FILM TECHNO-ECONOMIC ANALYSES

In the present review, five recent techno-economic analyses of thin-film devices are compiled and compared. These articles present techno-economic analyses of solar cells and/or modules (CdTe,<sup>38,39,40</sup> CIGS,<sup>39,40</sup> and GaAs<sup>39,40</sup>) and tungsten oxide thin films.<sup>41</sup> These analyses share a similar breakdown of the cost components, shown in Table 1.1. There are two main components to the total device cost: direct manufacturing costs (aka production costs) and non-manufacturing costs. The direct manufacturing costs are broken down into five categories: material costs, capital equipment, labor, energy, and manufacturing overheads. The material costs are further broken down into two categories: the

thin film cost and other materials (which may include the substrate, encapsulation, and materials used to combine solar cells into modules).

Each of these five studies uses a bottom-up cost modeling treatment for at least some components of the analysis. At least one of the studies, Horowitz et al., also applies a top-down treatment for one component, the non-manufacturing costs.<sup>10</sup> Table 1.1 indicates for the five studies which cost components are modeled using a bottom-up (BU) versus top-down (TD) approach, or whether the approach is unstated (U) in the analysis. A dash (-) indicates that the authors did not model a particular cost segment.

**Table 1.1:** Total device cost model for five techno-economic analyses. BU = bottom-up cost model; U = unstated; TD = top-down cost model.

Total Device Cost								
Direct Manufacturing Costs (aka Production Costs)								Non-Mfg Costs
Ref	Material costs			Capital Equipment	Labor	Energy	Mfg. Overheads	
	Films	Inactive Materials						
	Substrate	Other						
<sup>39</sup>	BU	-	-	-	-	-	-	-
<sup>41</sup>	BU	-	-	BU	BU	BU	-	-
<sup>38</sup>	BU	BU	BU	BU	BU	BU	BU	-
<sup>40</sup>	BU	BU	U	U	U	U	U	U
<sup>10</sup>	BU	BU	-	BU	BU	BU	BU	TD

As is clear from Table 1.1, direct manufacturing costs (aka production costs) of the devices receive more modeling attention than do non-manufacturing costs. This choice is natural within the techno-economic literature, because the estimation and analysis of technical parameters provides a rich base for engagement with and optimization of the technology. Non-manufacturing costs, on the other hand, mainly consist of overheads for the institute creating the device: namely, R&D overhead (estimated at 10% of revenue)<sup>10</sup> and the selling, general, and administrative non-direct labor costs (estimated at 20% of revenue).<sup>10</sup> Accordingly, I focus for the remainder of this review on direct

manufacturing costs.

The four technical components to direct manufacturing costs, as well as financial inputs, will each be reviewed in a subsection of this chapter. First, I provide an overview of the breakdown of the direct manufacturing costs (Subsection 1.4.1). Then, material costs will be compared with a focus on precursor price and precursor utilization (Subsection 1.4.2). Next, capital equipment costs will be reviewed, including tool cost, deposition rates, and tool uptime (Subsection 1.4.3). Subsequently, bottom-up cost estimations of labor will be given, with focus on how labor scales with production capacity of a solar PV factory (Subsection 1.4.4). Next, input values related to electricity use for the sub-components of vapor deposition tools will be presented (Subsection 1.4.5). Finally, financial inputs to the models will be reviewed (Subsection 1.4.6). The fifth component of direct manufacturing costs (also referred to as factory overhead, factory burden, and manufacturing support costs) will not be discussed in its own section. Factory overhead is composed of elements such as factory inspection, maintenance, factory supplies and personnel (other than direct labor), and sometimes includes utilities and electricity depending on the model treatment. None of the techno-economic analyses reviewed here provided values for the factory overhead parameters.

Before delving into the technical parameter values, the caveats on these values bear mentioning, since they were so strongly emphasized in several of the published analyses by the authors. First, the choice of appropriate data to use as input parameters is non-trivial: often technologies are being considered for scale-up and it is not known at the academic lab bench stage what the scaled-up values will be. When this is the case, learning curves from other technologies can be considered, assumptions about scaling the technology can be made, and sometimes data can be found by speaking with private industry experts. However, these experts often work at private companies which forbid public disclosure of technical and economic information. Accordingly, some studies are anonymized, some studies are done in aggregate, and sometimes final output values of the models are published but input values are suppressed. To quote Woodhouse et al.<sup>38</sup> in one quite repre-

sentative description: “the full detailed bill of materials cannot be shown (in order to respect the anonymity of certain collaborators).” Accordingly, the values that appear in the following sections should not be taken as precise.

#### 1.4.1 DIRECT MANUFACTURING COSTS OVERVIEW

As shown in Table 1.1, four of the five analyses modeled several components of the direct manufacturing cost of devices. The cost output of these analyses, compared with industry reports, are shown in Table 1.2. Note that these costs are not all directly comparable: the calendar year of the U.S. dollar value is given in parentheses.

**Table 1.2:** Direct manufacturing costs for thin-film devices. M = module; C = cell. <sup>40</sup>Wuerth Solar disintegrated in between 2010 and 2012. Its installer business was turned over to BayWa and its CIGS line was taken over by Manz.

Reference	Device	Efficiency	Direct Mfg Cost		Production vol.
			(\$/W <sub>p</sub> )	\$/m <sup>2</sup>	
<i>Model Outputs</i>					
Woodhouse <sup>38</sup>	CdTe Module	11.7% (M)	0.74 (2011)	86.58 (2011)	
Candelise <sup>40</sup>	CdTe Module	11.6% (M)	0.75 (2011)	86.87 (2011)	> 100 MW
Candelise <sup>40</sup>	CIGS Module (rotary)	11% (M)	0.84 (2011)	92.4 (2011)	> 100 MW
Candelise <sup>40</sup>	CIGS Module (planar)	11% (M)	0.97 (2011)	106.7 (2011)	> 100 MW
Horowitz <sup>10</sup>	3-J III-V Cell	33% (C)	100 (2017)	33,000 (2017)	50 kW
Horowitz <sup>10</sup>	3-J III-V Cell	33% (C)	70 (2017)	23,100 (2017)	200 kW
Garg <sup>41</sup>	Roll-to-roll WO <sub>3</sub>	n/a	n/a	5.26 (2005)	
Garg <sup>41</sup>	In-line WO <sub>3</sub>	n/a	n/a	8 (2005)	
<i>Industry Reports</i>					
First Solar <sup>42</sup>	CdTe Module	11.7% (M)	0.73 (2011)		
First Solar <sup>43</sup>	CdTe Module	11.6% (M)	0.75 (2011)		
Q-Cell Solibro <sup>44</sup>	CIGS Module		0.80 (2009)		
Wurth Solar <sup>45a</sup>	CIGS Module		1.22 (2010)		

Three types of solar cell materials were modeled in this set of analyses: CdTe, CIGS, and triple-junction (3-J) III-V cells. CdTe modules were evaluated by both Candelise et al.<sup>40</sup> and Woodhouse

et al.<sup>38</sup> Both sets of authors worked closely with industry practitioners, and created models whose outputs of  $\sim \$0.75/W_p$  match the First Solar report from that year (see Table 1.2). The direct manufacturing costs for CdTe and CIGS modules are relatively competitive with each other and these modules are commercially available, comprising around 5% of the global solar PV market. However, 3-J III-V cells are not mass-deployed commercially, and the cost modeling of Horowitz et al. indicates that these cells are still two orders of magnitude too high in cost to compete with CIGS and CdTe in the terrestrial photovoltaics (PV) market.

Beyond PV, one TEA model analyzed components of the cost of a tungsten oxide thin film plasma-enhanced CVD system. Garg et al. found that a roll-to-roll process will be less expensive on a \$ per m<sup>2</sup> basis than an in-line system. This authors did not model the full direct manufacturing cost, choosing only some components (see Table 1.1).

I next provide an example of the quantitative breakdown of the direct manufacturing cost. The most credible studies are those by Woodhouse and Candelise, since the direct manufacturing cost output of their models matches publicly-available data for commercially-available modules. Their cost breakdowns are very similar and their total costs vary by just 0.01 USD; I provide here the breakdown provided by Candelise et al. without substantial loss of generality. The reader is referred to Fig. 2 of Woodhouse et al.<sup>38</sup> for slight variations.

Candelise et al. created a bottom-up cost model of a production plant based in Europe producing CdTe or CIGS modules at a rate higher than 100 MW production capacity (100 MW<sub>p</sub> of panels per year). They assume current “baseline technology” is used to make the panels, naming VTD and CSS for CdTe and several techniques for CIGS. Today, it is known that VTD is used by First Solar for CdTe panels. The cost breakdown for CdTe modules from this study is shown in Table 1.3. In this model, materials are divided into “active components”, i.e., the materials that make up the solar PV layers; and all other materials (substrate, encapsulation, and modularization materials). The non-material cost components are labor, energy, capital, and overheads. Overheads in-



**Table 1.3:** Cost breakdown estimate for commercial CdTe modules made by best-available technology (i.e., vapor transport deposition) by First Solar. Module efficiency is 11.6%; thus, performance is estimated at  $116 W_p/m^2$ . Assumed factory production capacity is above 100 MW per annum. Source: Candelise et al.<sup>40</sup> <sup>a</sup>These percentages of module cost are taken verbatim from Candelise et al., Figure 7, and sum to 101. <sup>b</sup>The ‘other inactive materials’ category includes “encapsulation, modularisation, process gases, packaging and miscellaneous.”<sup>40</sup>

<i>Component</i>	<i>% of module cost</i>	<i>Value (\$/m<sup>2</sup>)</i>	<i>Value (\$/W<sub>p</sub>)</i>
Overheads	5	4.30	0.04
Energy	7	6.02	0.05
Labor	12	10.32	0.09
Other inactive materials <sup>b</sup>	25	21.50	0.19
TCO/Glass	17	14.62	0.13
Active materials	15	12.90	0.11
Capital	20	17.20	0.15
Total	≈100 <sup>a</sup>	87	0.75

clude both manufacturing overheads (maintenance, plant management, facility rent and costs) and non-manufacturing overheads (sales and marketing). The authors emphasize that the cost of the absorber layer material (CdTe or CIGS) is the only cost that can change due to technological innovation. All other costs are collectively referred to as “balance of module” (BOM) costs and are largely unchanged across thin film PV manufacturing plants of similar size and location (although they do vary for different plant sizes and locations).<sup>40</sup> Accordingly, thin film PV manufacturers’ competitiveness stems from their ability to optimize over the trade-offs between manufacturing cost of the active layers and the PV cell efficiency.

Overall, the cost breakdown for the 3-J III-V solar cells (not modules) modeled by Horowitz et al. (Table 1.4) is very similar to the breakdown for the CdTe solar modules. As a caveat, these cost components are not necessarily directly comparable because of the different technology readiness levels (TRLs) and the different device types (III-V cells versus CdTe modules). For both cell types, materials are the majority of the cost: ~57% for CdTe and ~63% for III-V. For both devices, labor represents 12% and capital represents ~20%. Taken together, these three studies giving the direct manufacturing costs of solar PV device production using vapor methods provide a useful bench-

**Table 1.4:** Cost breakdown estimate for research-scale 3-J III-V Cells. Assumed factory production capacity is 200 kW. Source: Horowitz et al. <sup>a</sup>Cell efficiency is 33%; thus, performance is estimated at 330  $W_p/m^2$ . <sup>b</sup>These percentages of module cost are extracted from the top plot of Figure 2 in Horowitz et al and do not add up to the  $\$70/W_{DC}$  given in the text, likely because the authors rounded up to  $\$70$  due to the substantial approximate nature of the model. Accordingly, these values should be considered highly approximate. For example, the  $\$22440/m^2$  value does not match the  $\$23100/m^2$  value given in Table 1.2 because the 22440 value is extracted from this plot.

<i>Component</i>	<i>% of module cost</i>	<i>Value (<math>\\$/m^2</math>)</i>	<i>Value (<math>\\$/W_p</math>)</i>
Maintenance	4	990	3
Equipment + Building	19	4290	13
Electricity	1	330	1
Direct Labor	12	2640	8
Materials	63	14190	43
Total	100	22440 <sup>a</sup>	68 <sup>b</sup>

mark for researchers, highlighting that active materials still represent the largest cost and therefore potentially a fruitful area for research.

#### 1.4.2 MATERIAL COSTS

The inactive materials category accounts for several components: encapsulation and modularization materials, process gases, packaging, and others. These materials individually all each cost less than the “active layer” materials cost. Thus, we conclude that the active layer materials cost is the largest single material contributor to the module cost for most solar stacks. Thus, the cost of this layer is arguably the most important piece of the techno-economic analysis. Correctly modeling the materials costs depends primarily on the amount and cost of the raw materials needed, which depend on the tool-dependent material utilization rate, the recovery rates, the layer thicknesses, and the quality (purity) of the materials. These parameters are next reviewed in turn.

The reported price of precursors in these studies is shown in Table 1.5. These prices are relatively consistent. The reported price of CdTe is between  $\$0.25$ - $\$0.56/g$  (2011 USD) and that of trimethyl-gallium is between  $\$1$ - $\$2.50$ . Estimates for the elements Te, In, and Ga are given at two purity stages:

standard grade and after formed into semiconductor grade targets. The increase in price from the first to the second stage was  $\sim 20\%$  for Ga and In, but much higher and more variable (80-180%) for Te.

The material utilization rates (Table 1.7) varied widely depending on the deposition method and maturity of the technology. Moreover, two independent research groups studying the same processes – CdTe by vapor transport deposition (VTD) – found utilization rates of 40% and 70% respectively. Recovery of the materials for re-use has the potential to decrease active layer materials cost, but recovery processes themselves have costs that must be taken into consideration. Recovery fraction is given in Table 1.8 and reveals that cost-effective recovery strategies are still immature. Overall, these ballpark values for materials cost, layer thickness, and materials utilization/recovery rates indicate that the active layer cost of a device will be highly material- and process-dependent.

### 1.4.3 CAPITAL EQUIPMENT COSTS

The capital expenditure, or capex, refers to the expenses on capital equipment, i.e., the fixed-cost, one-time-purchases of instrumentation needed to deposit the layers – chambers, valves, tubing, pumps, etc. Manufacturing in thin-film solar panel factories is organized in “lines,” which is to say, a single set of all the equipment needed to make a panel. The process to make a panel is continuous and highly automated, taking, for example, about 2.5 hours in the case of CdTe panels made by First Solar.<sup>47</sup> Often, one determines the capital expenditure per unit device, or in the cases studied here, unit  $W_p$  of solar module or  $W_{DC}$  of solar cell. To determine this unit cost, one must model how many devices can be produced per line per time. The technical parameters needed to determine this rate – device per tool per time – are the tool uptime, the deposition rate, and the yield rate.

The three reported deposition rates from the present studies are given in Table 1.9, and range from 1 nm - 10 nm/sec. Yield is defined differently in different studies, but it is broadly defined as the number of good devices produced to total devices produced. In these studies, yield fraction ranges

**Table 1.5:** Materials price input parameters to vapor deposition techno-economic models.

Ref	Precursors	Price	Year	Notes from the Reference
<i>Precursors</i>				
<sup>40</sup>	CdTe powder	\$0.38/g	2011	From personal communication; this value is for larger players; small/medium plants are charged \$0.42/g (2011)
<sup>39</sup>	CdTe	\$0.26/g	2011	Total price to make CdTe into the target needed for VTD
<sup>38</sup>	CdTe compound	\$0.41-\$0.56/g	2011	Assumes large volumes purchased
<sup>39</sup>	Te	\$0.15/g	2011	Price for Te when purchased at commonly-traded, standard grade of purity
<sup>38</sup>	Te	\$0.28 - \$0.43/g	2011	Price for Te after purified
<sup>39</sup>	Indium	\$0.52/g	2011	Price for element when purchased at commonly-traded, standard grade of purity
<sup>39</sup>	Indium target	\$0.62/g	2011	Total price to make the element into precursor needed for this deposition method
<sup>10</sup>	Trimethylindium (TMI)	\$12/g	2017	
<sup>39</sup>	Gallium	\$0.40/g	2011	Price for element when purchased at commonly-traded, standard grade of purity
<sup>39</sup>	Gallium target	\$0.50/g	2011	Total price to make the element into precursor needed for this deposition method
<sup>10</sup>	Trimethylgallium (TMG)	\$1/g	2017	Prices as low as \$0.45/g for Chinese manufacturing (of LEDs and other devices) have been reported.
<sup>39</sup>	Trimethylgallium (TMG)	\$2.5/g	2011	
<sup>41</sup>	WF <sub>6</sub> price	\$0.0003/g	2005	99.999% pure; cheaper if less pure
<sup>40</sup>	Indium target	\$1.4/g	2011	Reflects technical grade indium price of \$0.685/g
<sup>10</sup>	Arsine (AsH <sub>3</sub> )	\$0.44/g	2017	
<sup>10</sup>	Phosphine (PH <sub>3</sub> )	\$0.35/g	2017	
<sup>10</sup>	Gold (Au)	\$43/g	2017	Au is ~ 100× more expensive than Ag
<sup>10</sup>	Silver (Ag)	\$0.55/g	2017	
<i>Process Gases</i>				
<sup>41</sup>	Liquid argon	\$1.66/L	2005	
<sup>41</sup>	Liquid oxygen	\$0.62/L	2005	
<sup>41</sup>	Liquid nitrogen	\$0.23/L	2005	

**Table 1.6:** Layer thicknesses for TE models. 1-J = single-junction.

Ref	Layer	Thickness
41	WO <sub>3</sub>	400 nm
39	CdTe	2.5 μm
40	CdTe	2.1 μm
	CdTe (absorber)	2.5 μm
	CdS	0.05 - 0.15 μm
38	TCO	0.2 - 0.5 μm
	Back contact	1 μm
	Glass superstrate	3 mm
39	CIGS	2 μm
39	1-J GaAs via MOCVD	2.5 μm
39	1-J GaAs via HVPE	2.5 μm

from 80-100% (Table 1.10) and in general the semiconductor industry has state of the art practices at very high yield levels ( $\sim 99.999\%$ ).<sup>48</sup>

Finally, tool uptime must be taken into account. The tool will not be able to deposit at its deposition rate continuously for a year, but rather requires maintenance and, at the very least, sample loading, unloading, and heat-up and cool-down time. Such parameters are estimated in Table 1.11.

The deposition tool upfront cost will be highly specific to the process, depending on heat requirements, vacuum level, type of reaction initiation (plasma, etc.), and throughput, i.e., how many devices can be fabricated simultaneously in the tool. CVD tool costs between \$3M-\$8M are given in Table 1.12. Finally, the tool cost is combined with the yield fraction, deposition rate, and tool uptime data to determine the capex per some unit of produced device, e.g. per m<sup>2</sup> or per W<sub>p</sub>. These values are shown in Table 1.13. The CdTe capex is equivalent to about \$15-\$17/m<sup>2</sup> (2011 USD), which represents 20% of the direct manufacturing cost of the module.

**Table 1.7:** Material utilization rates discussed in TE models. The reader is referred to the references for further details.

Ref	Material	Utilization Rate	Notes from References
41	WF <sub>6</sub> (proportion that reacts, of total)	60%	PECVD
41	WF <sub>6</sub> (proportion in deposited film, of total WF <sub>6</sub> )	28%	
41	WF <sub>6</sub> (proportion on chamber walls, of total WF <sub>6</sub> )	32%	
40	CIGS sputter-based deposition process (rotary target)	50%	
39,46	Te in CdTe via VTD	70%	VTD = vapor transport deposition Generally reported to be up to 70%; however, estimates of material supplied to First Solar in 2008 give 40%
40	CdTe via VTD	40%	
40	CIGS sputter-based deposition process (planar target)	33%	
10	TMG	30%	
10	TMI	30%	
38	CdTe utilization rate	90%	
39	CIGS sputter-based deposition process (rotary target)	55%	Takes into account both rotary target utilization and transfer efficiency to the module; this is a representative collection fraction for the co-evaporation approach to CIGS module manufacturing
39	Ga in GaAs via MOCVD	30%	This value was provided by a relevant equipment supplier.
39	Ga in GaAs via HVPE	30%	Value unknown; value given here is a guess in line with known utilization rate for GaAs via CVD

**Table 1.8:** Mole recovery fraction of materials not in film.

Ref	Element	Recovery fraction	Notes from References
<sup>39</sup>	Indium, in CIGS sputter-based deposition process	25%	
<sup>39</sup>	Gallium, in CIGS sputter-based deposition process	25%	
<sup>39</sup>	Ga in GaAs via MOCVD	0%	Ga not currently recovered from these 2 processes (research-stage investigations)
<sup>39</sup>	Ga in GaAs via HVPE	0%	
<sup>39,46</sup>	Te, in CdTe by vapor transport deposition	20%	Recovery fraction that is reclaimed and used

**Table 1.9:** Deposition rates of thin film layers.

Ref	Material	Deposition Rate	
		$\mu\text{m/hr}$	nm/sec
<sup>41</sup>	WO <sub>3</sub>	36	10
<sup>10</sup>	GaAs	15	4
<sup>10</sup>	InGaP	4	1

**Table 1.10:** Device yield for various production processes.

Ref	Material, Dep. Technique	Yield	Notes from References
<sup>41</sup>	WO <sub>3</sub> by PECVD	80%	
<sup>40</sup>	CdTe Module by vapor transport deposition	90%	In 2003, was reported to be 70% and in 2009, 90%
<sup>10</sup>	1-J, 2-J III-V cells by MOCVD	100%	
<sup>10</sup>	3-J III-V cell by MOCVD	80%	

**Table 1.11:** Parameters to estimate tool uptime. <sup>a</sup>Aggressive value claimed achievable by Applied Films and Von Ardenne.

Ref	Category	Parameter Description	Value
<sup>10</sup>	Time btwn runs	Heat/cool + pump/vent time for MOCVD	30 min
<sup>41</sup>	Cleaning	Max film thickness that can be deposited before cleaning	1.5 mm
	Load lock cycle time	PECVD in-line system load lock cycle time <sup>a</sup>	30 sec
	Maintenance	Annual maintenance downtime for PECVD tool	552 h
	Repair	Number of repairs needed for PECVD tool	24/yr
	Time btwn chamber cleaning	If no source change needed, for PECVD tool	9.5 h
		If source change needed, for in-line PECVD tool	13 h
		If source change needed, for roll-to-roll PECVD tool	11.6 h

**Table 1.12:** Capex of individual vapor deposition tools.

Ref	Tool	Year	Tool cost	Tool cost per film area	Notes from References	Production Volume
<sup>10</sup>	MOCVD Tool	2018	\$2.8M		Includes installation and auxiliary costs	200 kW which is 3800 6-inch wafers/month
<sup>10</sup>	Lithography Tool	2018	\$1M to \$2.5M		Includes installation and auxiliary costs	
<sup>41</sup>	PECVD Tool, roll-to-roll	2005	\$6.8M	\$0.30/m <sup>2</sup>	For roll-to-roll PECVD system.	1.4 million m <sup>2</sup>
<sup>41</sup>	PECVD Tool, in-line	2005	\$8.3M			



**Table 1.13:** Total capex for solar techno-economic models. <sup>40</sup>Production volume for solar production factories is also known as total annualized run rate. It represents the yearly amount of panels in megawatt (MW) produced by one line. In business contexts, the “peak” designation,  $MW_p$ , is left off.

	Device	Item	Year	Capex per $W_p$	Capex per film area	Production Volume <sup>40</sup>
<sup>40</sup>	CdTe Module (11.6% efficient)	Equipment only	2011	$\$0.15/W_p$	$\$17.20/m^2$	> 100 MW
<sup>10</sup>	3-J LM III-V Cell (33% efficient)	Equipment + Building	2018	$\$13/W_{DC}$	$\$4,290/m^2$	200 kW which is 3800 6-inch wafers/month
<sup>38</sup>	CdTe Module (11.7% efficient)	Equipment + Building	2011	$\$0.13/W_p$	$\$15.21/m^2$	

#### 1.4.4 LABOR COSTS

Three types of data were provided by the five techno-economic analyses. One analysis, Garg et al., provided values for inputs to the model for labor time, shown in Table 1.14. Another analysis, Horowitz et al., provided values for labor rates at  $\$14/hr$  for unskilled labor and  $\$25/hr$  for skilled labor, stating that these vary by location and were meant to represent a mid-cost location in the U.S. Finally, two analyses provided values regarding employees per solar production capacity: Woodhouse et al. and Horowitz et al., as shown in Table 1.15. The values for employees per MW vary by about 50x because Horowitz et al. model a very small production capacity of between 50 - 200 kW for a cell that is not mass-produced, whereas Woodhouse et al. model a production capacity at least 1000x larger for a module that is mass-produced, thus achieving greater economies of scale.

**Table 1.14:** Parameters to estimate labor and tool uptime. All these parameters are from Garg et al. <sup>41</sup>

Parameter	Value
Technician time needed per repair	8 h
Technician time needed for annual maintenance	552 h
Loading each 2 m × 3 m glass sheet	30 s of time from 2 people
Operator presence for PECVD tool	100% of tool uptime
Process engineer presence for PECVD tool	During 100% of startup phase and available for 50% of other time

**Table 1.15:** Estimates of labor amount per solar production capacity.

Ref	Quoted value	Employees per MW	Location
<sup>38</sup>	600 employees per 250 MW added capacity	2.4	Vietnam and Mesa, Arizona
<sup>10</sup>	10 full time equivalent direct laborers per 100 kW/yr of cells produced	100	Mid-cost location in the U.S.

#### 1.4.5 ENERGY COSTS

Few of the analyses modeled energy costs. Only one analysis, Garg et al., provided input values for the model relating to electricity use; these are reproduced in Table 1.16. Two analyses provided energy as an independent component of the direct manufacturing cost breakdown of the device: Candelise et al. found that energy represented 7% of module cost (see Table 1.2) and Horowitz et al. found that energy represented about 1.4% of cell cost (see Table 1.4). Woodhouse et al. also modeled electricity costs, but they did not provide any input parameters and their value for the contribution of electricity to direct manufacturing cost of a CdTe cell is included as an all-utilities value representing 4% of module cost (see Figure 2 of Woodhouse et al.<sup>38</sup>).

**Table 1.16:** Chemical vapor deposition equipment power usage, reproduced from Garg et al.<sup>41</sup>

Equipment	Power Usage
Diffusion pump	72 kW
Mechanical pump	5.5 kW
Blower stacks	26 kW
Controls	6 kW
Heaters	60 kW
Drive motors	3.9 kW

#### 1.4.6 FINANCIAL INPUTS TO THE MODELS

Financial parameters must be combined with technical parameters to enable techno-economic analysis. Shown in Table 1.17 are the example parameters for depreciation, weighted annual cost of capital (WACC), and tax and inflation rates given in the present studies. Some financial parameters are more straightforward, like state and federal tax rates. Others are estimates, like annual predicted inflation rate or depreciation of instrumentation value over time. Overall, these values support the evaluation of investment decisions for these vapor deposition technologies.

**Table 1.17:** Financial parameters for TEA analysis.

Parameter	Ref	Value	Notes from References
Equipment depreciation			
PECVD Tool	<sup>41</sup>	10 years	Straight-line
MOCVD, Lithography, etc.	<sup>10</sup>	5 years	Straight-line
CIGS/CdTe equipment	<sup>40</sup>	7 years	
Building depreciation	<sup>10</sup>	20 years	Straight-line
Weighted annual cost of capital	<sup>10</sup>	14.80%	Consistent with what has been estimated for other PV manufacturing companies
	<sup>38</sup>	19%	Estimated for a successful PV company to seek finance construction of new capacity; WACC includes cost of equity but many reported PV module manufacturing costs may not
Combined state and federal tax rate	<sup>10</sup>	25.70%	
Inflation rate	<sup>10</sup>	2%	

Taken together, the parameters described in this literature survey are illustrative for the purposes of enabling researchers to develop their own techno-economic models. This literature survey both outlines a state-of-the-art existing techno-economic analysis method, and identifies benchmark values for technical parameters important in vapor deposition technologies. Overall, techno-economic analysis helps focus research objectives on aspects of the technology that will be the most commer-

cially impactful. In particular, based on this chapter, I find that the most impactful areas for academic research related to thin-film technologies are: (1) to develop alternatives to the high-cost “active materials” (Cd, Ga, In, Te) that are prevalent in thin-film solar panels and (2) to decrease the deposition tool cost (amortized per saleable device). These concepts inform my experimental work in the remainder of the dissertation.

## 1.5 PRESENTATION AND SCOPE OF THESIS

This thesis presents the results of my research studying and developing novel chemical vapor deposition techniques, with an emphasis on imparting desired properties to materials for next-generation photovoltaic and electronic devices. To this end, Chapters 2 and 3 detail two methods that I have co-invented to prepare thin films of the p-type semiconductor cuprous bromide. Chapter 2 describes a two-step anion exchange conversion method, in which thin films of cuprous chalcogenides can be partially or fully converted to cuprous bromide via exposure to HBr gas. Chapter 3 describes the direct chemical vapor deposition of cuprous bromide thin films by reaction between HBr gas and vinyltrimethylsilane(hexafluoroacetylacetonato)copper(I). Finally, Chapter 4 describes work to design and co-polymerize a hybrid organic-ceramic dielectric material using chemical vapor deposition (CVD). Taken together, these chapters advance knowledge in the field of chemical vapor deposition.

## References

- [1] J.-O. Carlsson and P. M. Martin, “Chemical Vapor Deposition,” in *Handbook of Deposition Technologies for Films and Coatings*, vol. 3, p. 60, 2010.
- [2] N. Alvi, “Equipment Modeling: A Tool To Cost Reduction,” *International Symposium on Semiconductor Manufacturing, Extended Abstracts of ISSM*, pp. 123–128, 1994.
- [3] W. Houf, J. Grcar, and W. Breiland, “A model for low pressure chemical vapor deposition in a hot-wall tubular reactor,” *Materials Science and Engineering: B*, vol. 17, pp. 163–171, Feb. 1993.
- [4] G. D. Hutcheson, “VLSI—An Economist’s Viewpoint,” *Proceedings of the ASEE Conference*, Jan. 1981.
- [5] G. D. Hutcheson, *A Capital Investment Model for the Semiconductor Industry*. MS thesis, San Jose State University, Dec. 1984.
- [6] R. Doering and Y. Nishi, eds., *Handbook of Semiconductor Manufacturing Technology*. Boca Raton: CRC Press, 2nd ed ed., 2008. OCLC: ocm77476656.
- [7] M. Sandholzer and M. Wouters, “The history of the standard for the calculation of cost of ownership in the semiconductor industry,” *Accounting History*, vol. 24, pp. 62–82, Feb. 2019.
- [8] K. Geissdörfer, R. Gleich, and A. Wald, “Potentials of standardizing life cycle cost analysis models for strategic cost management,” *Zeitschrift für Betriebswirtschaft*, vol. 79, pp. 693–715, June 2009.
- [9] S. Ragona, “Analyzing component manufacturing costs using the SEMI-E35 standard for cost of ownership (COO),” *Opto-Canada: SPIE Regional Meeting on Optoelectronics, Photonics, and Imaging*, p. 182, Aug. 2017.
- [10] K. A. Horowitz, T. W. Remo, B. Smith, and A. J. Ptak, “A Techno-Economic Analysis and Cost Reduction Roadmap for III-V Solar Cells,” Tech. Rep. NREL/TP–6A20–72103, 1484349, National Renewable Energy Lab, Nov. 2018.
- [11] Bureau of Labor Statistics, “Overview of BLS Wage Data by Area and Occupation,” 2017.

- [12] EIA, “Electricity Data,” Mar. 2018.
- [13] K. A. W. Horowitz and M. Woodhouse, “Cost and potential of monolithic CIGS photovoltaic modules,” *Proceedings of the 42nd IEEE Photovoltaic Specialists Conference*, 2015.
- [14] D. M. Powell, R. Fu, K. Horowitz, P. A. Basore, M. Woodhouse, and T. Buonassisi, “The capital intensity of photovoltaics manufacturing: Barrier to scale and opportunity for innovation,” *Energy & Environmental Science*, vol. 8, no. 12, pp. 3395–3408, 2015.
- [15] Z. Li, Y. Zhao, X. Wang, Y. Sun, Z. Zhao, Y. Li, H. Zhou, and Q. Chen, “Cost Analysis of Perovskite Tandem Photovoltaics,” *Joule*, vol. 2, pp. 1559–1572, Aug. 2018.
- [16] J. V. Busch and J. P. Dismukes, “Trends and market perspectives for CVD diamond,” *Diamond and Related Materials*, vol. 3, pp. 295–302, Apr. 1994.
- [17] A. Singer, “Polycrystalline CVD diamond in electronics: Important cost factors,” *1994 Proceedings. 44th Electronic Components and Technology Conference*, pp. 279–285, 1994.
- [18] A. E. Agboola, R. W. Pike, T. A. Hertwig, and H. H. Lou, “Conceptual design of carbon nanotube processes,” *Clean Technologies and Environmental Policy*, vol. 9, pp. 289–311, Nov. 2007.
- [19] J. Hernández-Vargas, J. Martínez-Gómez, J. B. González-Campos, J. Lara-Romero, and J. M. Ponce-Ortega, “An optimization approach for producing carbon nanotubes involving economic and safety objectives,” *Clean Technologies and Environmental Policy*, vol. 17, pp. 2185–2195, Dec. 2015.
- [20] A. Sarkar, “Economics of single-mode fiber production using MCVD and VAD processes,” *International Conference on Fiber Optics and Photonics: Selected Papers from Photonics India '98*, pp. 18–22, Apr. 1999.
- [21] D. C. Wong and A. Waugh, “Cost Impacts of Anti-Reflection Coatings on Silicon Solar Cells,” *MRS Proceedings*, vol. 426, p. 503, 1996.
- [22] K. A. Horowitz, R. Fu, and M. Woodhouse, “An analysis of glass–glass CIGS manufacturing costs,” *Solar Energy Materials and Solar Cells*, vol. 154, pp. 1–10, Sept. 2016.
- [23] K. A. W. Horowitz, R. Fu, X. Sun, T. Silverman, M. Woodhouse, and M. A. Alam, “Estimating the Effects of Module Area on Thin-Film Photovoltaic System Costs,” *2017 IEEE 44th Photovoltaic Specialist Conference (PVSC)*, pp. 1259–1263, June 2017.
- [24] A. C. Tamboli, D. C. Bobela, A. Kanevce, T. Remo, K. Alberi, and M. Woodhouse, “Low-Cost CdTe/Silicon Tandem Solar Cells,” *IEEE Journal of Photovoltaics*, vol. 7, pp. 1767–1772, Nov. 2017.

- [25] R. Helms and J. Shaw, "Basic Research Needs for Environmentally Responsible Technologies for the Future (Electronics Industry)," tech. rep., National Science Foundation and Dept. of Energy, Washington, D.C., 1996.
- [26] SIA, "The National Technology Roadmap for Semiconductors. Technology Needs," tech. rep., Semiconductor Industry Association, 1997.
- [27] A. Veltri, D. Dance, and M. Nave, "SH&E Life-Cycle Cost Model: An internal study from the semiconductor manufacturing industry," *Professional Safety*, vol. 48, pp. 23–32, June 2003.
- [28] V. Tipnis, "Towards a comprehensive methodology for competing on ecology: How to integrate competitive strategy and corporate financial objectives with life cycle, environmental impact and improvement analyses?," *Proceedings of 1994 IEEE International Symposium on Electronics and The Environment*, pp. 139–148, 1994.
- [29] N. Krishnan, S. Boyd, J. Rosales, D. Dornfeld, S. Raoux, and R. Smati, "Using a hybrid approach to evaluate semiconductor life cycle environmental issues: A case study in interconnect module impacts," in *IEEE International Symposium on Electronics and the Environment, 2004. Conference Record. 2004*, (Scottsdale, AZ, USA), pp. 86–90, IEEE, 2004.
- [30] E. D. Williams, R. U. Ayres, and M. Heller, "The 1.7 Kilogram Microchip: Energy and Material Use in the Production of Semiconductor Devices," *Environmental Science & Technology*, vol. 36, pp. 5504–5510, Dec. 2002.
- [31] S. Hermanns, "Using the LCA method for identifying resource conservation priorities at AMD saxony," in *NSF/SRC Center for Environmentally Benign Semiconductor Manufacturing Tele-Seminar*, 2002.
- [32] K. Schischke, M. Stutz, J.-P. Ruelle, H. Griese, and H. Reichl, "Life cycle inventory analysis and identification of environmentally significant aspects in semiconductor manufacturing," in *Proceedings of the 2001 IEEE International Symposium on Electronics and the Environment. 2001 IEEE ISEE (Cat. No. 01CH37190)*, pp. 145–150, IEEE, 2001.
- [33] R. Smati, S. Raoux, D. Ho, and M. Woolston, "Measuring and modeling gas consumption and emissions from semiconductor manufacturing processes," *EHS Assessment Techniques, SEMICON West*, 2002.
- [34] C. F. Murphy, G. A. Kenig, D. T. Allen, J.-P. Laurent, and D. E. Dyer, "Development of parametric material, energy, and emission inventories for wafer fabrication in the semiconductor industry," *Environmental Science & Technology*, vol. 37, no. 23, pp. 5373–5382, 2003.
- [35] C. F. Murphy, J.-P. Laurent, and D. T. Allen, "Life cycle inventory development for wafer fabrication in semiconductor manufacturing," in *IEEE International Symposium on Electronics and the Environment, 2003*, pp. 276–281, IEEE, 2003.

- [36] N. Krishnan, S. Thurwachter, T. Francis, and P. Sheng, "A modular environmental design and decision-support tool (EDDT) for semiconductor manufacturing," in *Proceedings from SEMICON West Improving Environmental Performance of Wafer Manufacturing Processes*, 2000.
- [37] E. Fuchs and R. Kirchain, "Design for Location? The Impact of Manufacturing Offshore on Technology Competitiveness in the Optoelectronics Industry," *Management Science*, vol. 56, pp. 2323–2349, Dec. 2010.
- [38] M. Woodhouse, A. Goodrich, R. Margolis, T. James, R. Dhere, T. Gessert, T. Barnes, R. Eggert, and D. Albin, "Perspectives on the pathways for cadmium telluride photovoltaic module manufacturers to address expected increases in the price for tellurium," *Solar Energy Materials and Solar Cells*, vol. 115, pp. 199–212, Aug. 2013.
- [39] M. Woodhouse, A. Goodrich, R. Margolis, T. L. James, M. Lokanc, and R. Eggert, "Supply-chain dynamics of tellurium, indium and gallium within the context of PV module manufacturing costs," *2012 IEEE 38th Photovoltaic Specialists Conference (PVSC) PART 2*, pp. 1–6, June 2012.
- [40] C. Candelise, M. Winkler, and R. Gross, "Implications for CdTe and CIGS technologies production costs of indium and tellurium scarcity: Effects of indium and tellurium scarcity," *Progress in Photovoltaics: Research and Applications*, vol. 20, pp. 816–831, Sept. 2012.
- [41] D. Garg, P. Henderson, R. Hollingsworth, and D. Jensen, "An economic analysis of the deposition of electrochromic WO<sub>3</sub> via sputtering or plasma enhanced chemical vapor deposition," *Materials Science and Engineering: B*, vol. 119, pp. 224–231, June 2005.
- [42] R. Gillette, M. Widmar, and L. Polizzotto, "Q1 2011 First solar earnings call," 2011.
- [43] First Solar, "First Solar Datasheet Q1 2011," Mar. 2011.
- [44] T. Cheyney, "CIGS spelled with a Q(Cells): Solibro's Segner speaks of production prowess, supplier shortcomings," *PV Tech online magazine*, Nov. 2009.
- [45] B. Dimmler, "Presentation," in *European PV Solar Energy Conference*, (Valencia, Spain), Sept. 2010.
- [46] V. Fthenakis, "Long-term estimates of primary & secondary sources of thin-film PV materials-Recycling and sustainability of PV," in *Presentation at PV Velocity Forum: Supply and Economics in Thin-Film PV Materials*, 2010.
- [47] W. Grossmann, K. W. Steininger, C. Schmid, and I. Grossmann, "Investment and employment from large-scale photovoltaics up to 2050," *Empirica*, vol. 39, pp. 165–189, May 2012.



- [48] C. Su and C. Chou, "A systematic methodology for the creation of Six Sigma projects: A case study of semiconductor foundry," *Expert Systems with Applications*, vol. 34, pp. 2693–2703, May 2008.

# 2

## Vapor deposition of copper(I) bromide films via a two-step conversion process

[The following chapter is derived in part from R. Heasley, C. M. Chang, L. M. Davis, K. Liu, R. G. Gordon, *Journal of Vacuum Science & Technology A* 35, 01B109 (2017).]\*

---

\*R. Heasley and C. Chang contributed equally to this work.

## 2.1 ABSTRACT

Thin films of  $\text{Cu}_2\text{S}$  grown by pulsed-chemical vapor deposition of bis( $N,N'$ -di-*sec*-butylacetamidinato)dicopper(I) and hydrogen sulfide were converted to CuBr upon exposure to anhydrous hydrogen bromide. X-ray diffraction shows that the as-deposited films have a polycrystalline  $\text{Cu}_2\text{S}$  structure. After exposure to HBr gas, the surface of the films is transformed to a  $\gamma$ -CuBr polycrystalline structure. Scanning electron microscopy and X-ray photoelectron spectroscopy reveal complete conversion of up to 100 nm of film. However, when the conversion to CuBr approaches the interface between as-deposited  $\text{Cu}_2\text{S}$  and the  $\text{SiO}_2$  substrate, the morphology of the film changes from continuous and nanocrystalline to sparse and microcrystalline.

## 2.2 INTRODUCTION

Research into photovoltaics employing a perovskite absorber layer (formula  $\text{ABX}_3$ , in which  $\text{A} = \text{CH}_3\text{NH}_3^+$ ,  $\text{CH}(\text{NH}_2)_2^+$ ;  $\text{B} = \text{Pb}_2^+$ ,  $\text{Sn}_2^+$ ; and  $\text{X} = \text{I}^-$ ,  $\text{Br}^-$ ,  $\text{Cl}^-$ ) has seen dramatic growth in the past 7 years, yielding an increase in power conversion efficiency from 3.8 % in 2009<sup>1</sup> to 25.2 % in 2019.<sup>2</sup> One limiting factor in the commercial development of complete perovskite solar cells is the high cost of the hole-transport material (HTM).<sup>3</sup> The HTM is a p-type semiconductor layer that extracts positive charges (holes) from the perovskite absorber and transfers them to the back contact. Currently, the most efficient perovskite solar cells use the HTM 2,2',7,7'-tetrakis( $N,N$ -di-*p*-methoxyphenylamine)-9,9'-spirobifluorene (spiro-OMeTAD), the synthesis of which is complex and requires extensive, costly purification.<sup>4</sup> The spiro-OMeTAD HTM is usually deposited by spin coating, which typically incorporates only ca. 5% of the expensive starting material<sup>5</sup> and produces nonconformal films.<sup>6</sup> To compensate for this lack of conformality, a HTM of spiro-OMeTAD must be at least 150 nm thick to prevent shunting between the absorber and the back contact of the cell.<sup>7</sup> In contrast, inorganic HTMs can be deposited by vacuum techniques that require significantly less

material to fully coat an underlying surface. Indeed, a solar cell with a power conversion efficiency greater than 10% can be produced using only 5 nm of an inorganic HTM.<sup>8</sup> It is clear that the current usage of a thick and prohibitively expensive organic HTM is far from ideal. The development of a suitable alternative to the spiro-OMeTAD HTM is imperative for the commercial development of perovskite photovoltaics.

One class of materials that might provide an inexpensive HTM is copper(I) halides. Cuprous iodide (CuI) has been used successfully in a perovskite solar cell,<sup>9,10</sup> with devices exhibiting power conversion efficiencies of up to 13.6%.<sup>11</sup> Cuprous bromide (CuBr) also shows promise: it is a p-type semiconductor with a hole concentration on the order of  $10^{16} \text{ cm}^{-3}$  and a hole mobility of  $0.4 \text{ cm}^2 \text{ V}^{-1} \text{ s}^{-1}$ .<sup>12</sup> The p-type conductivity is thought to originate from copper vacancies and oxygen doping.<sup>12</sup> CuBr features a wide bandgap of 2.9 eV, which would prevent parasitic light absorption during use in a solar cell.<sup>13</sup> Films of CuBr have been deposited previously by vacuum evaporation,<sup>14</sup> molecular beam epitaxy,<sup>15</sup> r.f. sputtering,<sup>16</sup> and spin-coating.<sup>17</sup>

Chemical vapor deposition (CVD) is a more appealing growth process for HTMs because it can produce films with high thickness uniformity and conformality over large areas of deposition. However, previous research in this lab indicates that direct CVD of metal halides is not well controlled when highly acidic hydrogen halide precursors (HX, with X = Cl, Br, I) are used. The reaction between HX and a metalorganic precursor does in fact produce the desired metal halide material by transferring a proton from HX to the anionic ligand of the metalorganic precursor, thereby releasing the neutral form of the ligand to be evacuated. However, CVD processes continuously supply both precursor vapors, allowing excess HX to protonate the newly released ligand a second time if that free ligand is basic. This acid-base reaction forms a ligand-hydrogen halide salt that is incorporated into the resultant film. For example, X-ray photoelectron spectroscopy (XPS) performed on nominal CuBr deposited by pulsed-CVD reveals carbon and nitrogen contamination consistent with the acetamidinium bromide salt, as shown in Figure 2.1.

Atomic layer deposition (ALD) is a type of CVD that separates the introduction of precursor vapors by purging with an inert gas and evacuating after each exposure. ALD is known as “self-limiting” because film growth proceeds by cycles of alternating precursor exposures and continues in each cycle only until surface reactive sites are depleted.<sup>18</sup> The precursor also does not react with its own fragments, which enables the depletion of surface reactive sites. It seems plausible that pure metal halide films could be deposited by this method given that the sequential nature of ALD would prevent the exposure of a basic ligand to a strong hydrogen halide acid. However, in an ideal ALD sequence, the hydrogen halide exposure step produces a halide-terminated surface, which means that no surface reactive sites are available for the next cycle of metalorganic precursor exposure. This limitation could be overcome if either the hydrogen halide or the metal precursor were able to adsorb to the film surface strongly enough to remain through the purge and evacuation steps. Previous research in this lab demonstrating the failure of ALD to produce any film under a variety of conditions indicates that this strong adsorption does not occur for the copper compound bis(*N,N'*-di-*sec*-butylacetamidinato)dicopper(I), [Cu(*s*Bu<sub>2</sub>AMD)]<sub>2</sub>. With regard to hydrogen halides, it has been shown that strong adsorption on metal halide surfaces occurs only for HF, as a result of the formation of bifluoride (FHF<sup>-</sup>) anions on the surface.<sup>19</sup> Adsorption of other hydrogen halides to a metal halide film is too weak to bind the molecule to the surface during purging and evacuation.<sup>19</sup> As such, we see no direct route to ALD of metal halides (with the exception of fluorides) using metalorganic precursors and hydrogen halide reactants. Indeed, an ALD process to produce PbI<sub>2</sub> films has recently been reported, and it does not utilize HI.<sup>20</sup>

Given the obstacles to the direct deposition of metal halides by CVD or ALD, the development of an alternative method for vapor deposition of CuBr and other halides is needed. Here, a novel route to the vapor deposition of pure CuBr by a two-step process is presented. A film of Cu<sub>2</sub>S is first deposited by a pulsed-CVD reaction between [Cu(*s*Bu<sub>2</sub>AMD)]<sub>2</sub> and hydrogen sulfide.<sup>21</sup> This film is then exposed to anhydrous hydrogen bromide gas while held at a temperature of 60 °C. XPS

reveals that the HBr exposure is able to fully convert at least 100 nanometers of the deposited  $\text{Cu}_2\text{S}$  to CuBr. Structural and morphological properties of the resultant CuBr films are presented and discussed.

## 2.3 MATERIALS AND METHODS

### 2.3.1 FILM GROWTH

$\text{Cu}_2\text{S}$  and CuBr films were grown in a custom-built, hot-walled ALD reactor similar in design to those described in previous work.<sup>22</sup> Films were deposited on  $1'' \times 1''$  substrates of Si with a 300-nm surface layer of  $\text{SiO}_2$  grown by wet oxidation. Substrates were sequentially rinsed in semiconductor-grade acetone and isopropanol (BDH,  $\geq 99\%$ ) and then dried in a nitrogen gas stream. The substrates were then treated with UV-ozone for 5 minutes to promote the formation of surface hydroxyl groups.

Thin films of  $\text{Cu}_2\text{S}$  were deposited via pulsed-CVD using exposures to  $[\text{Cu}(s\text{Bu}_2\text{AMD})]_2$  (Dow Chemical Company, synthesis first reported by Li et al.<sup>23</sup>) and  $\text{H}_2\text{S}$  (Airgas, 4 wt.% in  $\text{N}_2$ ). Both precursors were used as received and the  $[\text{Cu}(s\text{Bu}_2\text{AMD})]_2$  was loaded into a vacuum bubbler under a nitrogen atmosphere to prevent decomposition in air. The  $[\text{Cu}(s\text{Bu}_2\text{AMD})]_2$  vapor was transferred to the reactor chamber by a purified nitrogen carrier gas held at a pressure of 10 Torr in the bubbler. The  $[\text{Cu}(s\text{Bu}_2\text{AMD})]_2$  and  $\text{H}_2\text{S}/\text{N}_2$  reactants were mixed together in a region  $1''$  in length and  $0.57''$  in diameter before reaching the substrate holder. Swagelok ALD valves operated by LabView executed the pulsed-CVD recipes. Pulsed-CVD is similar to ALD, but omits the purging step between precursor doses. The timing sequence used for the  $\text{Cu}_2\text{S}$  recipe may be expressed as  $t_1 - t_2 - t_3 - t_4 - t_5$ , where  $t_1$  is the exposure time of the  $[\text{Cu}(s\text{Bu}_2\text{AMD})]_2$  precursor,  $t_2$  is the exposure time of the  $\text{H}_2\text{S}/\text{N}_2$  mixture,  $t_3$  is a waiting period during which all valves are closed and deposition occurs,  $t_4$  is the nitrogen purge time, and  $t_5$  is the evacuation time, with all times given in

seconds. The timing sequence was 1-1-30-10-30 for all Cu<sub>2</sub>S depositions. [Cu(*s*Bu<sub>2</sub>AMD)]<sub>2</sub> was delivered at a partial pressure of 0.025 Torr for a total exposure of 0.85 Torr-sec and the H<sub>2</sub>S/N<sub>2</sub> mixture was delivered at a pressure of 2.6 Torr for a total H<sub>2</sub>S exposure of 3.2 Torr-sec. The bubbler temperature of [Cu(*s*Bu<sub>2</sub>AMD)]<sub>2</sub> was maintained at 130 °C while the substrate temperature was varied from 100-200 °C. The inlet and outlet of the reactor tube furnace were heated to temperatures from 100-150 °C by Omega FGH heating tape regulated by an Omega miniature benchtop proportional-integral-derivative controller.

After completion of the Cu<sub>2</sub>S deposition, the films were removed from the reactor and the substrate temperature was adjusted to 30 °C, 60 °C, or 180 °C. Half of the as-deposited films were stored under N<sub>2</sub> atmosphere for future characterization and half were returned to the reactor after a brief (ca. 5 minutes) air exposure. At this point, conversion to CuBr proceeded via repeated exposures to anhydrous HBr (MilliporeSigma, ≥ 99%, used as received). The HBr was introduced by a 1-second pulse at a pressure of 1.3 Torr followed by a 30-second wait period with all valves closed. The total HBr exposure was 36 Torr-sec. This was followed by a 10-second N<sub>2</sub> purge and 30-second evacuation. The repeated purging and evacuation steps were implemented to ensure the removal of generated H<sub>2</sub>S and the continuation of the forward conversion reaction. The number of cycles was typically 484, which corresponds to about 4 hours of total exposure to HBr. Although the films do not appear to oxidize or hydrolyze in air, all as-deposited and converted samples were stored under N<sub>2</sub> atmosphere except during analysis.

### 2.3.2 FILM CHARACTERIZATION

Electron microscopy and energy dispersive X-ray spectroscopy (EDS) were performed in a Zeiss Supra 55 scanning electron microscope (SEM). X-ray diffraction (XRD) patterns were recorded in a Bruker D2 PHASER X-ray diffractometer using Cu K $\alpha$  radiation ( $\lambda = 1.542 \text{ \AA}$ ) and a  $\theta$ - $2\theta$  scan. X-ray photoelectron spectroscopy (XPS) was performed on a Thermo Scientific K-Alpha spectrometer

equipped with a monochromated Al K $\alpha$  X-ray source, 12 kV electron beam, and Ar<sup>+</sup> sputtering gun. Depth profiles were collected by sputtering at 500 eV for 50 seconds per level, unless otherwise stated. The XPS sputtering rate was determined by dividing the film thickness as determined by SEM by the total sputtering time before the SiO<sub>2</sub> substrate was detected.

## 2.4 RESULTS AND DISCUSSION

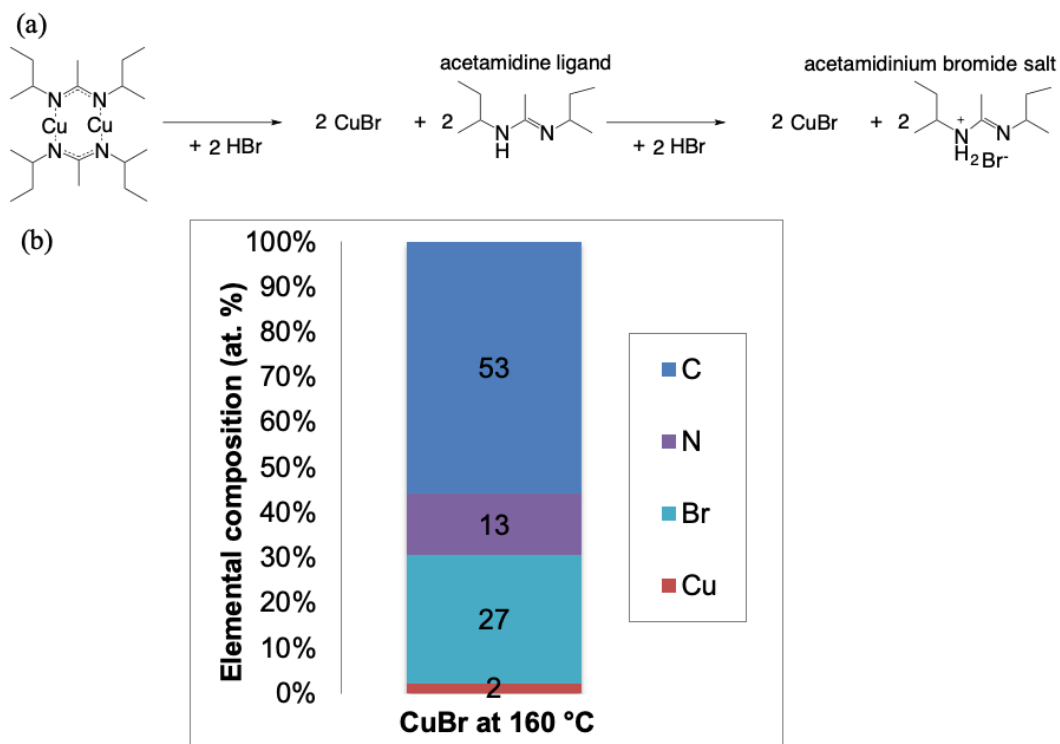
### 2.4.1 LIGAND SALT-CONTAMINATED FILM

Figure 2.1a depicts the reaction of HBr with [Cu(*s*Bu<sub>2</sub>AMD)]<sub>2</sub>, followed by an acid-base reaction between excess HBr and the demetallated acetamidine ligand. Because HBr is a strong acid and amidines are bases, this reaction is very favorable. Figure 2.1b shows the elemental composition of a nominally CuBr film deposited by direct pulsed-CVD between [Cu(*s*Bu<sub>2</sub>AMD)]<sub>2</sub> and HBr at 160 °C, as determined by XPS survey spectra after 45 seconds of Ar<sup>+</sup> sputtering. The overall composition is suggestive of the acid-base reaction illustrated in Figure 2.1a and the measured C:N ratio of 53:13 is within error of the expected C:N ratio of 5:1 for the acetamidinium bromide salt.

### 2.4.2 GROWTH AND CHARACTERIZATION OF CUPROUS SULFIDE FILMS

The growth of Cu<sub>2</sub>S was optimized across several variables with the ultimate goal of producing a pure, continuous film of uniform thickness. Pulsed-CVD was chosen as the deposition method for its accelerated growth rate relative to ALD.<sup>24</sup> XPS survey spectra reveal that depositions conducted between 120 °C and 180 °C produced films containing solely copper and sulfur, whereas films deposited at 100 °C or 200 °C also contain carbon. The film depicted in Figure 2.2a was deposited at a substrate temperature of 100 °C and the film depicted in Figure 2.2b was deposited at a substrate temperature of 200 °C. Both films contain a significant amount of carbon, which is likely due to incomplete reaction of the precursor at 100 °C and thermal decomposition at 200 °C. The film





**Figure 2.1:** (a) The reaction of  $[\text{Cu}(\text{sBu}_2\text{AMD})_2]_2$  and HBr to form CuBr, followed by the acid-base reaction between excess HBr and the singly protonated ligand to form the acetamidinium bromide salt. (b) The elemental composition of a CuBr film deposited at a growth temperature of  $160 \text{ }^\circ\text{C}$  by p-CVD as determined by an XPS survey spectrum obtained after 45 seconds of  $\text{Ar}^+$  sputtering.

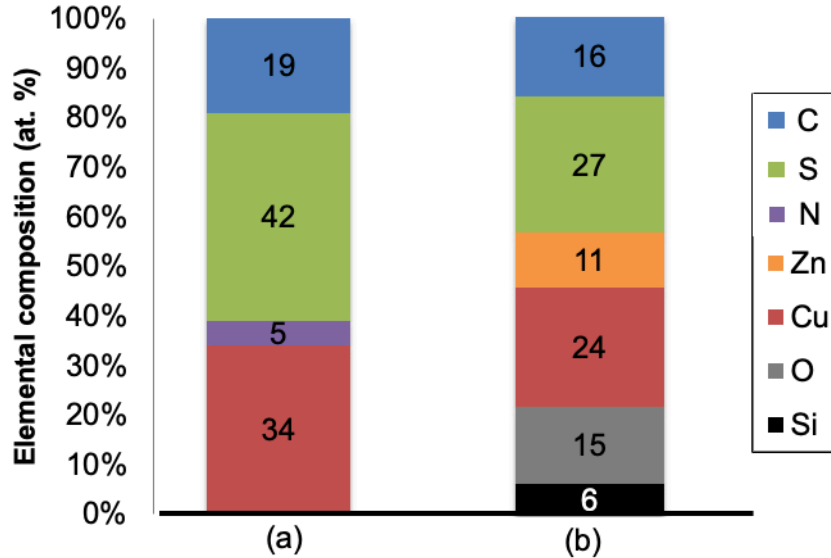


**Figure 2.2:** The elemental compositions of films of  $\text{Cu}_2\text{S}$  deposited at (a) 100 °C and (b) 200 °C as derived from XPS survey spectra obtained after 45 seconds of  $\text{Ar}^+$  sputtering.

deposited at 200 °C also contains zinc, which was unintentionally introduced by a volatile contaminant within the ALD reactor itself. XPS survey spectra reveal only Cu and S for films deposited at temperatures between 100 °C and 200 °C.

Depositions conducted between 120 °C and 180 °C produced films containing solely copper and sulfur. As evidenced by electron micrographs, growth proceeds by island coalescence. Figures 2.3a-c compare pulsed-CVD  $\text{Cu}_2\text{S}$  films after 322 cycles of growth at 180 °C, 150 °C, and 120 °C, respectively. In these depositions, the temperature at the inlet of the reactor tube, ca. 1'' from the substrate, was set to 150 °C, 120 °C, and 100 °C, respectively. As the progression from Figure 2.3a to 2.3c shows, surface coverage increases as substrate and inlet temperatures decrease. Of particular significance is Figure 2.3c, which demonstrates that the reaction between  $[\text{Cu}(\text{iBu}_2\text{AMD})]_2$  and  $\text{H}_2\text{S}$  proceeds even at the low temperature of 120 °C. This high reactivity implies that if the inlet of the reactor tube is heated to 120 °C or greater, film deposition can occur in the mixing region before the precursors reach the substrate holder. As such, the observed reduction in surface coverage for higher

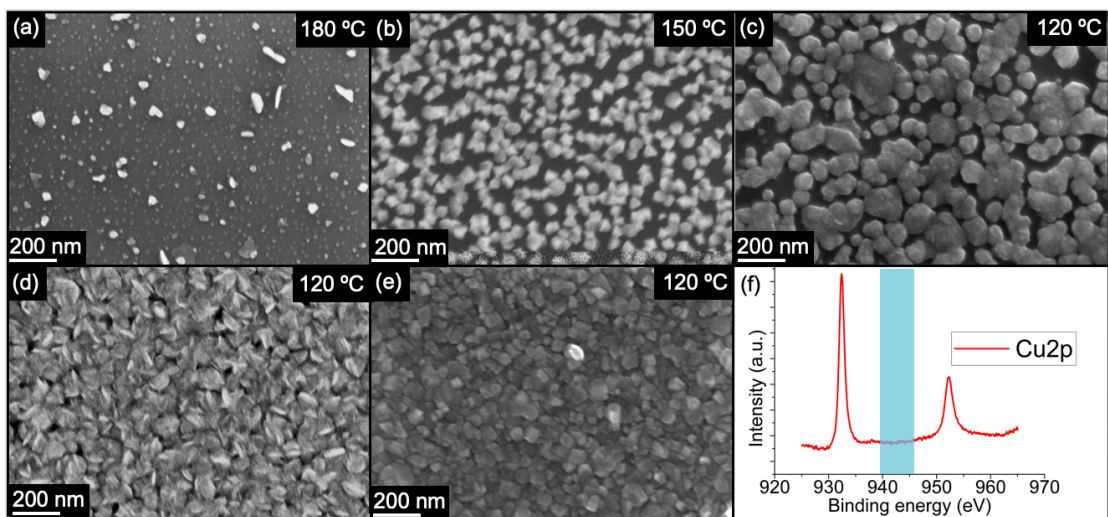


**Figure 2.3:** SEM images of  $\text{Cu}_2\text{S}$  film coverage after 322 cycles at a growth temperature of (a)  $180^\circ\text{C}$ , (b)  $150^\circ\text{C}$ , and (c)  $120^\circ\text{C}$ .  $120^\circ\text{C}$  was selected for its superior film coverage and  $\text{Cu}_2\text{S}$  films were deposited for (d) 400 and (e) 500 cycles. A high-resolution XPS scan of the  $\text{Cu}2p$  region shown in (f) gives no indication of the  $\text{Cu}^{2+}$  satellite peak typically observed at 943 eV (highlighted region).

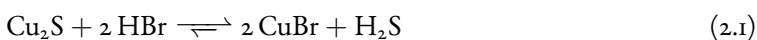
growth temperatures likely results from significant film deposition in the mixing region, owing to the higher corresponding inlet temperature. Much of the delivered precursor is therefore consumed upstream of the  $\text{SiO}_2$  substrates. The reaction proceeds more slowly at an inlet temperature of  $100^\circ\text{C}$ , which limits the deposition in the mixing region and leads to higher surface coverage of  $\text{Cu}_2\text{S}$  at a substrate temperature of  $120^\circ\text{C}$ . High-quality films of  $\text{Cu}_2\text{S}$  can also be grown more quickly at this temperature by pulsed-CVD with the waiting period  $t_3 = 1$  second, as well as by standard ALD.

Figures 2.3d and 2.3e show the morphology of  $\text{Cu}_2\text{S}$  films deposited at  $120^\circ\text{C}$  over 400 and 500 cycles, respectively. At this temperature, film closure occurs between 322 and 500 cycles and the growth per cycle ranges from 1.1 to 1.7  $\text{\AA}/\text{cycle}$ , with the higher values calculated from thicker films. This large variation in growth per cycle at a single temperature is likely due to a relatively higher amount of film deposited per cycle during steady-state  $\text{Cu}_2\text{S}$  deposition as compared with initial nucleation. The existence of separate nucleation and bulk deposition growth regimes is relatively common in ALD and CVD processes.<sup>25,26,27,28</sup> Figure 2.3f is a high-resolution XPS spectrum of the

Cu 2p peak obtained after 45 seconds of Ar<sup>+</sup> sputtering. While C and O are detected at the surface of the deposited films, these contaminants are removed after 45 seconds of Ar<sup>+</sup> sputtering and the absence of the characteristic Cu<sup>2+</sup> satellite peak at 943 eV confirms copper is present as Cu<sup>+</sup> throughout the film.<sup>29</sup>

### 2.4.3 CONVERSION TO CUPROUS BROMIDE

After optimization of the Cu<sub>2</sub>S growth process, experiments were conducted to convert the Cu<sub>2</sub>S film to pure CuBr. The deposited films of Cu<sub>2</sub>S were exposed to anhydrous HBr in accordance with the reaction described in Equation 2.1:



The thermodynamic favorability of the conversion of Cu<sub>2</sub>S to CuBr was determined by calculating the sign of the change in Gibbs free energy from:

$$\Delta G = \Delta H - T\Delta S \quad (2.2)$$

Using tabulated  $\Delta H_f$  and S values for HBr,<sup>30</sup> CuBr,<sup>31</sup> Cu<sub>2</sub>S,<sup>32,33</sup> and H<sub>2</sub>S<sup>30</sup> at 60 °C, it is straightforward to use Hess's law and Equation 2.2 to show that  $\Delta G = -40 \text{ kJ/mol} < 0$  and the conversion of Cu<sub>2</sub>S to CuBr upon exposure to HBr is thermodynamically favorable at 60 °C. Films of Cu<sub>2</sub>S with a range of thicknesses from 60 to 400 nm were first prepared. These films were then heated to 60 °C and exposed to 484 pulses of HBr at a pressure of 1.3 Torr, amounting to a total exposure time of 4 hours. The variation in atomic composition through the thickness of the converted films was measured by a depth profile within the XPS. Figure 2.4 shows the incomplete conversion of a 400-nm thick film of Cu<sub>2</sub>S. As evidenced by the presence of Br, the HBr was able to penetrate through hundreds of nanometers of the film, fully converting the top 100 nm to CuBr (highlighted

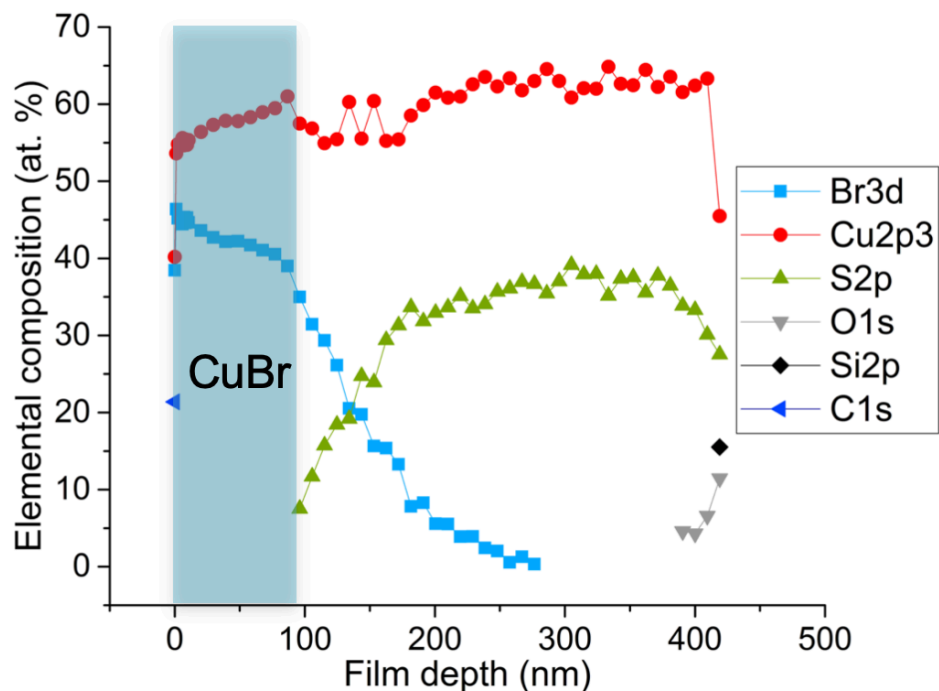


Figure 2.4: Depth profile obtained by XPS of a film converted from a 400-nm thick film of  $\text{Cu}_2\text{S}$  via HBr exposure at 60 °C.

region). After this top 100 nm is removed by sputtering, sulfur becomes detectable by XPS and the film transitions gradually to predominantly  $\text{Cu}_2\text{S}$ . Oxygen and silicon from the  $\text{SiO}_2$  substrate become visible after the full 400-nm thickness is removed.

The forward reaction in Equation 2.1 is slightly more exergonic at 30 °C ( $\Delta G = -42$  kJ/mol versus -40 kJ/mol) and does proceed, but the penetration depth of the HBr is shallower, with 9 hours of exposure resulting in only 25 nm of CuBr at the surface, as shown in the XPS depth profile in Figure 2.5. At 30 °C, the reaction is kinetically limited and conversion proceeds much more slowly than at 60 °C.

Conversion of  $\text{Cu}_2\text{S}$  to CuBr is further evidenced by XRD analysis before and after HBr exposure. Figure 2.6 presents the diffractograms of the as-deposited  $\text{Cu}_2\text{S}$  film and the same film after a 4-hour exposure to HBr at 60 °C. Figure 2.6a shows that the as-deposited  $\text{Cu}_2\text{S}$  films are crystalline

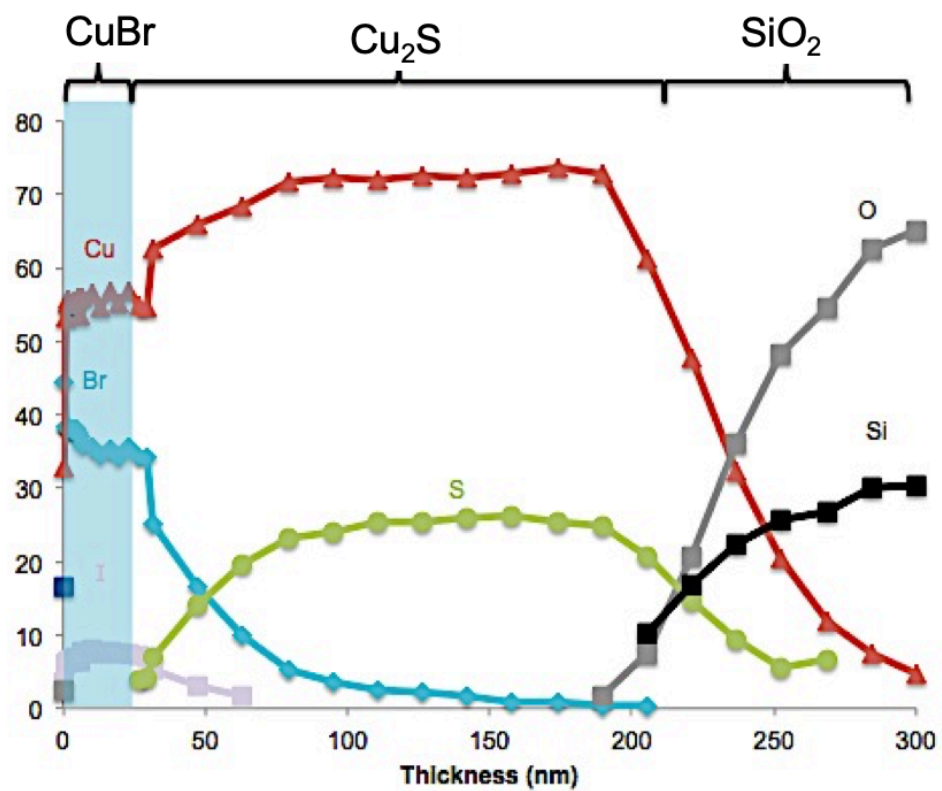
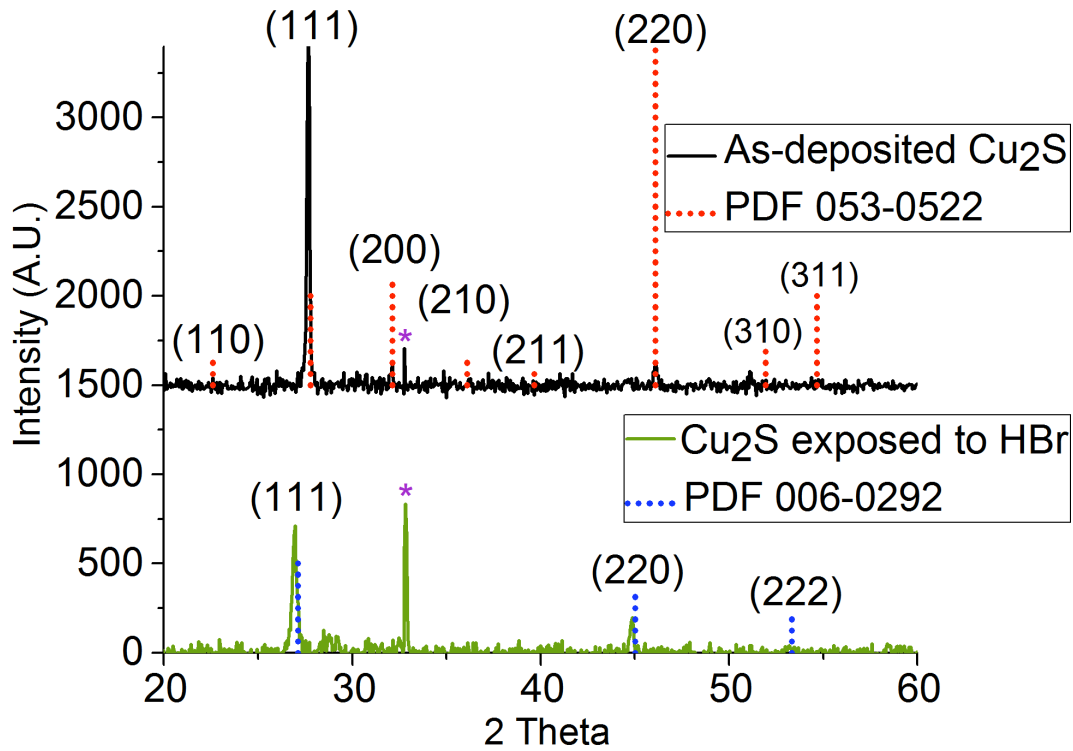


Figure 2.5: Depth profile obtained by XPS of a film converted from a 400-nm thick film of Cu<sub>2</sub>S via HBr exposure at 30 °C.



**Figure 2.6:** X-ray diffraction patterns of as-deposited 250 nm thick  $\text{Cu}_2\text{S}$  film (top) and the same film after conversion of the top 100 nm to  $\text{CuBr}$  via a 4-hour exposure to HBr at  $60^\circ\text{C}$  (bottom). The asterisk (\*) denotes a background peak associated with the XRD instrument itself.

and highly oriented. The experimental pattern best matches PDF 53-0522 for cubic  $\text{Cu}_2\text{S}$ , though the expected crystal structure for  $\text{Cu}_2\text{S}$  formed at  $120^\circ\text{C}$  is the hexagonal high-chalcocite.<sup>34</sup> This discrepancy may be due to the significant impact of small deviations in stoichiometry on the resultant crystal structure of  $\text{Cu}_2\text{S}$  films, which complicates the precise crystallographic analysis of this material by XRD.<sup>35</sup> Figure 2.6b illustrates the measured XRD pattern of the same  $\text{Cu}_2\text{S}$  film following the HBr exposure, which matches PDF 006-0292 for  $\gamma\text{-CuBr}$ . Both the as-deposited and converted films appear to be (111)-oriented.

The film morphology was also influenced by the duration and temperature of the HBr exposures.

HBr exposure tests were conducted at 30 °C, 60 °C, and 180 °C with a total exposure time of either 4 or 10 hours. These two parameters control the extent of the conversion. The use of longer HBr exposures or higher reaction temperatures resulted in a greater volume of Cu<sub>2</sub>S converted to CuBr. Electron micrographs in Figure 2.7 show the variation in film morphology produced by these changes in exposure conditions. For shorter HBr exposure times or lower reaction temperatures, the converted CuBr formed as a surface layer that appeared rougher than the as-deposited Cu<sub>2</sub>S, but remained continuous. However, for longer exposures or higher reaction temperatures, the conversion of Cu<sub>2</sub>S progressed farther into the film and two distinct morphologies developed.

The SEM image in Figure 2.7b illustrates these morphologies. The upper layer is comprised of uncoalesced, 1 μm-sized grains, and the layer beneath is comprised of 200-nm grains. Both layers are discontinuous, though the large grains of the top layer are more spatially separated than the smaller grains underneath. Figure 2.7f shows a similar discontinuous morphology, except the grains of the top layer are smaller. Two-dimensional EDS mapping shown in Figure 2.8 confirms that the larger grains at the surface are composed of copper and bromine, whereas the smaller grains beneath are composed of copper and sulfur. The SiO<sub>2</sub> substrate is also visible through the converted film.

The thickness of the as-deposited Cu<sub>2</sub>S affects the morphology of the converted CuBr. Figures 2.7c and 2.7f show films of Cu<sub>2</sub>S with different initial thicknesses that have been exposed to HBr for 10 hours at 60 °C. The 400-nm thick film of Figure 2.7c has a smooth, continuous surface of CuBr (visible in cross-section in Figure 2.7d), whereas the 60-nm thick film of Figure 2.7f has developed the discontinuous morphology. Table 2.1 contains the atomic composition of the films imaged in Figure 2.7 as determined by XPS survey spectra conducted after 30 seconds of Ar<sup>+</sup> sputtering. The surface of the film imaged in Fig. 2.7c is exclusively composed of copper and bromine, whereas for the film in Fig. 2.7f, copper and bromine are detected, but also sulfur and the silicon and oxygen of the SiO<sub>2</sub> substrate. From these results, it appears that the conversion of Cu<sub>2</sub>S to CuBr upon exposure to HBr proceeds until enough of the Cu<sub>2</sub>S is consumed that the SiO<sub>2</sub> surface is exposed. At



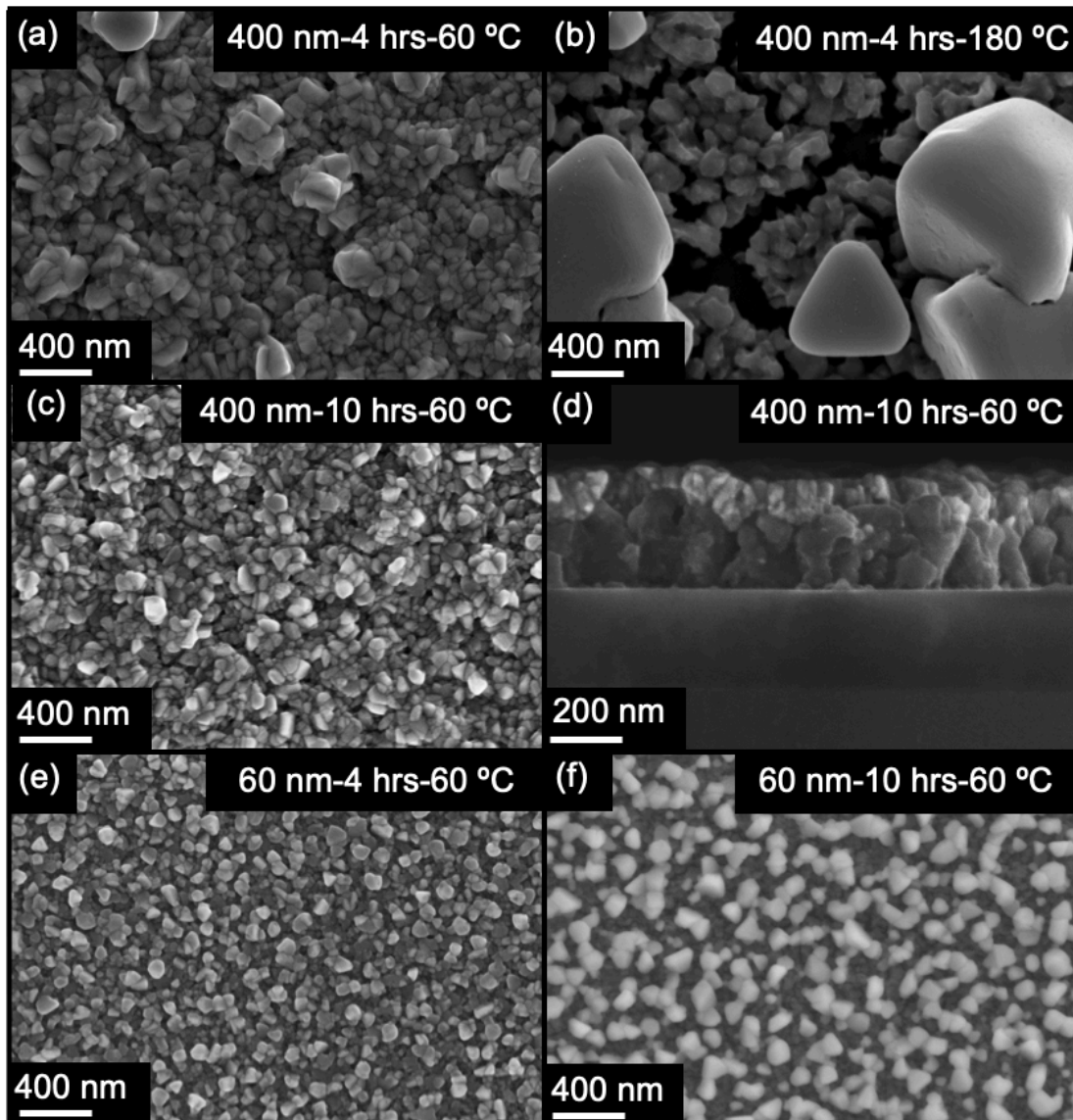


**Figure 2.7:** SEM images of Cu<sub>2</sub>S films with initial thickness  $x$ , exposed to HBr for  $y$  hours at a temperature of  $z$  °C (denoted  $x - y - z$ ) (a) 400 nm-4 hrs-60 °C; (b) 400 nm-4 hrs-180 °C; (c) 400 nm-10 hrs-60 °C; (d) 400 nm-10 hrs-60 °C imaged in cross-section; (e) 60 nm-4 hrs-60 °C; (f) 60 nm-10 hrs-60 °C.

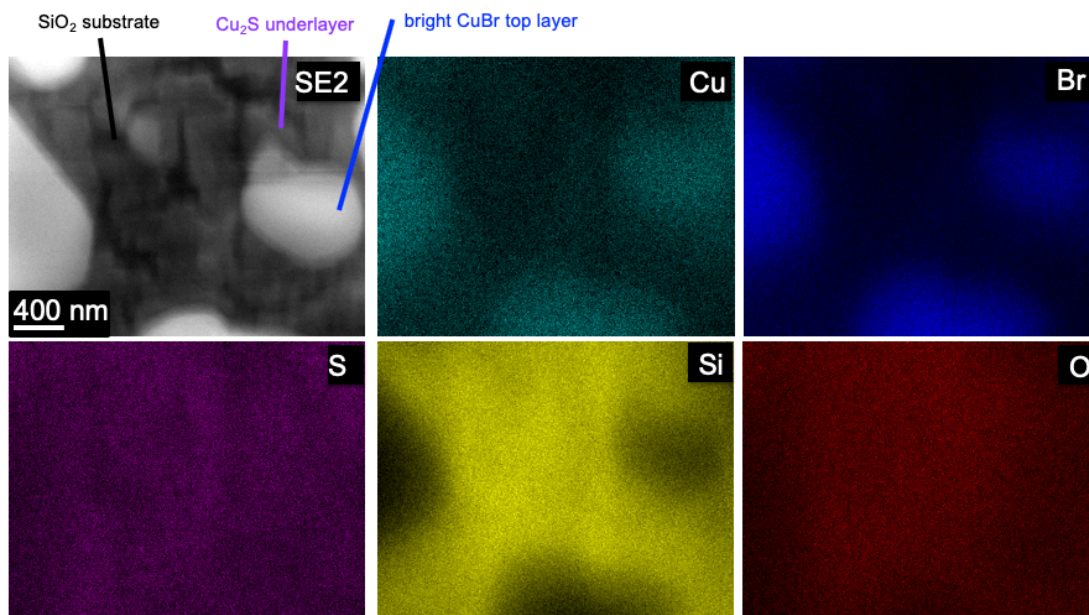


**Figure 2.8:** EDS composition mapping of a 400-nm thick film of  $\text{Cu}_2\text{S}$  exposed to HBr for 4 hours at  $180\text{ }^\circ\text{C}$ .

this point, the CuBr agglomerates into larger grains on the surface of the remaining  $\text{Cu}_2\text{S}$ . This result suggests that the surface energy of the partially converted film is minimized when CuBr- $\text{Cu}_2\text{S}$  and CuBr-CuBr interactions are favored over CuBr- $\text{SiO}_2$  interactions. Thinner as-deposited films of  $\text{Cu}_2\text{S}$  require shorter HBr exposures and lower reaction temperatures to develop the discontinuous morphology, which is consistent with this hypothesis, as there is less  $\text{Cu}_2\text{S}$  to convert before the  $\text{SiO}_2$  surface is exposed. Research is ongoing to find a substrate that will allow a film of  $\text{Cu}_2\text{S}$  to be converted completely to a thin, continuous film of CuBr. The next chapter discusses a related body of experimental work that informs this ongoing research.

## 2.5 CONCLUSION

Thin films of CuBr were deposited by a two-step process, starting with the growth of  $\text{Cu}_2\text{S}$  by pulsed-CVD of bis( $N,N'$ -di-sec-butylacetamidinato)dicopper(I) and hydrogen sulfide at temper-

**Table 2.1:** As-deposited Cu<sub>2</sub>S film thicknesses, subsequent HBr exposure parameters, and elemental composition measured by XPS survey spectra after 30 seconds of Ar<sup>+</sup> sputtering.

As-deposited thickness (nm)	Exposure duration (hours)	Exposure temperature (°C)	Cu (at.%)	Br (at.%)	S (at.%)	Si (at.%)	O (at.%)
400	4	60	54	46			
400	4	180	45	35	14	2.5	4.5
400	10	60	56	45			
60	4	60	54	46			
60	10	60	41	9	29	11	10

atures ranging from 100 °C to 200 °C. A growth temperature of 120 °C produced crystalline Cu<sub>2</sub>S films with carbon and oxygen contents below the detection limit of XPS. These Cu<sub>2</sub>S films were then converted to CuBr by exposure to anhydrous hydrogen bromide at 60 °C. The reaction produced films of pure, crystalline (111)-oriented  $\gamma$ -CuBr. The morphology of the resultant CuBr was dependent on the proximity of the growth front to the SiO<sub>2</sub> substrate, with much larger grains forming in a discontinuous arrangement when the substrate was exposed. This sulfide-to-bromide conversion process is in principle generalizable to the preparation of halides of many different metals. Our findings regarding the poor wetting of CuBr on SiO<sub>2</sub> also point the way toward research that will enable better wetting of CuBr on alternate substrates. Our research on this topic is described in the next chapter, as well as in the PhD dissertation of Dr. Rachel Heasley<sup>36</sup> and a journal article.<sup>37</sup>

## References

- [1] A. Kojima, K. Teshima, Y. Shirai, and T. Miyasaka, "Organometal Halide Perovskites as Visible-Light Sensitizers for Photovoltaic Cells," *Journal of the American Chemical Society*, vol. 131, pp. 6050–6051, May 2009.
- [2] NREL, "Best Research-Cell Efficiencies," 2019.
- [3] K. Rakstys, M. Saliba, P. Gao, P. Gratia, E. Kamarauskas, S. Paek, V. Jankauskas, and M. K. Nazeeruddin, "Highly Efficient Perovskite Solar Cells Employing an Easily Attainable Bifluorenylidene-Based Hole-Transporting Material," *Angewandte Chemie International Edition*, vol. 55, pp. 7464–7468, June 2016.
- [4] M. Saliba, S. Orlandi, T. Matsui, S. Aghazada, M. Cavazzini, J.-P. Correa-Baena, P. Gao, R. Scopelliti, E. Mosconi, K.-H. Dahmen, F. De Angelis, A. Abate, A. Hagfeldt, G. Pozzi, M. Graetzel, and M. K. Nazeeruddin, "A molecularly engineered hole-transporting material for efficient perovskite solar cells," *Nature Energy*, vol. 1, p. 15017, Jan. 2016.
- [5] S.-R. Tseng, H.-F. Meng, K.-C. Lee, and S.-F. Horng, "Multilayer polymer light-emitting diodes by blade coating method," *Applied Physics Letters*, vol. 93, p. 153308, Oct. 2008.
- [6] E. Yenilmez, Q. Wang, R. J. Chen, D. Wang, and H. Dai, "Wafer scale production of carbon nanotube scanning probe tips for atomic force microscopy," *Applied Physics Letters*, vol. 80, pp. 2225–2227, Mar. 2002.
- [7] G.-W. Kim, D. V. Shinde, and T. Park, "Thickness of the hole transport layer in perovskite solar cells: Performance versus reproducibility," *RSC Advances*, vol. 5, no. 120, pp. 99356–99360, 2015.
- [8] W. Yu, F. Li, H. Wang, E. Alarousu, Y. Chen, B. Lin, L. Wang, M. N. Hedhili, Y. Li, K. Wu, X. Wang, O. F. Mohammed, and T. Wu, "Ultrathin  $\text{Cu}_2\text{O}$  as an efficient inorganic hole transporting material for perovskite solar cells," *Nanoscale*, vol. 8, no. 11, pp. 6173–6179, 2016.
- [9] J. A. Christians, R. C. M. Fung, and P. V. Kamat, "An Inorganic Hole Conductor for Organo-Lead Halide Perovskite Solar Cells. Improved Hole Conductivity with Copper Iodide," *Journal of the American Chemical Society*, vol. 136, pp. 758–764, Jan. 2014.

- [10] G. A. Sepalage, S. Meyer, A. Pascoe, A. D. Scully, F. Huang, U. Bach, Y.-B. Cheng, and L. Spiccia, "Copper(I) Iodide as Hole-Conductor in Planar Perovskite Solar Cells: Probing the Origin of  $J - V$  Hysteresis," *Advanced Functional Materials*, vol. 25, pp. 5650–5661, Sept. 2015.
- [11] W.-Y. Chen, L.-L. Deng, S.-M. Dai, X. Wang, C.-B. Tian, X.-X. Zhan, S.-Y. Xie, R.-B. Huang, and L.-S. Zheng, "Low-cost solution-processed copper iodide as an alternative to PEDOT:PSS hole transport layer for efficient and stable inverted planar heterojunction perovskite solar cells," *J. Mater. Chem. A*, vol. 3, no. 38, pp. 19353–19359, 2015.
- [12] P. Knauth, Y. Massiani, and M. Pasquinelli, "Semiconductor Properties of Polycrystalline CuBr by Hall Effect and Capacitive Measurements," *physica status solidi (a)*, vol. 165, pp. 461–465, Feb. 1998.
- [13] M. Altarawneh, A. Marashdeh, and B. Z. Dlugogorski, "Structures, electronic properties and stability phase diagrams for copper(I/II) bromide surfaces," *Physical Chemistry Chemical Physics*, vol. 17, no. 14, pp. 9341–9351, 2015.
- [14] A. Cowley, F. O. Lucas, E. Gudimenko, M. M. Alam, D. Danieluk, A. L. Bradley, and P. J. McNally, "Electroluminescence of  $\gamma$ -CuBr thin films via vacuum evaporation deposition," *Journal of Physics D: Applied Physics*, vol. 43, p. 165101, Apr. 2010.
- [15] A. Yanase and Y. Segawa, "Two different in-plane orientations in the growths of cuprous halides on MgO(001)," *Surface Science*, vol. 329, pp. 219–226, May 1995.
- [16] J.-L. Seguin, M. Bendahan, G. Lollmun, M. Pasquinelli, and P. Knauth, "Preparation of thin films of copper(I) bromide by r.f. sputtering: Morphology and electrical properties," *Thin Solid Films*, vol. 323, pp. 31–36, June 1998.
- [17] H. Zhu, A. Liu, and Y.-Y. Noh, "Transparent Inorganic Copper Bromide (CuBr) p-Channel Transistors Synthesized From Solution at Room Temperature," *IEEE Electron Device Letters*, vol. 40, pp. 769–772, May 2019.
- [18] S. M. George, "Atomic Layer Deposition: An Overview," *Chemical Reviews*, vol. 110, pp. 111–131, Jan. 2010.
- [19] R. S. C. Smart and N. Sheppard, "Infrared Spectroscopic Studies of Adsorption on Alkali Halide Surfaces. I. HCl, HBr and HI on Fluorides, Chlorides, Bromides and Iodides," *Proceedings of the Royal Society of London A: Mathematical, Physical and Engineering Sciences*, vol. 320, pp. 417–436, 1971.
- [20] G. Popov, M. Mattinen, T. Hatanpää, M. Vehkamäki, M. Kemell, K. Mizohata, J. Räisänen, M. Ritala, and M. Leskelä, "Atomic Layer Deposition of PbI<sub>2</sub> Thin Films," *Chemistry of Materials*, vol. 31, pp. 1101–1109, Feb. 2019.

- [21] A. B. F. Martinson, J. W. Elam, and M. J. Pellin, "Atomic layer deposition of Cu<sub>2</sub>S for future application in photovoltaics," *Applied Physics Letters*, vol. 94, p. 123107, Mar. 2009.
- [22] D. M. Hausmann, P. de Rouffignac, A. Smith, R. Gordon, and D. Monsma, "Highly conformal atomic layer deposition of tantalum oxide using alkylamide precursors," *Thin Solid Films*, vol. 443, pp. 1–4, Oct. 2003.
- [23] Z. Li, S. T. Barry, and R. G. Gordon, "Synthesis and Characterization of Copper(I) Amidinates as Precursors for Atomic Layer Deposition (ALD) of Copper Metal," *Inorganic Chemistry*, vol. 44, pp. 1728–1735, Mar. 2005.
- [24] P. Sinsersuksakul, R. Chakraborty, S. B. Kim, S. M. Heald, T. Buonassisi, and R. G. Gordon, "Antimony-Doped Tin(II) Sulfide Thin Films," *Chemistry of Materials*, vol. 24, pp. 4556–4562, Dec. 2012.
- [25] L. Baker, A. S. Cavanagh, D. Seghete, S. M. George, A. J. M. Mackus, W. M. M. Kessels, Z. Y. Liu, and F. T. Wagner, "Nucleation and growth of Pt atomic layer deposition on Al<sub>2</sub>O<sub>3</sub> substrates using (methylcyclopentadienyl)-trimethyl platinum and O<sub>2</sub> plasma," *Journal of Applied Physics*, vol. 109, p. 084333, Apr. 2011.
- [26] Q. Ma, F. Zaera, and R. G. Gordon, "Thermal chemistry of copper(I)-*N,N'*-di-*sec*-butylacetamidinate on Cu(110) single-crystal surfaces," *Journal of Vacuum Science & Technology A: Vacuum, Surfaces, and Films*, vol. 30, p. 01A114, Jan. 2012.
- [27] D.-w. Choi, M. Yoo, H. M. Lee, J. Park, H. Y. Kim, and J.-S. Park, "A Study on the Growth Behavior and Stability of Molecular Layer Deposited Alucone Films Using Diethylene Glycol and Trimethyl Aluminum Precursors, and the Enhancement of Diffusion Barrier Properties by Atomic Layer Deposited Al<sub>2</sub>O<sub>3</sub> Capping," *ACS Applied Materials & Interfaces*, vol. 8, pp. 12263–12271, May 2016.
- [28] J. Lee, B. Hong, R. Messier, and R. W. Collins, "Nucleation and bulk film growth kinetics of nanocrystalline diamond prepared by microwave plasma-enhanced chemical vapor deposition on silicon substrates," *Applied Physics Letters*, vol. 69, pp. 1716–1718, Sept. 1996.
- [29] E. Cano, C. L. Torres, and J. M. Bastidas, "An XPS study of copper corrosion originated by formic acid vapour at 40% and 80% relative humidity," *Materials and Corrosion*, p. 10, 2001.
- [30] M. W. Chase, *NIST-JANAF Thermochemical Tables Fourth Edition*. American Chemical Society and the American Institute of Physics for the National Institute of Standards and Technology, 1998.
- [31] M. J. Ferrante and R. R. Brown, "High temperature relative enthalpies of CuBr," *Report of Investigations 8917*, 1984.

- [32] F. Grønvold and E. F. Westrum, "Thermodynamics of copper sulfides I. Heat capacity and thermodynamic properties of copper(I) sulfide, Cu<sub>2</sub>S, from 5 to 950 K," *The Journal of Chemical Thermodynamics*, vol. 19, pp. 1183–1198, Nov. 1987.
- [33] M. J. Ferrante, J. Stuve, G. Daut, and L. Pankratz, "Low-temperature heat capacities and high-temperature enthalpies of cuprous and cupric sulfides," *Final Report of Investigations Bureau of Mines, Albany, OR. Albany Metallurgy Research Center*, 1978.
- [34] A. B. F. Martinson, S. C. Riha, E. Thimsen, J. W. Elam, and M. J. Pellin, "Structural, optical, and electronic stability of copper sulfide thin films grown by atomic layer deposition," *Energy & Environmental Science*, vol. 6, no. 6, p. 1868, 2013.
- [35] O. Madelung, U. Rössler, and M. Schulz, eds., *Non-Tetrahedrally Bonded Elements and Binary Compounds I*, vol. 41C of *Landolt-Börnstein - Group III Condensed Matter*. Berlin/Heidelberg: Springer-Verlag, 1998.
- [36] R. Heasley, *Vapor Deposition of Halide Perovskites and Hole-Transport Materials for Use in Thin-Film Photovoltaics*. PhD dissertation, Harvard University, Aug. 2017.
- [37] R. Heasley, L. M. Davis, D. Chua, C. M. Chang, and R. G. Gordon, "Vapor Deposition of Transparent, p-Type Cuprous Iodide Via a Two-Step Conversion Process," *ACS Applied Energy Materials*, vol. 1, pp. 6953–6963, Dec. 2018.

3



# Direct chemical vapor deposition of copper(I) bromide thin films

## 3.1 ABSTRACT

THE SEMICONDUCTORS  $\text{CuX}$  ( $X = \text{Br}, \text{I}$ ) are high-mobility p-type transparent conductors, promising for use in thin-film optoelectronic devices such as perovskite photovoltaics. These devices require smooth, pinhole-free films that are tens of nanometers thick, which cannot easily be deposited via existing methods. A promising alternative method, chemical vapor deposition (CVD), is an established industrial process with excellent uniformity. However, no prior CVD method could produce continuous thin films of any cuprous halide. We have established such a method, preparing  $\text{CuBr}$  thin films by reaction between  $\text{HBr}$  gas and vinyltrimethylsilane(hexafluoroacetylacetonato)copper(I). Our method not only provides the desired device-quality films, but also opens up the possibility of a general route to the CVD of other metal halides.

## 3.2 INTRODUCTION

Thin films of transparent conductive layers are important for a wide variety of optoelectronic devices, including photovoltaics, flat-panel displays, and other photonic devices requiring wide-bandgap semiconductors. N-type electron-transport layers (ETLs) tend to be more widely available, most notably transparent conducting oxides (TCOs).<sup>1</sup> In contrast, there are many fewer p-type transparent

hole-transport layers (HTLs) available, e.g. SnO,<sup>2</sup> NiO,<sup>3</sup> and alloy materials derived from Cu<sub>2</sub>O.<sup>4</sup> Unfortunately, p-type TCOs do not perform nearly as well as n-type TCOs for reasons that are under study and relate to the localized nature of the oxygen 2p-derived valence band.<sup>5</sup>

One promising alternative is the class of p-type semiconductors CuX (X = Cl, Br, I), which combine near-UV bandgaps<sup>6</sup> (2.9 to 3.1 eV), high hole mobility<sup>7,8</sup> (0.4 to 12 cm<sup>2</sup>V<sup>-1</sup>s<sup>-1</sup>), and transparency in the visible region. Because of these properties, CuX thin films are increasingly interesting as HTLs. For example, CuI has been used in p-n junctions,<sup>6</sup> thermoelectric devices,<sup>9</sup> and transparent conductors and hole transport layers in solar cells;<sup>10</sup> CuBr has been used in thin-film transistors.<sup>11</sup>

There are many solution or physical vapor deposition methods to fabricate CuX thin films, including doctor-blading,<sup>10</sup> spin-coating,<sup>12</sup> vacuum and thermal evaporation,<sup>6,13,14</sup> molecular beam epitaxy,<sup>15</sup> r.f. sputtering,<sup>16,17</sup> laser-assisted molecular beam deposition,<sup>18</sup> pulsed laser deposition,<sup>19</sup> and solid or vapor iodination<sup>8,20</sup> of Cu metal or Cu<sub>3</sub>N. Though these methods have enabled promising CuX thin films for research purposes, they typically produce films that have inadequate smoothness, purity, or continuity for ultimately commercial application in optical devices. Moreover, even high-quality, continuous CuI films made by sputtering dewet into islands if sputtered at high substrate temperatures.<sup>21</sup>

The lack of adequate fabrication methods for CuX motivates their potential fabrication via chemical vapor deposition (CVD). CVD is one of the main techniques used in industry to fabricate device-quality films of other materials, because of its molecular-level control of the fabrication process. However, research efforts in the development of a CVD process to deposit continuous metal halide films – not just CuX, but the larger class of materials MX<sub>n</sub> – have met several reactivity challenges. The few known metal halide CVD and ALD processes to produce MX<sub>n</sub> thin films have been confined almost entirely to metal fluorides. Known processes utilize either of two halide sources: HF and ancillary metal halides. The HF-based mechanism relies on adsorption generating the bifluoride anion (FHF<sup>-</sup>),<sup>22</sup> which is not sufficiently stable for the heavier halides, limiting the

utility of those methods. When ancillary metal halides are used as the halide source,<sup>23,24,25</sup> this chemistry relies on halide transfer between two metals, which is specific to the two metals in question and thus also limited in applicability. Accordingly, it is of considerable interest to develop a more general route to metal halide vapor deposition, and the past few years have seen increased research efforts toward this important goal. Some researchers have succeeded in producing discontinuous “islands” of metal halides (e.g. CuCl, CuI), but continuous thin films of metal chlorides, bromides, and iodides have remained elusive. For example, Grundmann and co-workers<sup>20</sup> reported CVD of CuI from reaction between cyclopentadienyl(triethylphosphino)copper(I) and ethyl iodide, resulting in well-crystallized islands of CuI instead of thin films. Cameron and co-workers reported ALD from the reaction between (bis(trimethylsilyl) acetylene)(hexafluoroacetylacetonato)-copper(I) and HCl or pyridine hydrochloride, resulting in CuCl crystallite islands instead of thin films.<sup>26,27,28</sup> We have attempted<sup>29</sup> both atomic layer deposition (ALD) and pulsed CVD of CuBr from HBr vapor and the volatile compound bis(*N,N'*-di-*sec*-butylacetamidinato)dicopper(I), [Cu(*s*BuAMD)]<sub>2</sub>, and found that both variants face mechanistic challenges. Under ALD conditions, HBr did not strongly adsorb to the substrate in its half of the ALD cycle, as evidenced by a lack of thin film deposition under a variety of conditions. However, under pulsed CVD conditions in which both precursor vapors were available in the reactor simultaneously, although the desired reaction to produce CuBr thin films succeeded, a further acid-base reaction between HBr and the acetamidine yielded nonvolatile acetamidinium halide salts, contaminating the CuBr films with carbon and nitrogen. To the best of our knowledge, continuous thin films of metal halides (X = Cl, Br, I) have not yet been attained by chemical vapor deposition.

In response to this challenge, we herein report the first chemical vapor deposition of a continuous metal halide (non-fluoride) thin film not relying on an ancillary metal halide as the halide source. Our method uses a reaction between the commercially available vinyltrimethylsilane(hexafluoroacetylacetonato)copper(I), Cu(hfac)(vtms), and HBr. Given the broad availability of metal  $\beta$ -diketonates,

this reaction paves the way for other CVD reactions to produce pure, continuous films of  $\text{MX}_n$  ( $X = \text{Cl, Br, I}$ ).

### 3.3 MATERIALS AND METHODS

#### 3.3.1 DIAGRAM OF THE REACTOR SETUP

Our custom-built apparatus for CVD reactions is a hot-walled ALD reactor was modified as shown in Figure 3.1, whose symbol legend is shown in 3.2. Our p-CVD depositions take place within a tube furnace that is 16'' long, where at the far left, reactants are introduced to the chamber. The substrate holder end is 0.5'' away from the inlet to the chamber, and the holder is 11.5'' long. Thus, samples can be placed between 0.5'' and 12'' away from the inlet. To have the highest precursor utilization, we placed substrates at the furthest left position, approximately 0.5'' away from where gases enter the chamber, unless otherwise noted.

When we place a silicon wafer substrate inside the tube furnace and heat the furnace until the temperature display stabilizes, we wondered what the temperature of the substrate is. We suspected that it might not be the same value displayed on the tube furnace, for a variety of reasons. First, the furnace thermocouple may be out of calibration. Second, the temperature of the tube and the coils may differ, since the metal tube is heated radiatively and convectively, rather than by direct contact with the heating coils. Third, the top surface of the silicon is exposed to a low pressure of gas. If allowed sufficient time, this gas must reach thermal equilibrium with the walls. But during a CVD recipe, new gas aliquots are pulsed in on the order of 0.1 to 10 seconds. These gases are at lower temperatures than the tube furnace initially, so they may cause instantaneous cooling. These three reasons prompted us to design experiments to determine the temperature of the substrates in our tube furnace.

We designed an *in situ* thermocouple and placed it where a substrate sits in the reactor, as shown

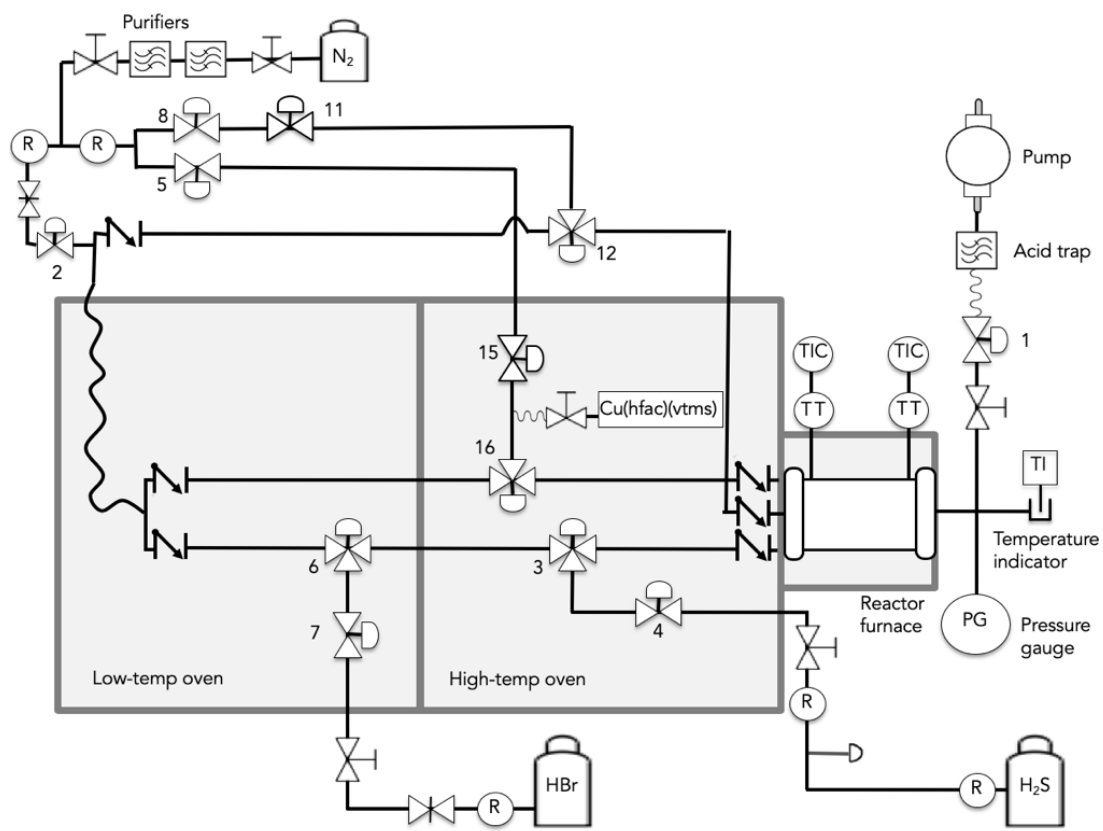


**Figure 3.1:** Piping & instrumentation diagram (P&ID) of the custom-built hot-walled reactor for CuBr depositions. Industry standard P&ID symbols are used: TT = temperature transmitter; TC = temperature controller; TI = temperature indicator. Other symbols shown in 3.2

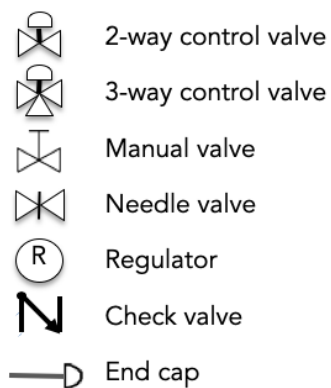


Figure 3.2: Piping & Instrumentation Diagram Legend.

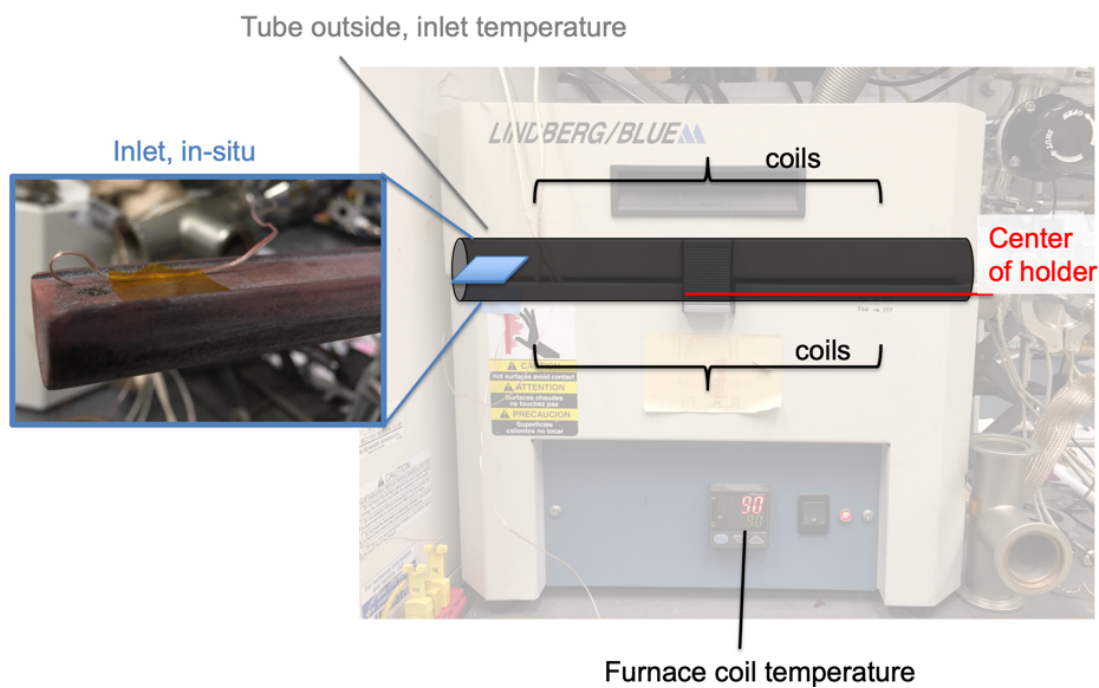


Figure 3.3: Our reactor tube furnace has four temperature readings. (1) The furnace heating coil temperature reading is displayed on the front (red LED number, black label). (2) Our substrate holder contains a thermocouple at its center (red). Additionally, we used Kapton tape to attach two thermocouples to other locations around the reactor. (3) We attached one directly to the outside of the tube at the far left of the furnace (gray). (4) We attached one to the substrate holder, bending the thermocouple end so that it touches the holder surface, where our substrates sit (blue, inset).

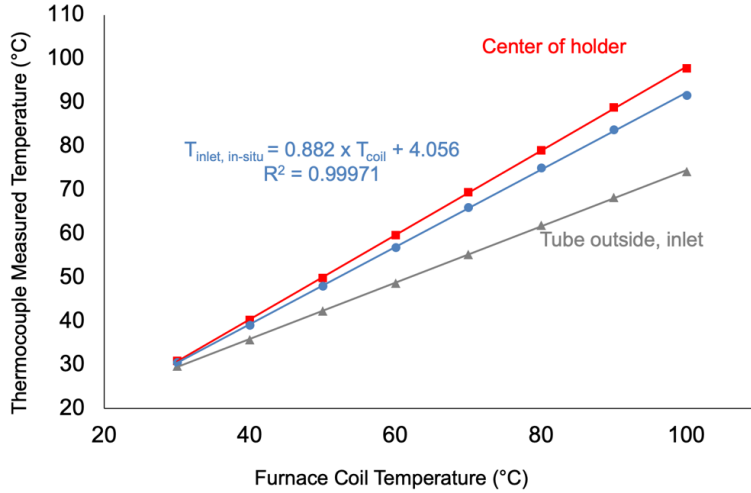


Figure 3.4: Calibration curve for measured temperatures

in Figure 3.3. We then allowed the reactor tube furnace to equilibrate at various set temperatures and recorded the output temperature readings from the four reactor thermocouples, resulting in the calibration curve shown in Figure 3.4. The inlet *in situ* temperature is closest to what we believe the substrate temperature is. Accordingly, when we conducted experiments in the present work, we recorded the furnace coil temperature for each experiment and then based on the calibration equation given in Figure 3.4, we reported the inlet *in situ* temperature. For example, when the tube furnace was set to 90 °C, the inlet *in situ* temperature was 83.4 °C.

We suspected that the pulses of gases into the reactor might slightly cool the substrate. To assess this possibility, we ran a recipe similar to our standard p-CVD recipe with the *in situ* thermocouple inside the reactor instead of a substrate. We closed the Cu(hfac)(vtms) bubbler manual valve, so as not to waste this chemical. We did not pulse in HBr, but instead pulsed N<sub>2</sub> with the same time sequence. The resulting inlet *in situ* temperature recorded during the cycle was highly repeatable and is shown in Figure 3.5. During one p-CVD cycle, the *in situ* temperature is decreased ~0.5 °C by the nitrogen purge and evacuation steps.

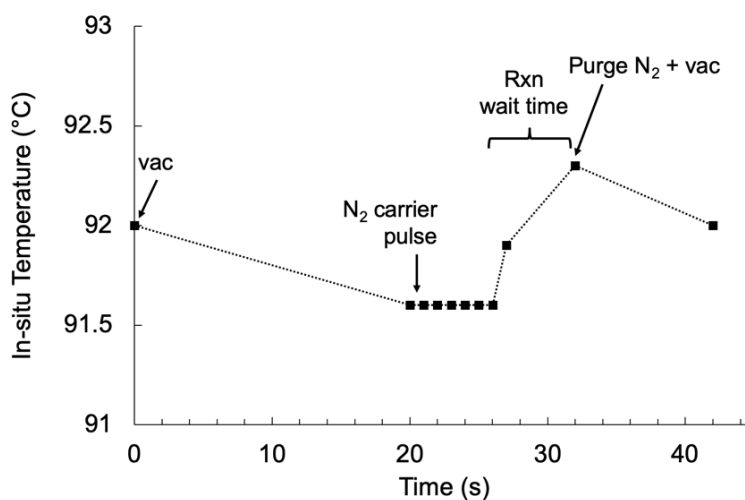


Figure 3.5: *In situ* temperature measured during the course of a nitrogen pulse sequence.

### 3.3.2 PURIFICATION OF $\text{Cu}(\text{hfac})(\text{vtms})$

The  $\text{Cu}(\text{hfac})(\text{vtms})$  compound was received as a liquid mixture of  $\text{Cu}(\text{hfac})_2$  and  $\text{Cu}(\text{hfac})(\text{vtms})$ . We developed the following procedure to separate the two compounds: in a nitrogen glovebox, the as-received  $\text{Cu}(\text{hfac})(\text{vtms})/\text{Cu}(\text{hfac})_2$  mixture was run through a silica column with pentane as the eluent. We observed a dark green top band and a bright yellow bottom band. The yellow pentane/ $\text{Cu}(\text{hfac})(\text{vtms})$  solution was collected in a Straus flask, which we stoppered and removed from the glovebox. Finally, we submerged the pentane/ $\text{Cu}(\text{hfac})(\text{vtms})$  in a 0 °C ice bath and distilled off the pentane by evacuating the flask and collecting pentane in a liquid nitrogen cold trap on a Schlenk line, as shown in Figure 3.6.

To quantify the proportion of pentane remaining in the solution, we dissolved an aliquot of the solution into deuterobenzene in an NMR tube and maintained a positive pressure of  $\text{N}_2$  gas in the headspace of the tube throughout the transfer to avoid oxidation of the  $\text{Cu}(\text{I})$  complex, and immediately collected a  $^1\text{H}$  NMR spectrum, shown in Figure 3.7. Peak assignments and integrals



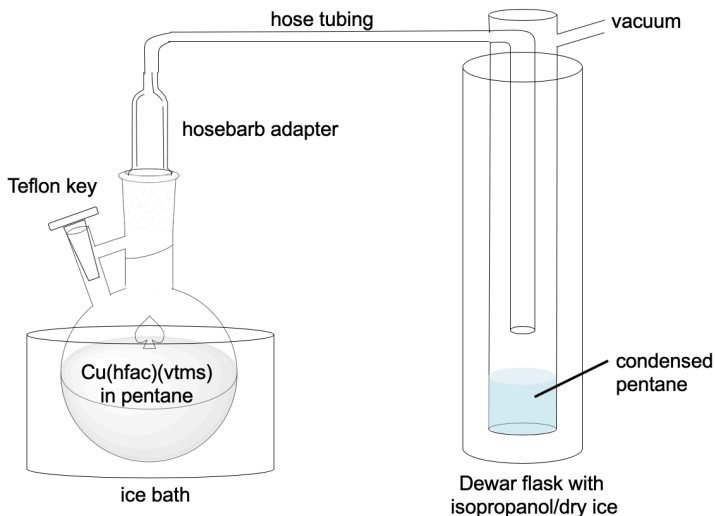


**Figure 3.6:** Straus flask diagram

for pentane, Cu(hfac)(vtms) protons, and deuterobenzene solvent residuals are given in Table 3.8 and are consistent with the literature. To estimate the amount of pentane in the solution, we first determined the relative proportions of the molecules implied by the proton integrations. Using the CH<sub>2</sub> protons, we calculate a relative molar amount of pentane (vs. the 0.5% residual C<sub>6</sub>H<sub>6</sub> in the C<sub>6</sub>D<sub>6</sub>) at 0.0067, which is larger than the calculation from the CH<sub>3</sub> protons, at 0.0033. We similarly calculated the relative molar amount of Cu(hfac)(vtms) using the three types of protons present on this molecule, as shown in Table 3.8. We next calculated the most conservative estimate of the amount of pentane in the solution, by using the largest amount of pentane calculated (0.0067) and the smallest amount of Cu(hfac)(vtms) calculated (0.71).

Our estimate is that the maximum amount of pentane in solution is  $0.0067 / (0.0067 + 0.71) = 0.9$  mol % pentane. This 99% Cu(hfac)(vtms) mixture was used directly as the precursor for CuBr vapor deposition. Purification can be done on large batches, and the purified precursor stored at -20 °C in a freezer does not disproportionate appreciably over at least 8 months. 5-mL aliquots were

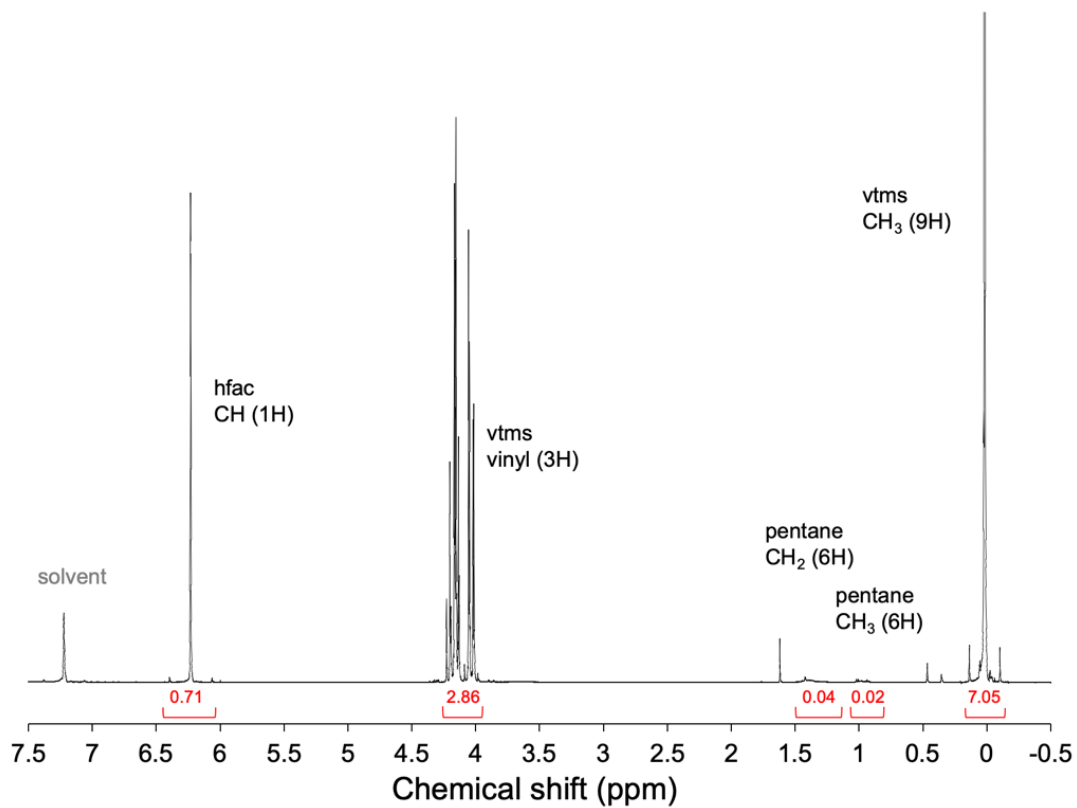


Figure 3.7:  $^1\text{H}$  NMR spectrum of  $\text{Cu}(\text{hfac})(\text{vtms})$  after purification procedure.

Compound	Identity	Mult.	Chemical Shift	Integral	# molecules (AU)
$\text{C}_6\text{D}_6$ solvent	CH	s	7.16 (ref'd)	n/a	n/a
n-pentane	$\text{CH}_3$ (6H)	t, 7	0.87	0.02	0.0033 pentanes
	$\text{CH}_2$ (6H)	m	1.32	0.04	0.0067 pentanes
vtms	$\text{SiCH}_3$ (9H)	s	-0.05	7.05	0.78 $\text{Cu}(\text{hfac})(\text{vtms})$
	vinyl (3H)	m	3.9-4.2	2.86	0.95 $\text{Cu}(\text{hfac})(\text{vtms})$
hfac	CH	s	6.17	0.71	0.71 $\text{Cu}(\text{hfac})(\text{vtms})$

Figure 3.8:  $^1\text{H}$  NMR peaks of  $\text{Cu}(\text{hfac})(\text{vtms})$  after purification procedure.

taken out and loaded into the reactor as needed for thin film deposition experiments.

### 3.3.3 CVD GROWTH OF CuBr AND Cu

Thin films of CuBr were deposited via pulsed-CVD using exposures to Cu(hfac)(vtms) (Gelest, purified as discussed above) and HBr (Matheson). Cu(hfac)(vtms) was loaded into a vacuum bubbler under a nitrogen atmosphere to prevent decomposition in air. HBr was used as received either at research purity (99.999%) or at chemical purity grade (99.8%), in a 1-lb lecture bottle pressurized to 320 psig. Owing to the materials used in the construction of the valves, these lecture bottles should not be stored for more than circa 6 months, as the valves tend to corrode due to HBr exposure.

The Cu(hfac)(vtms) vapor was transferred to the reactor chamber by a purified (Entegris purifier model number CE500KFI4R) nitrogen carrier gas held at a pressure of 10 Torr in the bubbler. Swagelok ALD valves operated by LABVIEW executed the pulsed-CVD recipes. Pulsed-CVD is similar to ALD, but omits the purging step between precursor doses. We programmed recipes with either of two types of precursor delivery, known in the literature as “open-valve mode” and “closed-valve mode” In open-valve mode, the reactor chamber is constantly being purged with a carrier gas that is being evacuated, such that the valve to the vacuum is never closed. In closed-valve mode, the reactor chamber is closed off from the vacuum at some point in the CVD cycle, often so that the precursors are held in the reactor chamber for a longer incubation time than would otherwise be possible if the valve to the vacuum were open. While closed-valve mode may in some instances provide higher precursor utilization and/or greater film coverage and uniformity throughout the reactor, it is also often slower, because it requires separate steps for reaction and for purging/evacuation. We explored both modes.

For closed-valve mode, the timing sequence used for the CuBr recipe may be expressed as  $t_1 - t_2 - t_3 - t_4 - t_5$ , where  $t_1$  is the exposure time of the Cu(hfac)(vtms),  $t_2$  is the exposure time of the HBr,  $t_3$  is a waiting period during which all valves are closed and deposition occurs,  $t_4$  is the time during

which nitrogen purge gas is purged through the reactor, and  $t_5$  is the chamber evacuation time, with all times given in seconds. For our standard recipe, the timing sequence was 1-1-5-10-20. The relevant pressures are: 0.7 Torr purge nitrogen pressure; 10 Torr nitrogen carrier gas pressure, 1 Torr HBr exposure and 1 Torr combined Cu(hfac)(vtms) and carrier gas exposure.

We assessed the partial pressures of Cu(hfac)(vtms) and carrier gas in the mixture by conducting a control experiment. The bubbler oven temperature was maintained at 35 °C, and the tube furnace was at room temperature. We first evacuated the precursor bubbler until the pressure stabilized at a steady state with pumping at a reactor pressure gauge reading of 40 mTorr. This pressure stabilization process took 90 seconds. Then, we closed the ALD valve to the bubbler and let its headspace gas equilibrate for 2 minutes, while the chamber continued to be under dynamic vacuum.

The reactor pressure gauge reading returned to 20 mTorr under dynamic vacuum, its typical base pressure. Then we closed the pump and opened the ALD valve to the bubbler for 1 second. We saw the pressure in the reactor tube furnace rise from 20 mTorr to 83 mTorr. We therefore reason that the partial pressure of Cu(hfac)(vtms) during our reaction cycles is approximately 63 mTorr.

In the standard recipe, the two precursors are in the reactor together for 5 seconds, resulting in an exposure value of 1 Torr  $\times$  5 seconds = 5 Torr-seconds each. Based on the preceding information, the exposure of Cu(hfac)(vtms) itself must be roughly 6% of 5 Torr-seconds, which is 0.3 Torr-seconds. We found during the course of our experiments that the full 5 seconds are not necessary to achieve our reported growth per cycle. The 5-second wait time  $t_3$  can be reduced to 0.1 second, without reducing the film growth per cycle. Thus, our “accelerated” closed-valve p-CVD recipe timing sequence is 1-1-0.1-10-20.

In open-valve mode, a nitrogen stream is constantly purging the reactor chamber and precursor manifold central lines, so both the valves to nitrogen and to the pump downstream of the reactor chamber are always open. The timing sequence used for an open-valve CuBr recipe may be expressed as  $t_a - t_b - t_c$ , where  $t_a$  is the exposure time of the Cu(hfac)(vtms),  $t_b$  is the exposure time

of the HBr, and  $t_c$  is the wait time during which solely the nitrogen and pump valves are open. This wait time is required in order to return the reactor pressure down to its steady-state nitrogen flow, after HBr and Cu(hfac)(vtms)/carrier gas are dosed in. Our open-valve recipe timing sequence is 0.5-0.5-8. The relevant pressures are, as for the closed-valve mode, 0.7 Torr purge nitrogen pressure, 10 Torr nitrogen carrier gas pressure, 1 Torr HBr and 1 Torr Cu(hfac)(vtms) carrier gas pressure.

The control experiments to deposit Cu metal were conducted in closed-valve mode. The timing sequence used for the Cu recipe is the same as our standard closed-valve recipe, namely a timing sequence of 1-1-5-10-20, except that instead of a dose of HBr during the  $t_2$  time, no valves open during that time and thus HBr is not injected into the reactor.

#### 3.3.4 SUBSTRATES

Films were deposited on 5 substrate types. Three substrate types were purchased: 12.7 mm diameter high purity vitreous carbon planchets (Ted Pella), 1 cm  $\times$  1 cm quartz substrates (Electron Microscopy Sciences), and 1 in.  $\times$  1 in. Si substrates with a 300-nm surface layer of SiO<sub>2</sub> grown by wet oxidation, which were cut from larger wafers (University Wafer). We prepared two more substrate types in-house, by adding surface layers to both the quartz and the SiO<sub>2</sub>/Si substrates. One surface layer we prepared using a Denton E-beam evaporator: 5 nm of Ti adhesion layer were followed by 200 nm of Pt. Another surface layer we prepared using an STS PECVD: 40 nm of SiN<sub>x</sub> were deposited from 35 sccm SiH<sub>4</sub>, 55 sccm NH<sub>3</sub>, and 1960 sccm N<sub>2</sub> on high-frequency mode (13.56 MHz), with the power supply at 20 W. The vitreous carbon planchets were used as received, without washing prior to CuBr deposition. All of the other 4 substrate types were treated with solvent washes of semiconductor-grade acetone and isopropanol (BDH,  $\geq$  99%). Furthermore, both the Pt and the SiO<sub>2</sub>/Si substrates were then treated with UV-ozone for 5 min both to promote the formation of surface hydroxyl groups and, via oxidation, further remove any carbonaceous contamination on the surface.

### 3.3.5 FILM CHARACTERIZATION

Scanning electron microscopy (SEM) was performed in a Zeiss Ultra Plus scanning electron microscope. X-ray photoelectron spectroscopy (XPS) was performed on a Thermo Scientific K-Alpha spectrometer equipped with a monochromated Al  $K\alpha$  X-ray source, 12 kV electron beam, and Ar<sup>+</sup> sputtering gun. Depth profiles were collected by sputtering at 500 eV for 80 s per level, unless otherwise stated. The XPS sputtering rate was determined by dividing the film thickness as determined by SEM by the total sputtering time before the substrate elemental signals were detected. X-ray diffraction (XRD) patterns were recorded in a Bruker D2 PHASER X-ray diffractometer using Cu  $K\alpha$  radiation ( $\lambda = 1.542 \text{ \AA}$ ) and a  $\vartheta - 2\vartheta$  scan. Optical transmittance and reflectance measurements were performed over a wavelength range of 200 - 800 nm using the small spot kit in the diffuse reflectance accessory of an Agilent Cary 7000 Universal Measurement Spectrophotometer. Reflectance measurements were made at  $60^\circ$  and transmittance measurements at  $180^\circ$ . To determine the absorption coefficient of CuBr thin films, we measured transmittance and reflectance for both a 40 nm SiN<sub>x</sub> film on quartz (the “substrate” measurement), and a 120 nm CuBr film on 40 nm SiN<sub>x</sub> on quartz (the “total” measurement). To extract out the CuBr film absorption coefficient, we used two data treatment steps. First, we calculated  $\alpha_{sub}$  and  $\alpha_{total}$  via the equation  $\alpha = 1/d_{sub} \times \ln\left(\frac{1-R}{T}\right)$ , where  $d_{sub}$  = thickness of quartz substrate (1 mm), following the approximation by Ritter and Weiser.<sup>30</sup> Second, we estimated  $\alpha_{CuBr}$  via the equation  $\alpha_{film} = d_{sub}/d_{film} \times (\alpha_{total} - \alpha_{sub})$ , following Cesaria.<sup>31</sup>

Electrical properties were assessed by Hall effect measurements using a high sensitivity rotating parallel dipole line system developed by IBM.<sup>32</sup> To form electrical contacts for Hall measurements, a 10 nm adhesion layer of Ti followed by 200 nm of Au were deposited through a shadow mask by electron-beam evaporation in a Denton Explorer. The leads of the Hall system were adhered to the Au contacts using In solder. Rutherford Backscattering Spectrometry (RBS) experiments and

data interpretation were conducted at the Rutgers Ion Scattering Facility by Dr. Ryan Thorpe. A 2.0 MeV beam of  $^4\text{He}^{++}$  ions was used for RBS experiments, with an energy resolution of 20 keV. Contact angle measurements were performed via the sessile drop technique using the half angle method on a Tantec CAM-PLUS MICRO equipped with micrometer syringe and fiber-optic light source. Four standard contact angle test liquids (diiodomethane, thiodiglycol, ethylene glycol, and deionized water) were selected for their distinct and well-defined dispersive and polar components of surface free energy.

### 3.4 RESULTS AND DISCUSSION

#### 3.4.1 SCREEN OF SUBSTRATES

CuBr films were grown in a custom-built, hot-walled ALD reactor (see diagram in Figure 3.1) which has been reported in previous work.<sup>29</sup> In this reactor, we installed a bubbler containing the Cu(hfac)(vtms) precursor. Thin films of CuBr were deposited via pulsed-CVD using alternating exposures to Cu(hfac)(vtms) and HBr, with the recipes outlined in the Methods section.

The morphology of thin films grown by CVD is highly dependent on the surface free energy match between the deposited material and the surface material. Cuprous halides do not seem to easily wet metal oxides: we have observed<sup>29</sup> that vapor-converted CuBr forms islands on  $\text{SiO}_2$ , and that CuI forms islands<sup>33</sup> on  $\text{Cu}_2\text{O}$  under many experimental conditions. Prior researchers have observed similar results in attempts to produce CuI thin films via CVD. For example, Gottschalch et al. found<sup>20</sup> CuI formed islands when grown on  $\text{Al}_2\text{O}_3$ ,  $\text{SiO}_2$ , Si, and GaAs. Accordingly, we intended to assess our proposed CVD process on  $\text{SiO}_2$  (for comparison), as well as on alternative substrates that we hoped could allow formation of densely packed, continuous films instead of sparse islands. Based on availability, surface free energy considerations, and the substrate requirements of various analytical techniques we sought to employ, we selected glassy carbon, silicon nitride, and platinum

for initial tests.

When we ran our standard p-CVD recipe at a substrate temperature of  $83.4\text{ }^{\circ}\text{C} \pm 0.5\text{ }^{\circ}\text{C}$ , we observed apparent crystallites approximately 100 nm in diameter on each of 4 substrate surfaces: glassy carbon, silicon nitride, platinum, and silica (Figures 3.9, 3.10, and 3.11). These films were uniform across the  $1'' \times 1''$  substrates.

Consistent with our previous findings<sup>29</sup> from vapor-converted CuBr films, we found that CuBr grains on SiO<sub>2</sub> were somewhat isolated from each other, with SiO<sub>2</sub> substrate visible in the plan-view SEM micrographs. In contrast, the  $\sim 70\text{nm}$  thick CuBr films grown on glassy carbon, silicon nitride, and platinum appeared continuous at the  $83.4\text{ }^{\circ}\text{C} \pm 0.5\text{ }^{\circ}\text{C}$  substrate temperature.

During SEM imaging, we observed a beam-induced phenomenon when imaging the CuBr films grown on Pt substrates. We saw bright dots appear on the CuBr grains, and, with further beam exposure, these dots became larger and grew up like tendrils out of the grains. Because these tendrils were bright when imaged in the in-lens imaging mode, we envision that they may be copper metal, and that electrons from the SEM beam are reducing the film's Cu<sup>1+</sup> to Cu<sup>0</sup>. This effect only occurs when the underlying substrate was platinum, implying that conduction is required for this phenomenon to occur. In the SEM images of CuBr on Pt, images were recorded immediately upon navigating the beam to a new film area, so that this effect was minimized in our images of CuBr grains. Still, small bright dots are visible in Figure 3.9c, Figure 3.13c, and Figure 3.12.

### 3.4.2 FILM COMPOSITION CHARACTERIZATION

We next used two methods to evaluate the elemental composition of the deposited thin films. We first used X-ray photoelectron spectroscopy (XPS). We found that the composition of our film grown on silicon nitride was 55% Cu and 45% Br by XPS (Figure 3.13). Matrix effects alter the detection efficiency of photoelectrons, and there is no a priori reason to expect the uncalibrated XPS values to be quantitative.



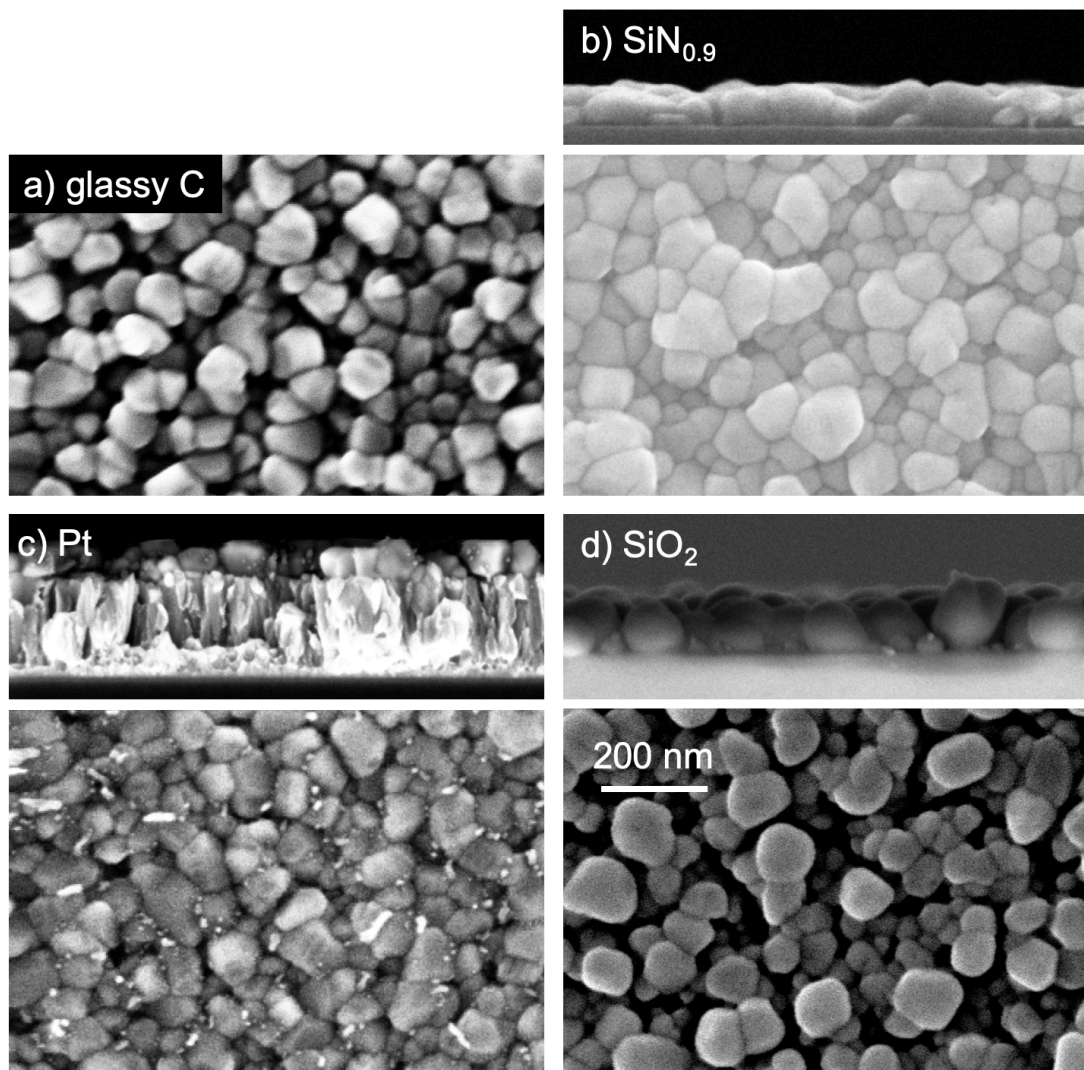


**Figure 3.9:** SEM images of CuBr grown at 83.4 °C on (a) glassy carbon, (b) silicon nitride, (c) platinum, and (d) silica. All films were deposited using 600 cycles of the standard p-CVD recipe. No cross-section is available for glassy carbon because the as-received plachets are too rough for imaging at these length scales and moreover they cannot be easily fractured, forming dust instead of cleaving cleanly.

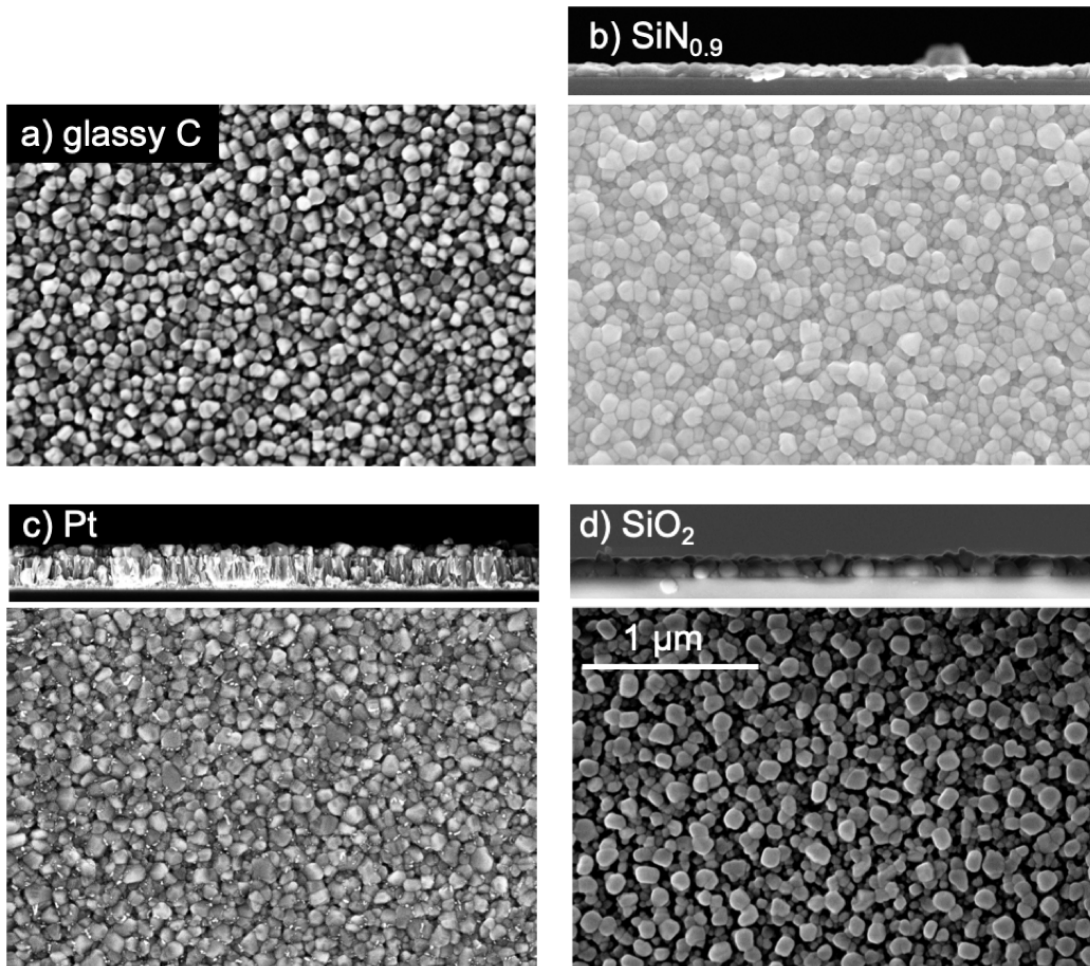


**Figure 3.10:** SEM images of CuBr grown at 83.4 °C on (a) glassy carbon, (b) silicon nitride, (c) platinum, and (d) silica. All films were deposited using 600 cycles of the standard p-CVD recipe. These micrographs show uniformity across 3 microns of film length. No cross-section is available for glassy carbon because the as-received planchets are too rough for imaging at these length scales.

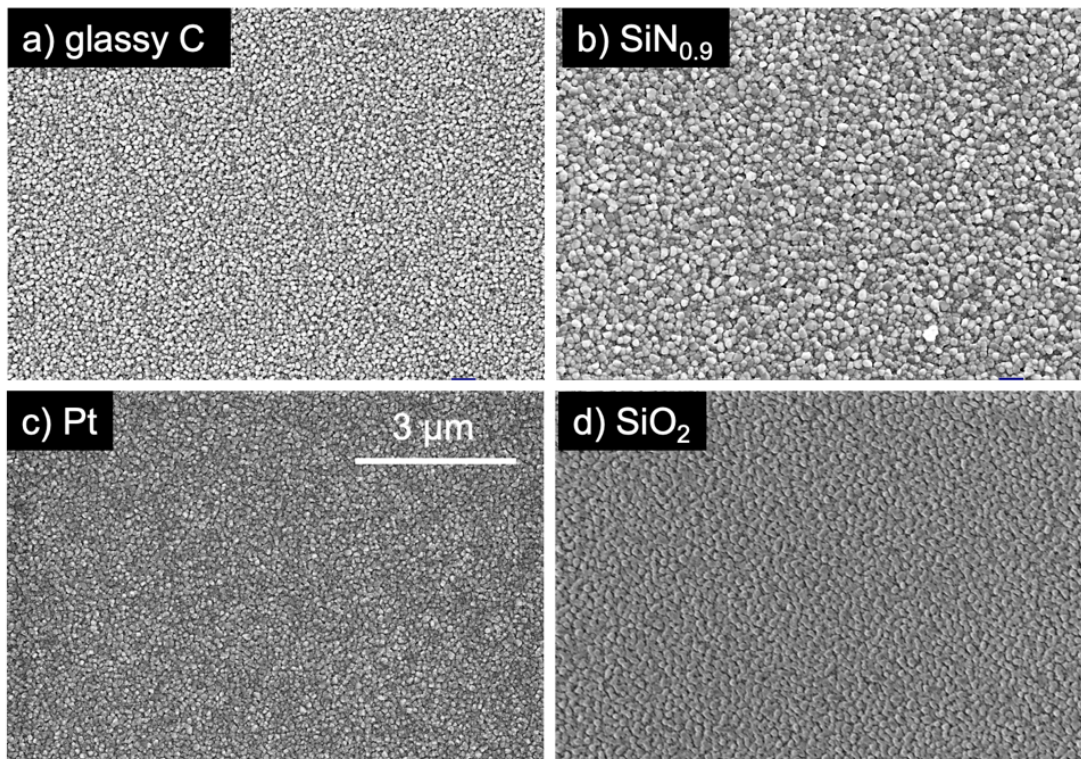


**Figure 3.11:** SEM images of CuBr grown at 83.4 °C on (a) glassy carbon, (b) silicon nitride, (c) platinum, and (d) silica. All films were deposited using 600 cycles of the standard p-CVD recipe. These micrographs show uniformity across 10 microns of film length.



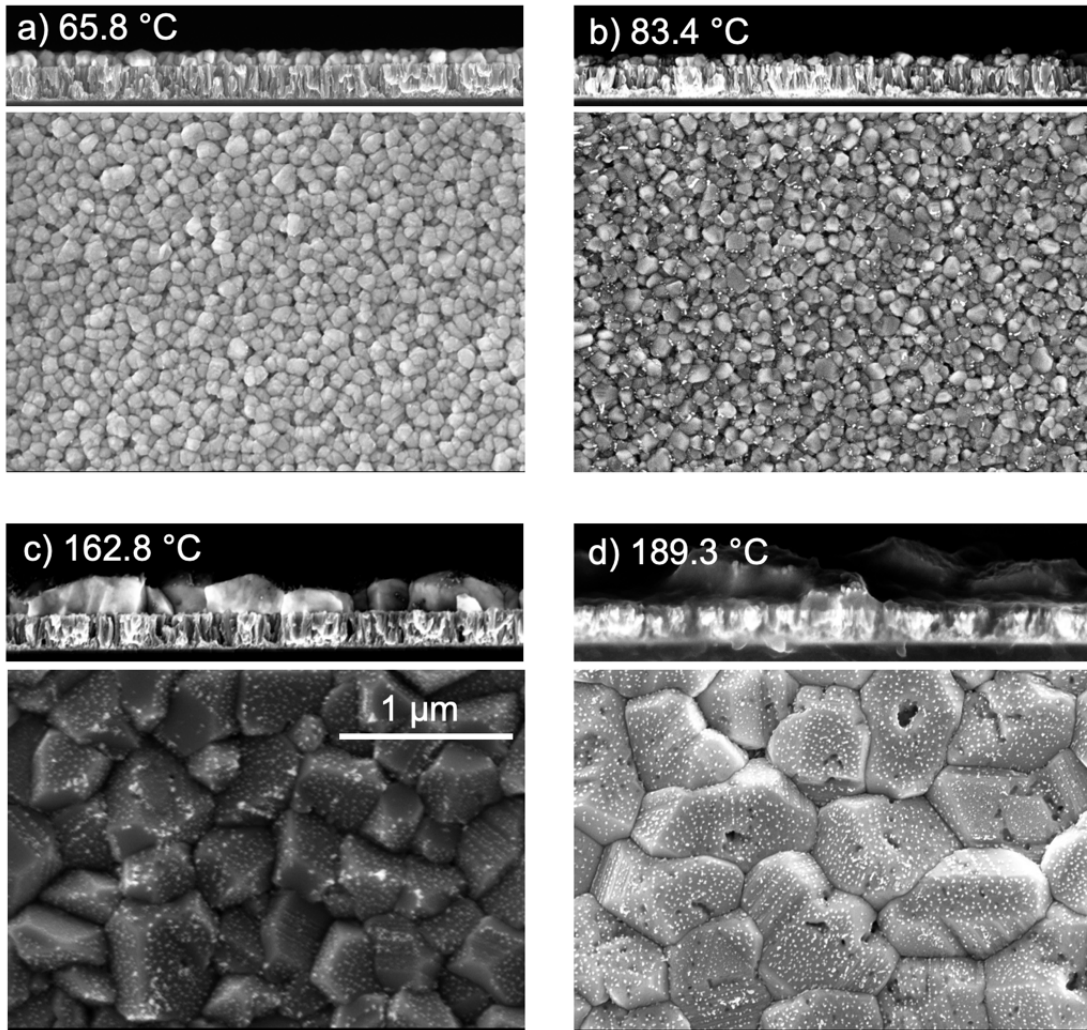


**Figure 3.12:** SEM images of CuBr deposited on Pt using our standard recipe at a range of temperatures: (a) 65.8 °C, (b) 83.4 °C, (c) 162.8 °C, and (d) 189.3 °C.

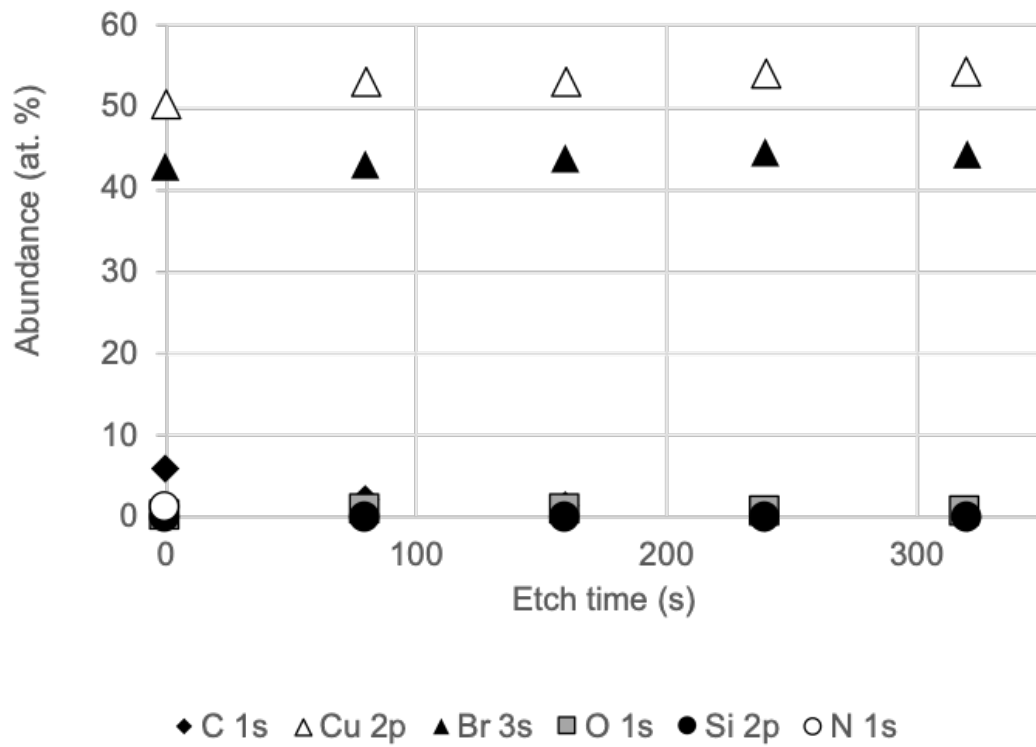


**Figure 3.13:** XPS depth profile of CuBr deposited on silicon nitride at 83.4 °C using the standard p-CVD recipe. After sputtering away surface contamination, we measured an elemental composition of 55 at. % Cu and 45 at. % Br.

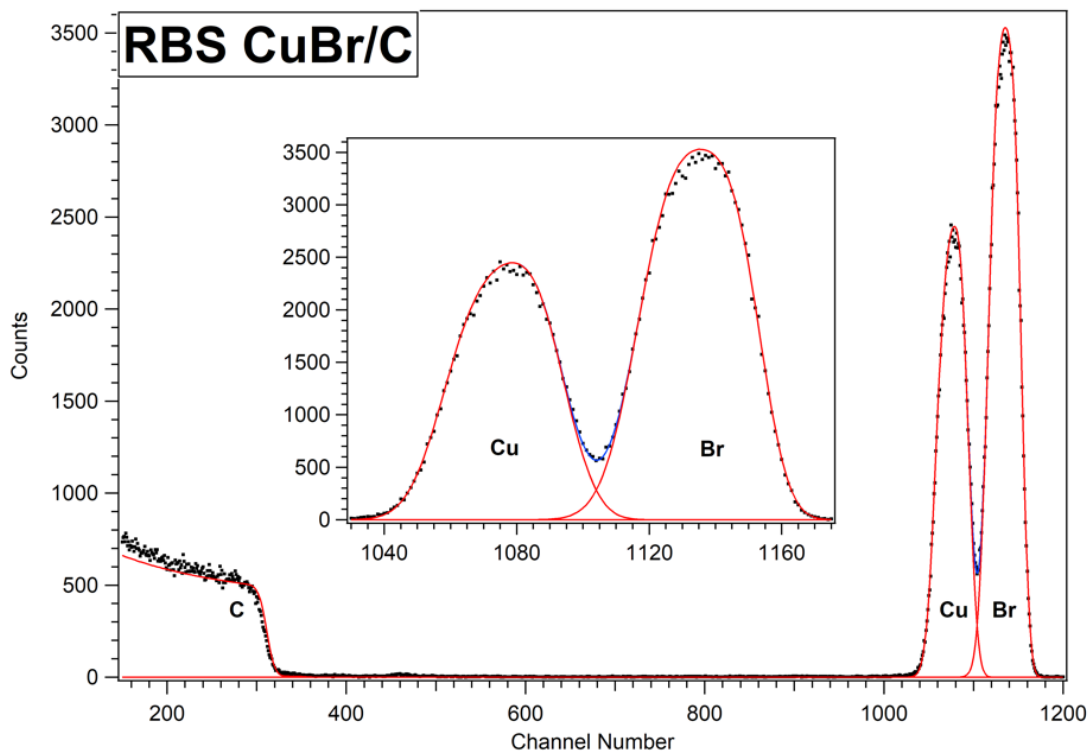


**Figure 3.14:** Fits of the Rutherford Backscattering Spectrometry data, provided by Dr. Ryan Thorpe. The model shown here indicates that identical counts of Cu and Br atoms were found in the film, giving a stoichiometry of  $\text{Cu}_{1.00}\text{Br}_{1.00\pm 0.02}$ . No other elements were detected. The peak shapes here are consistent with compositional uniformity throughout the depth of the CuBr film.

Given the difference from the expected 1:1 ratio and the possible role of these matrix effects, we calibrated the XPS composition with Rutherford backscattering spectrometry (RBS). RBS is typically used to detect, in a thin film, elements that are heavier than elements comprising the substrate. Thus, we subjected the film grown on glassy carbon to RBS analysis, allowing us to search for impurities of N, O, etc., to the at. 1% level. By RBS, we found that the density of Cu and Br were each  $184 \pm 3 \times 10^{15}$  atoms/cm<sup>2</sup>, giving a stoichiometry of  $\text{Cu}_{1.00}\text{Br}_{1.00\pm 0.02}$ . No other elements were detected by RBS. Further, the peak shapes of the RBS spectra indicate compositional uniformity throughout the CuBr film (Figure 3.14).

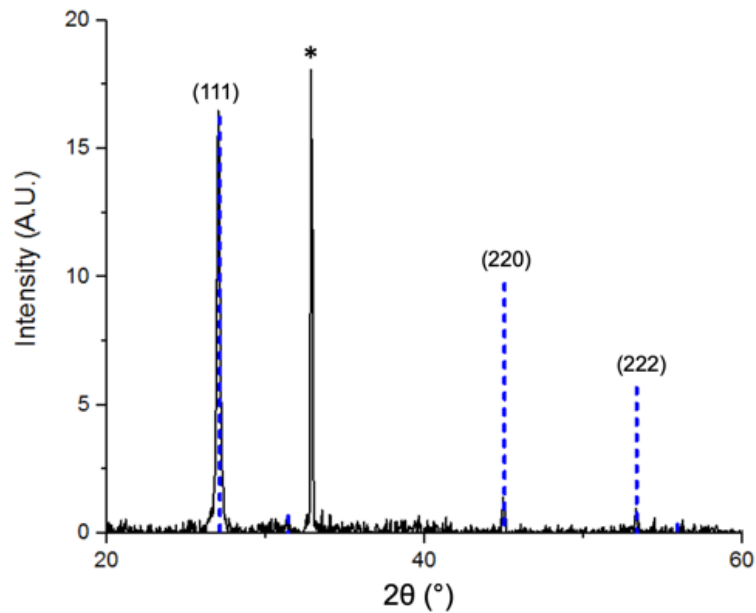


**Figure 3.15:** X-ray diffraction pattern of CuBr deposited on silicon nitride via 600 cycles of our standard p-CVD recipe. The blue dotted lines PDF 006-0292, for  $\gamma$ -CuBr, normalized such that the reference (111) peak height matches our CuBr data (111) peak height. The asterisk (\*) denotes a background peak associated with the XRD instrument itself.

We confirmed that our films are composed of CuBr via XRD. As shown in Figure 3.15, our CuBr films are crystal-line and highly oriented in the (111) direction. The experimental pattern matches PDF 006-0292 for  $\gamma$ -CuBr. Using the Debye-Scherrer equation, we calculated a value of 43 nm for  $\tau$ , the mean size of the ordered (crystalline) domains. This value of  $\tau$  is smaller than the apparent grain size by microscopy, which is between 50-200 nm for the same film.

### 3.4.3 SUBSTRATE TEMPERATURE STUDY

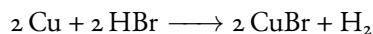
Based on our substrate screen, we chose to further study the deposition characteristics on silicon nitride and platinum substrates. We deposited CuBr using our standard recipe at a range of temperatures between 65 °C and 200 °C. Grown on both silicon nitride and platinum substrates, CuBr grains increased in size as a function of temperature, as shown on silicon nitride (Figures 3.16 and

3.17) and Figure 3.12 on platinum.

At the high end of the temperature range, at 136.4 °C, we observed both a dense layer of 50-100 nm CuBr grains and scattered  $\sim 1\text{-}\mu\text{m}$  CuBr particles. These particles appear to be large enough to scatter light, such that the film grown at 136.4 °C appears cloudy to the eye, as opposed to the transparent films grown at or below 83.4 °C  $\pm$  0.5 °C. The deposition of large particles at high deposition temperatures is not uncommon in CVD reactions. They often result from gas-phase reactions, which can produce solid particles or “powder” on the substrate. Because light-scattering films are not ideal for many transparent conductor applications, we did not explore this reaction at temperatures higher than 136.4 °C on the silicon nitride surface. We found an overall similar morphology-temperature relationship for CuBr grown on platinum, but we note the complication that on metal surfaces, the Cu(hfac)(vtms) precursor can disproportionate to form Cu and volatile Cu(hfac)<sub>2</sub>,<sup>34</sup> a process promoted by increasing temperature. Accordingly, we further study depositions on platinum in the next section.

#### 3.4.4 CONTROL EXPERIMENTS

We envisioned there may be at least two classes of mechanism by which CuBr is formed via reaction between Cu(hfac)(vtms) and HBr. In the first mechanism, HBr and Cu(hfac)(vtms) undergo an acid-base bimolecular reaction to form CuBr, Hhfac, and vtms. There are variations on this mechanism depending on when vtms is released and which species is/are bound to the surface. In the second mechanism, two Cu(hfac)(vtms) molecules undergo the known metal-catalyzed disproportionation to form a Cu metal film, and the volatile species Cu(hfac)<sub>2</sub> and 2 vtms. In this second mechanism, a film of copper metal results, and then HBr may oxidize the copper metal up to Cu<sup>II</sup>, resulting in CuBr and a reduced species, perhaps H<sub>2</sub> vapor, according to the reaction:





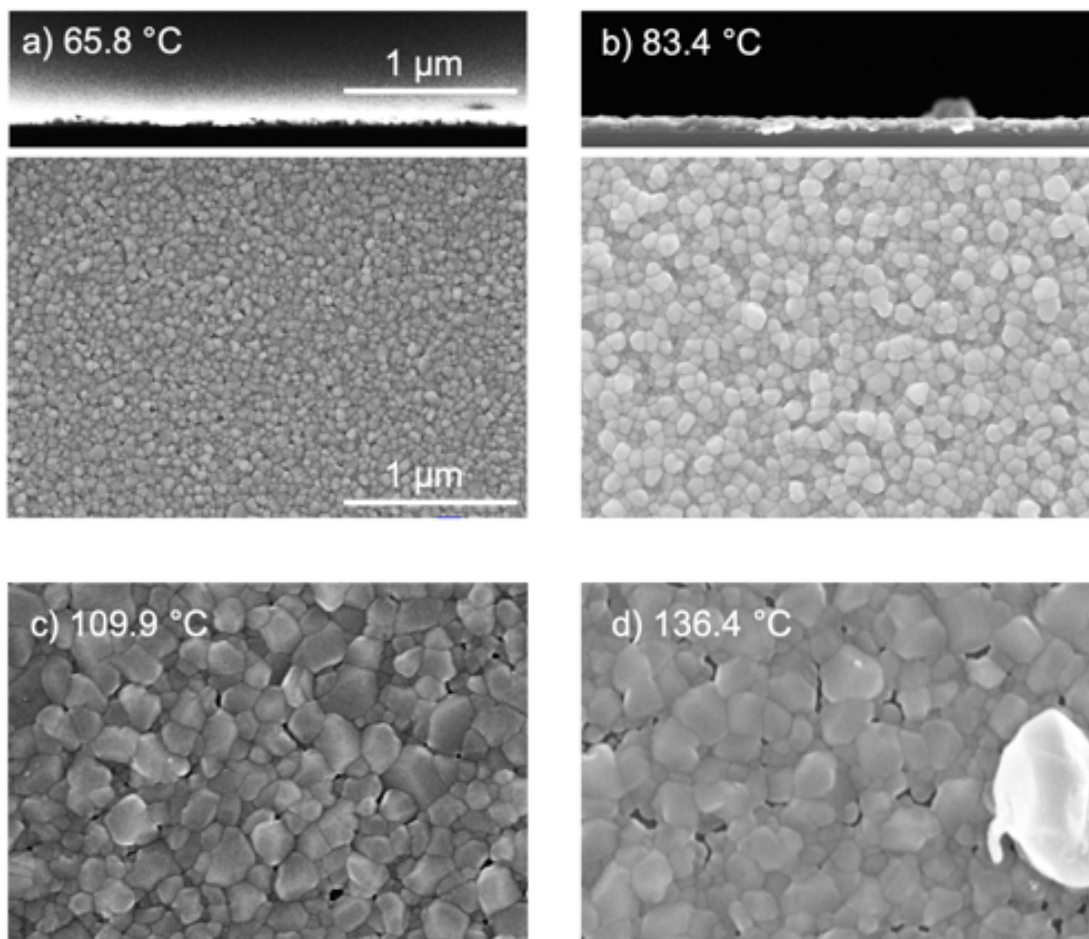


**Figure 3.16:** SEM images of CuBr grown on silicon nitride at a range of substrate temperatures: (a) 65.8 °C, (b) 83.4 °C, (c) 109.9 °C, and (d) 136.4 °C. All images at same scale. Scale bar 1 micron.

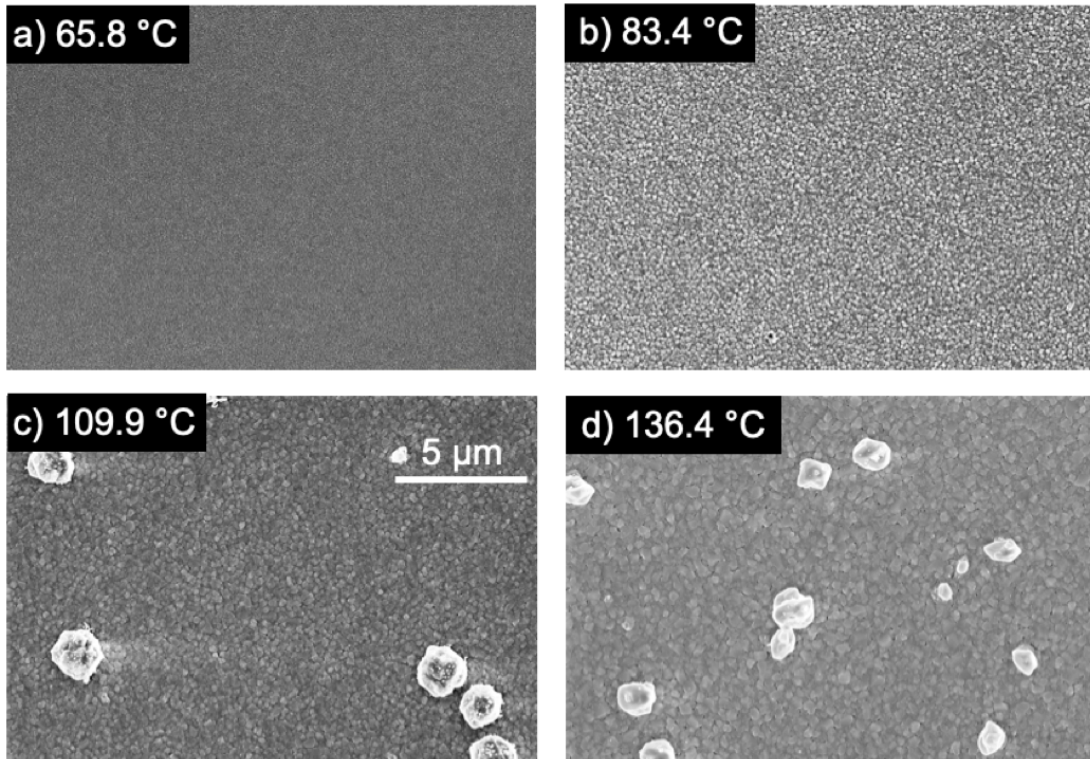


**Figure 3.17:** SEM images of CuBr grown on silicon nitride at a range of substrate temperatures: (a) 65.8 °C, (b) 83.4 °C, (c) 109.9 °C, and (d) 136.4 °C. Scale bar is 5 microns. At temperatures 109.9 °C and above, we observed large particles atop the film, whose areal density increases with deposition temperature.

We believed the first mechanism to be likely by analogy to the many metalorganic precursor reactions with vapors of Brønsted acids ( $\text{H}_2\text{O}$ ,  $\text{H}_2\text{S}$ , etc.). We next explored whether the second mechanism might be operational or whether we could rule it out. The second mechanism is possible on thermodynamic grounds. Reaction (1) has a  $\Delta G_{rxn}$  of  $-85.5$  kJ/mol at  $90$  °C.<sup>35</sup> However, we reasoned that the Cu metal may never form in the first place at the conditions of interest, due to the fact that the disproportionation of  $\text{Cu}(\text{hfac})(\text{vtms})$  has been reported to function only at temperatures above approximately  $100$  °C and that it is metal-surface-catalyzed.<sup>34,36</sup> This knowledge prompted us to conduct control experiments to determine whether metallic Cu may first be formed on the surface and then transformed into CuBr. In our control experiment, we dosed  $\text{Cu}(\text{hfac})(\text{vtms})$  into the reactor using the same sequence as the CuBr depositions, but without introducing HBr, at a substrate temperature of  $83.4$  °C. Five substrates were placed into the chamber: glassy carbon, silica, silicon nitride, alumina, and platinum.

Upon the four insulating substrates, we determined that hardly any deposition had occurred. Via the SEM images in Figure 3.18, we find no visible Cu grains. Via XPS in Figure 3.19, we find approximately  $0.5$  % of Cu or Br present (likely Br is left over in the chamber from HBr-based depositions). High-resolution XPS spectra were taken and corroborated with survey scans to ensure no peaks were missed.

However, upon the platinum substrate, we found a copper layer had been deposited (XPS and SEM in Figure 3.20). Based on these SEM images, we believe this layer is variable in thickness with distance into the reactor, from circa  $300$  nm to  $80$  nm, and even thinner further into the reactor. Therefore, we concluded that the mechanism of deposition upon insulating substrates is likely not bromination of existing copper metal, but that such a mechanism would be possible when the substrate is platinum.

It is known that  $\text{Cu}(\text{hfac})(\text{vtms})$  disproportionates to form nonvolatile Cu metal and volatile  $\text{Cu}(\text{hfac})_2$  over time and with heating. Because the  $\text{Cu}(\text{hfac})(\text{vtms})$  precursor is heated to  $35$  °C to

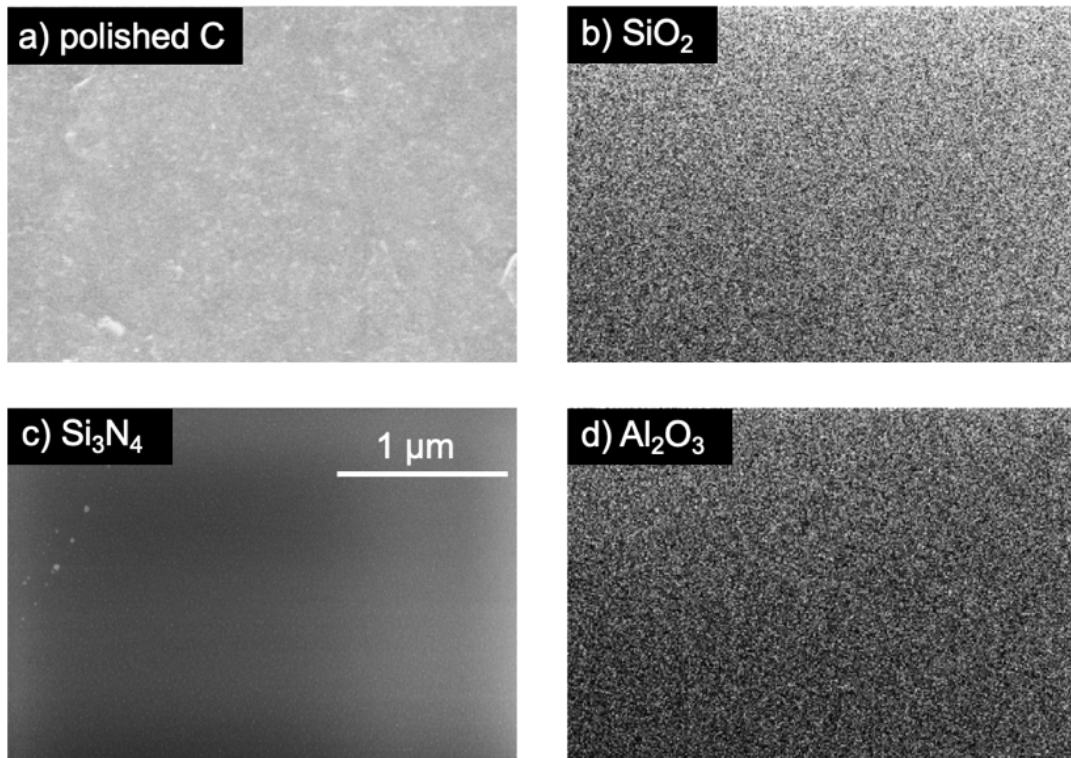


**Figure 3.18:** In a control experiment, Cu(hfac)(vtms) was dosed for 600 cycles onto insulating substrates at a substrate temperature of 83.4 °C. Scale bar is 1 micron for all four images: a) polished carbon, b) silicon dioxide, c) silicon nitride, and d) aluminum oxide substrates.

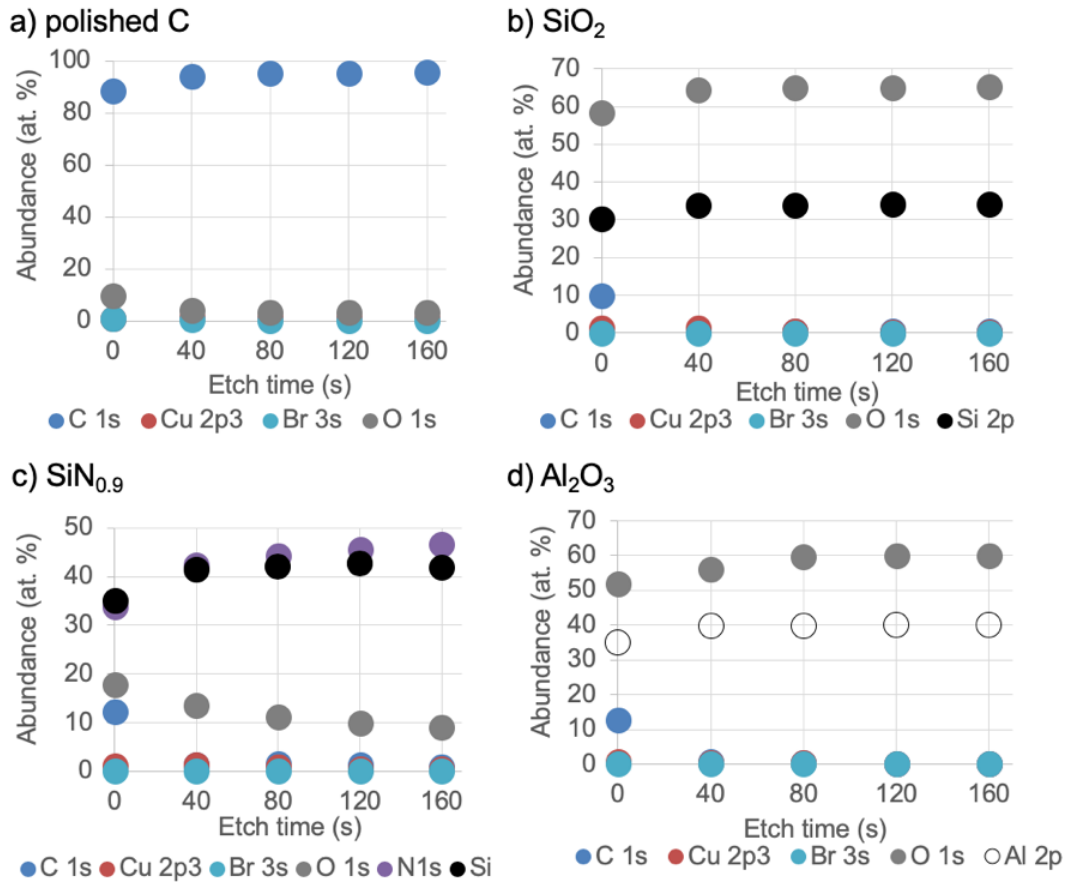


**Figure 3.19:** In a control experiment, Cu(hfac)(vtms) was dosed for 600 cycles onto insulating substrates at a substrate temperature of 83.4 °C. After surface carbon is sputtered away beyond the first etch level, the substrate is the most appreciably detected component, with approx. 0-0.5 at % of Cu and 0-0.5 at % Br detected.

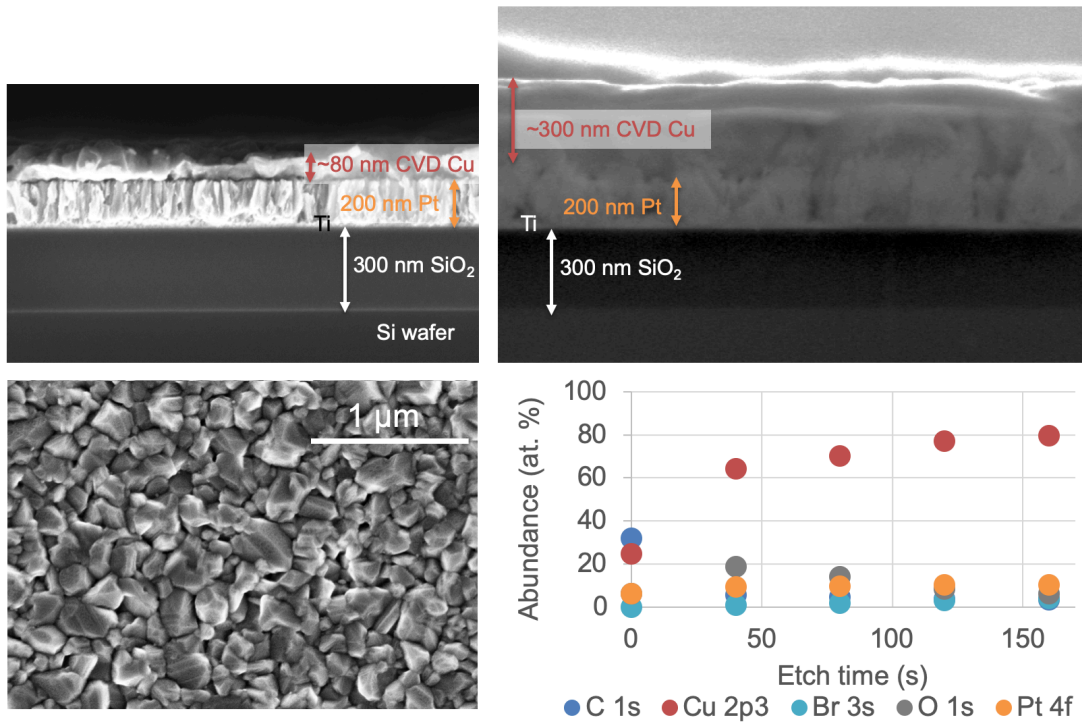


**Figure 3.20:** In a control experiment, Cu(hfac)(vtms) was dosed for 600 cycles onto a platinum substrate at a temperature of 83.4 °C. High-resolution XPS and SEM indicate that a copper layer of variable thickness has been deposited on the surface of the platinum. Via SEM, we imaged regions of the Cu film that were as thin as 80 nm and as thick as 300 nm.

enhance its evaporation during CVD reactions, we considered whether this disproportionation reaction might take place to an appreciable extent within the precursor container over the course of many deposition runs. However, we found no significant difference between films grown immediately after Cu(hfac)(vtms) was loaded and films grown after 5 months, the timescale of loading a new charge of this precursor.

#### 3.4.5 STUDY OF SUBSTRATE OXIDATION OVER TIME

Knowing that silicon nitride may oxidize over time, we anticipated that exposing the silicon nitride adhesion layer to ambient air may affect the nucleation of CuBr on silicon nitride. To understand the potential effects of ambient oxidation of silicon nitride on CuBr growth, we conducted an experiment in which we deposited CuBr on several substrates in the same deposition experiment, including both freshly-deposited SiN<sub>x</sub> substrates and older SiN<sub>x</sub> substrates that had been exposed to air for 4 months. On average, there was no appreciable difference between the CuBr films grown on these two substrate types.

#### 3.4.6 STUDY OF GROWTH PER CYCLE

We assessed the CuBr film growth per cycle on silicon nitride substrates at a substrate temperature of  $83.4 \text{ }^{\circ}\text{C} \pm 0.5 \text{ }^{\circ}\text{C}$  using two closed-valve p-CVD recipes. Our standard recipe has a 5-second reaction wait time where all valves are closed, whereas for our accelerated recipe, this period is only 0.1 seconds. These recipes have the same timings for all other pulses, as described in the Methods section. When using either recipe, if the Cu(hfac)(vtms) liquid volume in the bubbler was greater than about 6 mL, we obtained a growth per cycle of 0.12 nm CuBr/cycle for substrates placed at the reactor inlet.

Under these conditions for both recipes, we saw that more CuBr was deposited at the inlet than

at the outlet. We conducted an experiment to qualitatively assess precursor utilization throughout the reactor tube. As described in the Methods section, substrates can be placed along a substrate holder between 0.5" and 12" away from the inlet where gases are introduced into the reactor. In order to assess the extent to which our precursor material is being utilized along the length of the reactor, we placed a SiN<sub>x</sub> substrate 12" away from the inlet. This experiment used 600 cycles of our standard recipe with the substrate at 65.8 °C. For the substrate placed at the inlet, film closure is achieved under these same reaction conditions (Figure 3.16a). However, for the substrate placed 12" away from the inlet, the CuBr grains form as islands rather than a continuous film, as shown in Figure 3.21. We expect this result can be attributed to precursor consumption by the walls of the reactor tube.

However, if the Cu(hfac)(vtms) liquid volume in the bubbler was less than about 6 mL, the liquid-gas surface area was lower, because of the tapered shape of the bubbler bottom. Under this reduced surface area condition, we observed growth per cycles of less than 0.12 nm/cycle.

From these observations, we draw the conclusion that the CVD reaction between Cu(hfac)(vtms) and HBr in our reactor takes place in a precursor-limited growth regime. The observation of the same film thickness for both 5 s and 0.1 s reaction wait times supports the conclusion that the film deposition is not limited by the chemical reaction time, under our conditions. Further, we reason that the CuBr film thickness decreases along the reactor length from inlet to outlet because either one or both precursors are being depleted. These observations are consistent with precursor-limited growth behavior. One cycle of our accelerated recipe takes 34.55 seconds, corresponding to a growth rate of 0.2 nm/min.

Seeking to improve this CuBr growth rate, we conducted a brief exploration of a third CuBr deposition recipe, this time employing open-valve mode. Open-valve mode recipes can be faster than closed-valve mode recipes because purging happens simultaneously with precursor dosing. In this recipe, the reactor is constantly purged with nitrogen, and alternating doses of Cu(hfac)(vtms) and



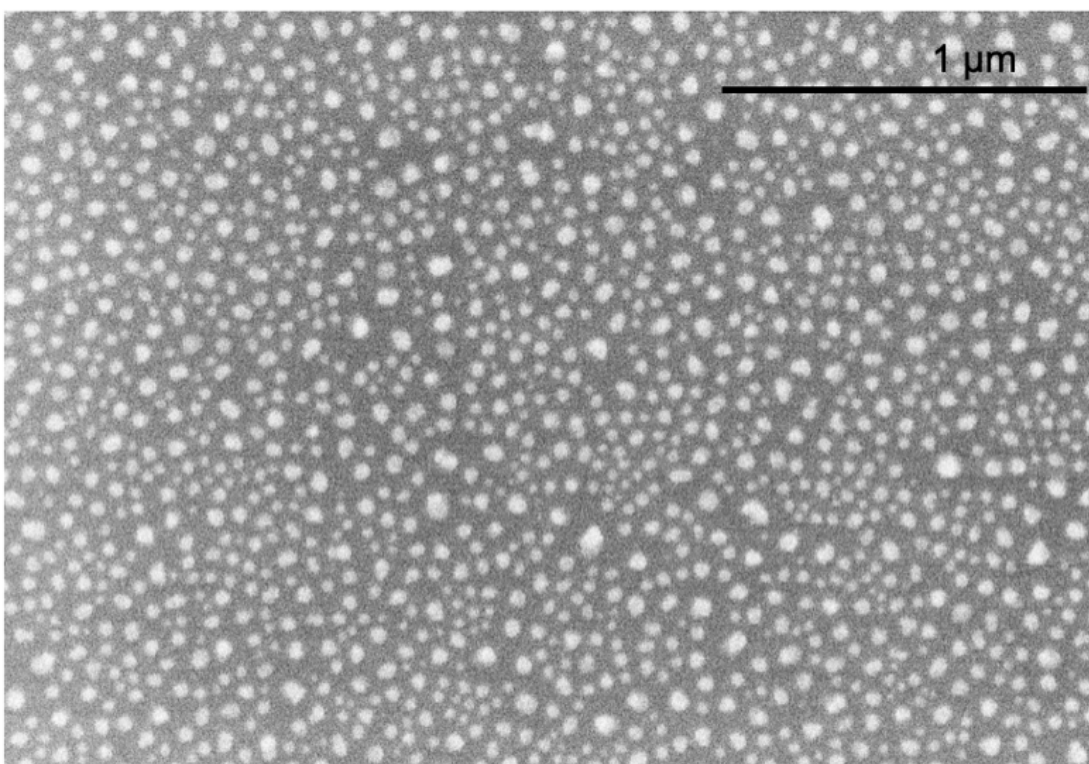
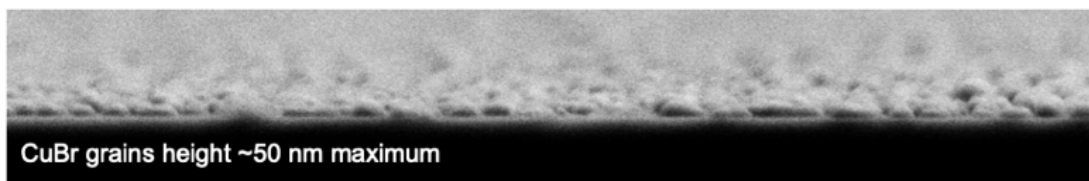


Figure 3.21: SEM Micrograph of CuBr Deposited on SiN<sub>x</sub> at 1 foot from reactor inlet.

HBr are released into the reactor while purging is still occurring. This recipe is described in further detail in the Methods section. Our preliminary results using open-valve mode suggest that CuBr can be grown with a growth per cycle of at least 0.18 nm / cycle. One cycle of this open-valve recipe takes only 10.55 seconds, corresponding to a growth rate of 1 nm/min. We expect that further increase in growth rate can be achieved via other modifications to our procedures, including, for example, increasing the precursor gas pressures via increasing the Cu(hfac)(vtms) bubbler temperature and HBr regulator outlet pressure. We also expect that further increase in growth rate can be achieved by scaling up to another reactor design that permits continuous-flow CVD.

### 3.4.7 OPTICAL CHARACTERIZATION

As a sample for optical characterization, we deposited 120 nm of CuBr (1200 cycles) using our standard recipe at a substrate temperature of 83.4 °C on a substrate which was 40 nm silicon nitride on quartz. Transmittance (T) and reflectance (R) were measured for three samples: quartz (Figure 3.22), 40 nm silicon nitride on quartz (Figure 3.23), and 120 nm CuBr on 40 nm silicon nitride on quartz (Figure 3.24). Absorbance (A) was calculated as  $A = 1 - T - R$  and is plotted alongside T and R. These samples are shown in the photograph in Figure 3.26. The method developed by Cesaria<sup>31</sup> was used to extract the absorption coefficient of CuBr as a function of wavelength. As shown in the plot of absorption coefficient  $\alpha$  versus wavelength  $\lambda$  (Figure 3.25), this CuBr sample is mostly transparent in the range of visible light, ca. 400 - 800 nm. The expected excitonic peaks are apparent at 2.96 eV ( $Z_1$ ), 2.97 eV ( $Z_2$ ) and 3.12 ( $Z_3$ ).<sup>37</sup>

### 3.4.8 ELECTRICAL CHARACTERIZATION

Electrical characterization of the CuBr thin films was carried out using an AC Hall-effect measurement system. The CuBr sample was 75 nm thick, as shown in Figure 3.27. The sheet resistance for

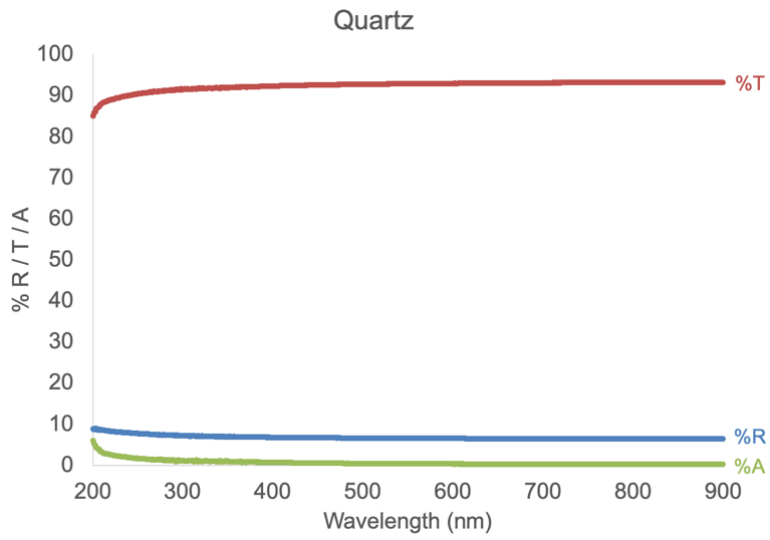


Figure 3.22: UV-Vis Spectrum of Quartz. Transmission through quartz is about 93% in the visible region.

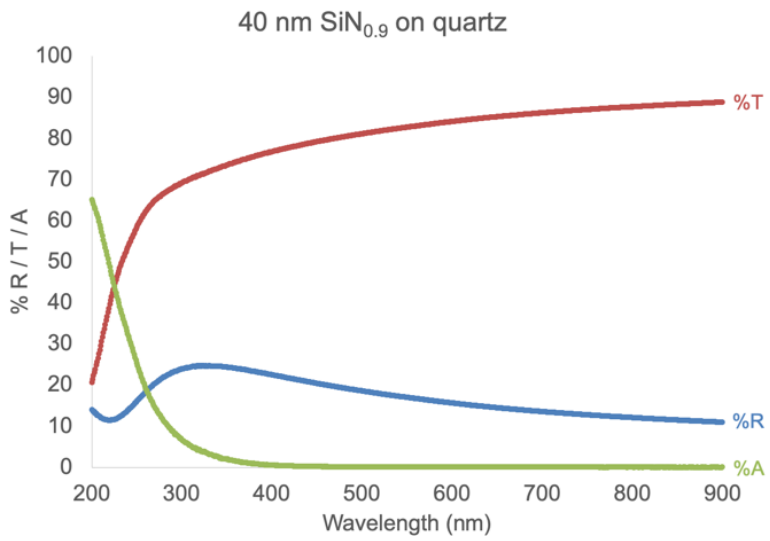


Figure 3.23: UV-Vis Spectrum of 40 nm SiN<sub>x</sub> on quartz.

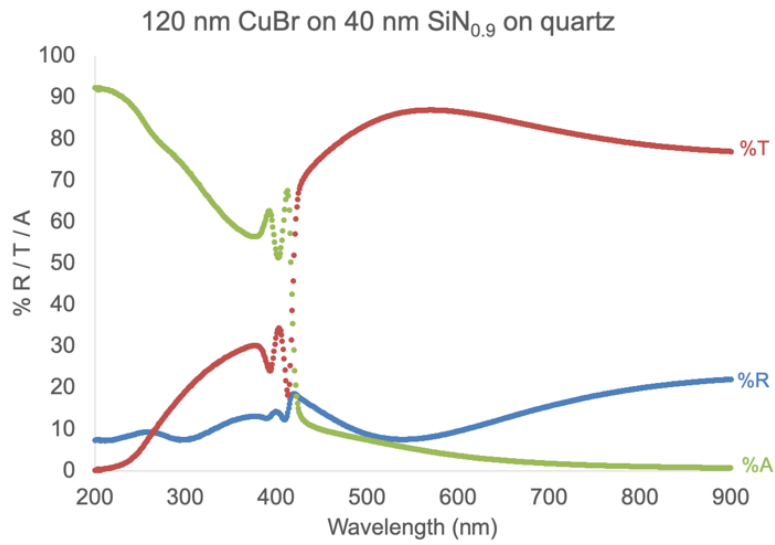


Figure 3.24: UV-Vis Spectrum of 120 nm CuBr on 40 nm SiN<sub>x</sub> on quartz.

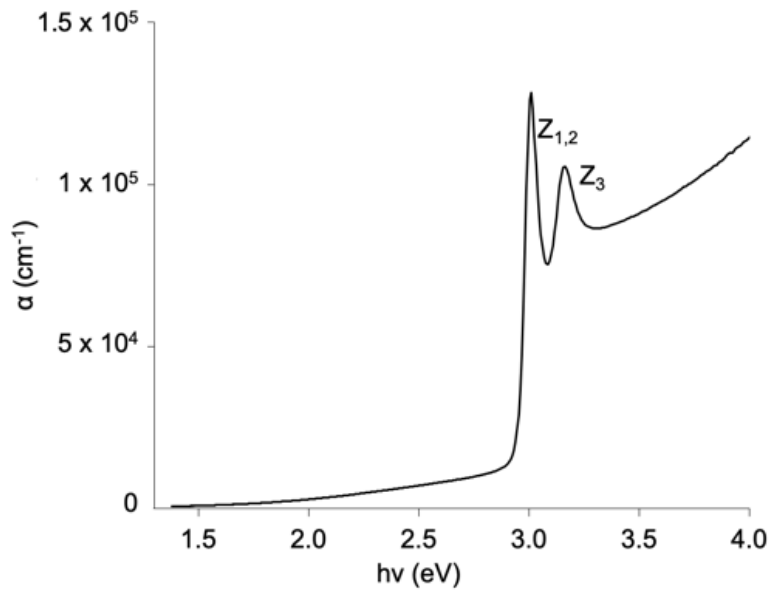
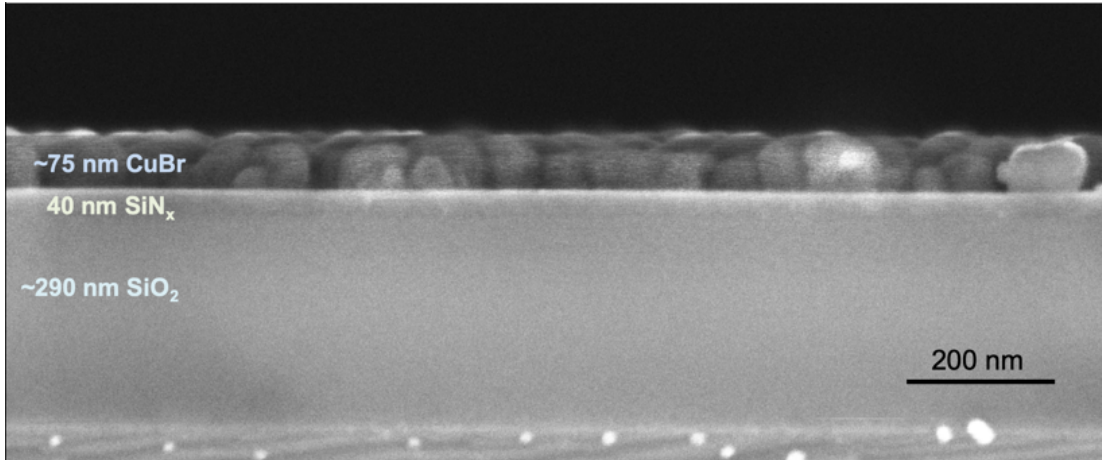


Figure 3.25: Absorption coefficient versus energy for 120 nm CuBr on 40 nm SiN<sub>x</sub> on quartz, grown using our standard recipe at 83 °C. Our CuBr films are transparent in the visible region.

**Figure 3.26:** Photograph of three samples: (left) quartz, (center) 40 nm silicon nitride on quartz, and (right) 200 nm of CuBr on 40 nm silicon nitride on quartz, with the CuBr having been deposited at 83.4 °C using our accelerated recipe.



**Figure 3.27:** SEM Micrograph of CuBr sample used for Hall effect measurement.

this sample was  $5 \times 10^5 \text{ } \Omega/\text{sq}$ , leading us to calculate a resistivity of  $3.7 \pm 1.0 \text{ } \Omega \cdot \text{cm}$ . The charge carrier type was found to be holes. The hole concentration was found to be  $5.5 \pm 1.6 \times 10^{17}$  carriers per  $\text{cm}^3$  and the hole mobility was measured at  $3.0 \pm 0.2 \text{ cm}^2 \text{ V}^{-1} \text{ s}^{-1}$ , which is in line with the literature.<sup>37,7</sup>

### 3.4.9 CONTACT ANGLE ANALYSIS

Consider a liquid droplet on a solid surface, shown in Figure 3.28. Aside from gravity, three other forces are exerted on the droplet at the three-phase interface shown. We denote the surface free energy of a solid surface exposed to a vapor as  $\gamma_{SV}$ , in units of energy per unit area ( $\text{kg}/\text{s}^2$  in SI units).

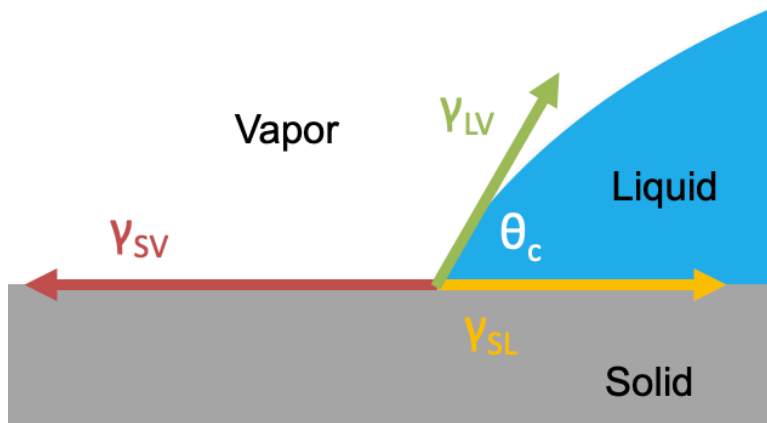


**Figure 3.28:** Cross-section of a liquid droplet on a solid surface indicating contact angle  $\vartheta_c$ .

This quantity is also known as the interfacial free energy of the solid-vapor interface. We denote the surface tension of a liquid exposed to a vapor as  $\gamma_{SV}$ , in units of force per unit length (also  $\text{kg/s}^2$  in SI units). This quantity is also known as the interfacial free energy of the solid-liquid interface. We finally denote the interfacial free energy between the solid and liquid as  $\gamma_{SL}$ , in units of energy per unit area ( $\text{kg/s}^2$  in SI units).

A free-body diagram of the interfacial free energy forces exerted at the 3-phase interfacial point is shown to scale in Figure 3.28. The equilibrium shape of the droplet is determined by minimization of free energy. Once the equilibrium shape of the droplet is formed, the forces balance each other and net force is zero. Considering forces along the x-axis, forces pulling the droplet to the left must equal forces pulling the droplet to the right:

$$\gamma_{SV} = \gamma_{SL} + \gamma_{LV} \cos \vartheta_c \quad (3.1)$$

This expression is known as Young's equation.<sup>38</sup> This form of the equation indicates that wetting is favored by high solid-vapor surface free energy  $\gamma_{SV}$ , low interfacial free energy  $\gamma_{LV}$ , and low liquid surface free energy  $\gamma_{SL}$ . Unfortunately, it is not easy to directly measure the interfacial free energy

values  $\gamma$ . However, it is practical to measure  $\vartheta_c$ . Re-arranging Equation 3.1, we obtain an expression isolating  $\vartheta_c$ :

$$\cos \vartheta_c = \frac{\gamma_{SV} - \gamma_{SL}}{\gamma_{LV}} \quad (3.2)$$

The work needed to separate the liquid from the solid is known as the “work of adhesion,” denoted  $W_A$ . This work represents the difference in energy per unit area between the adhered and unadhered states:

$$W_A = \gamma_{SV} + \gamma_{LV} - \gamma_{SL} \quad (3.3)$$

Substituting Equation 3.3 into Equation 3.1, we arrive at the Young-Dupré equation relating  $W_A$  to  $\vartheta_c$ :

$$W_A = \gamma_{LV}(1 + \cos \vartheta_c) \quad (3.4)$$

Two materials adhere due to various microscopic forces at the material surfaces: covalent bonding, hydrogen bonding and van der Waals forces. Within this last category are three main interactions: Keesom forces which arise from molecules with permanent dipoles,<sup>39</sup> Debye forces which arise from a molecule with a permanent dipole inducing a temporary dipole in a neighboring molecule,<sup>40</sup> and London dispersion forces which arise when instantaneous dipoles are induced.<sup>41</sup> Many methods have been proposed that decompose  $W_A$  and  $\gamma$  into components that account for these forces. One widely accepted decomposition of  $\gamma$  is decomposition into two components: the “dispersive” component  $\gamma^d$  accounts for interactions between temporary dipoles and the “polar” component  $\gamma^p$  accounts for interactions between permanent dipoles. These interactions are additive, such that:

$$\gamma = \gamma^d + \gamma^p \quad (3.5)$$

The work of adhesion required to overcome these adhesive forces has been modeled by many, and

one widely applied approach is that of Owens and Wendt.<sup>42</sup> These authors determine the work of adhesion by using a geometric mean:

$$W_A = 2 \left( \sqrt{\gamma_{LV}^d \gamma_{SV}^d} + \sqrt{\gamma_{LV}^p \gamma_{SV}^p} \right) \quad (3.6)$$

By combining equations 3.3, 3.5, and 3.8, we may write the following equation that relates the contact angle  $\vartheta_c$  of a liquid on a surface with the polar and dispersive components of the interfacial free energies of the solid and the liquid (in the vapor of the liquid, not ambient atmosphere\*). The goal of this calculation is to be able to calculate unknown  $\gamma_{SV}$  values from known  $\gamma_{LV}$  values and measured  $\vartheta_c$  values.

$$\gamma_{LV}(1 + \cos \vartheta_c) = 2 \left( \sqrt{\gamma_{LV}^d \gamma_{SV}^d} + \sqrt{\gamma_{LV}^p \gamma_{SV}^p} \right) \quad (3.7)$$

We rearrange this equation to produce a formula in the format  $y = mx + b$ , which will enable a statistical best fit line from which the most accurate values of  $\gamma_{SV}^p$  and  $\gamma_{SV}^d$  can be determined from several test liquids:

$$\frac{\gamma_{LV}(1 + \cos \vartheta_c)}{2\sqrt{\gamma_{LV}^d}} = \left( \sqrt{\gamma_{SV}^p} \right) \left( \frac{\sqrt{\gamma_{LV}^p}}{\sqrt{\gamma_{LV}^d}} \right) + \sqrt{\gamma_{SV}^d} \quad (3.8)$$

In order to estimate  $\gamma_{SV}$  for a solid surface of interest, one can use a test liquid with known  $\gamma_{LV}^p$  and  $\gamma_{LV}^d$  values, and measure  $\vartheta_c$  of the liquid on the surface. In collaboration with Ms. Eliza Spear, a battery of test liquids was assembled with polar and dispersive components of surface free energy spanning a large range: diiodomethane, thiodiglycol, deionized water, and ethylene glycol. The polar and dispersive components of surface free energy were obtained from Adão et al.<sup>43</sup> for the former three liquids and van Oss<sup>44</sup> for the latter four liquids. The results of these experiments and analysis are shown in Figure 3.29. We find that CuBr clearly ages within 5 days, likely to become a

---

\*Experimentally, is often not easily feasible to create an atmosphere of the liquid vapor, and so often researchers use normal atmospheric ambient conditions instead



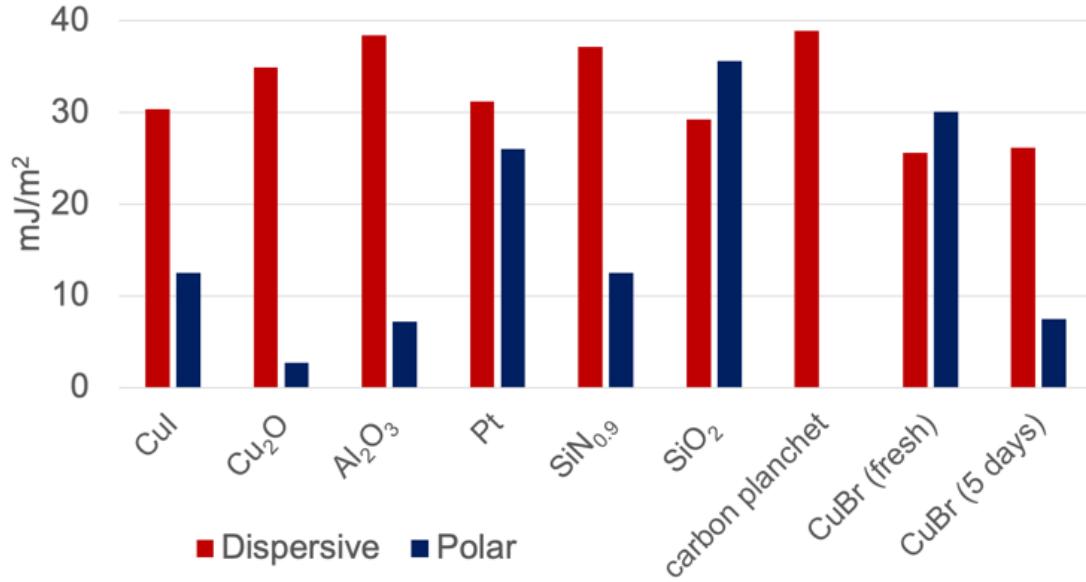


**Figure 3.29:** Calculated polar and dispersive free energy components for several surfaces. The CuI, Cu<sub>2</sub>O, and Al<sub>2</sub>O<sub>3</sub> values are extracted from data in the PhD dissertation of Dr. Rachel Heasley.<sup>45</sup>

copper oxide on the surface. This result about CuBr oxidation provides new context for our prior results.<sup>33</sup>

Ultimately we want to estimate the interfacial free energy between two solids, CuBr and the various substrates. To estimate the interfacial free energy between two solids, we turn to work by Girifalco et al.,<sup>46</sup> whose equation uses the dispersive and polar components of the solid-vapor surface free energy of two materials 1 and 2:

$$\gamma_{12} = \gamma_1 + \gamma_2 - 2 \left( \sqrt{\gamma_1^d \gamma_2^d} + \sqrt{\gamma_1^p \gamma_2^p} \right) \quad (3.9)$$

As is apparent by inspection of Equation 3.9, interfacial free energy is minimized when the two materials have quantitatively similar dispersive components and quantitatively similar polar components of free energy.

The results of this analysis are shown in Figure 3.30. In order from best to poorest wetting match

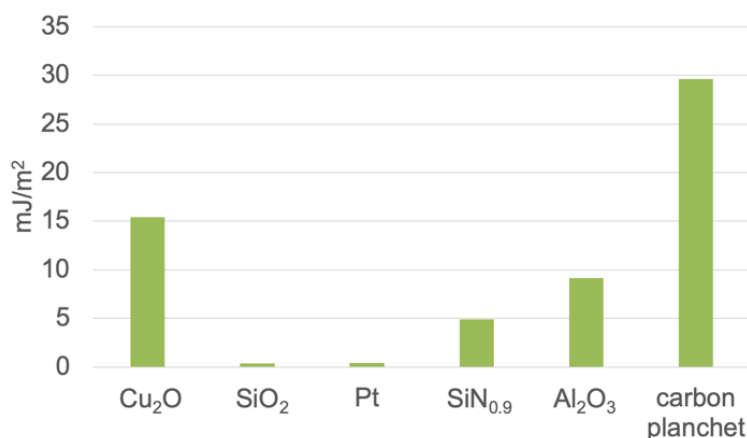


**Figure 3.30:** Calculated interfacial free energy components for CuBr films and substrates.

for CuBr, the substrates rank as follows: silica (0.4), Pt (0.4), silicon nitride (4.9), alumina (9.2), cupric oxide (15.4), and glassy carbon (29.6), all in units of mJ/m<sup>2</sup>. These results predict that we should observe good wetting of CuBr on silica and poor wetting of CuBr on glassy carbon. However, we observe that our CuBr films are continuous on glassy carbon, silicon nitride and platinum, whereas they poorly wet silica and alumina. From the mismatch between the deposited CuBr morphologies and the contact angle measurements, we surmise that these open-air, room-temperature contact angle measurements do not accurately capture the interfacial free energy values of the substrates when under reaction conditions: 83 °C and with reactant headspace gases. In particular, we envision that the chemistry of the reaction is the most likely cause of altered interfacial free energy. For example, the neutral ligand used in Cu(hfac)(vtms), vinyltrimethylsilane, is present in the reactor stoichiometrically with copper, and moreover silanes are known adhesion promoters.<sup>47</sup> Vtms concentration in particular is known<sup>48</sup> to alter the growth versus nucleation rates in the CVD deposition of Cu from Cu(hfac)(vtms). Clearly, the surface chemistry under our reaction conditions is more complicated than can be accurately measured outside the reactor. Our work to understand the *in situ* surface properties is ongoing. Dosing in extra vtms or silanes and/or alternate precur-

sors with alternate neutral ligands are some of the future research avenues we may pursue to further understand the science underlying our continuous films.

### 3.5 CONCLUSION

Using Cu(hfac)(vtms) and HBr as precursors, we report direct chemical vapor deposition of continuous cuprous bromide thin films, which represents the first in the literature to the best of our knowledge. By controlling the growth conditions and choice of substrate, we can produce apparently continuous films of CuBr at low substrate temperatures from 65 to 110 °C. A more detailed study of how our reaction chemistry enables continuous film growth is underway.

## References

- [1] T. Minami, “Transparent conducting oxide semiconductors for transparent electrodes,” *Semiconductor Science and Technology*, vol. 20, pp. S35–S44, Apr. 2005.
- [2] Y. Ogo, H. Hiramatsu, K. Nomura, H. Yanagi, T. Kamiya, M. Hirano, and H. Hosono, “P-channel thin-film transistor using p-type oxide semiconductor, SnO,” *Applied Physics Letters*, vol. 93, p. 032113, July 2008.
- [3] K.-C. Wang, J.-Y. Jeng, P.-S. Shen, Y.-C. Chang, E. W.-G. Diau, C.-H. Tsai, T.-Y. Chao, H.-C. Hsu, P.-Y. Lin, P. Chen, T.-F. Guo, and T.-C. Wen, “P-type Mesoscopic Nickel Oxide/Organometallic Perovskite Heterojunction Solar Cells,” *Scientific Reports*, vol. 4, Apr. 2014.
- [4] M. Nolan, “Defects in Cu<sub>2</sub>O, CuAlO<sub>2</sub> and SrCu<sub>2</sub>O<sub>2</sub> transparent conducting oxides,” *Thin Solid Films*, vol. 516, pp. 8130–8135, Sept. 2008.
- [5] K. H. L. Zhang, K. Xi, M. G. Blamire, and R. G. Egdell, “P-type transparent conducting oxides,” *Journal of Physics: Condensed Matter*, vol. 28, p. 383002, Sept. 2016.
- [6] M. Grundmann, F.-L. Schein, M. Lorenz, T. Böntgen, J. Lenzner, and H. von Wenckstern, “Cuprous iodide: A p-type transparent semiconductor, history, and novel applications: Cuprous iodide,” *physica status solidi (a)*, pp. n/a–n/a, Aug. 2013.
- [7] P. Knauth, Y. Massiani, and M. Pasquinelli, “Semiconductor Properties of Polycrystalline CuBr by Hall Effect and Capacitive Measurements,” *physica status solidi (a)*, vol. 165, pp. 461–465, Feb. 1998.
- [8] N. Yamada, R. Ino, and Y. Ninomiya, “Truly Transparent p-Type  $\gamma$ -CuI Thin Films with High Hole Mobility,” *Chemistry of Materials*, vol. 28, pp. 4971–4981, July 2016.
- [9] C. Yang, D. Souchay, M. Kneiß, M. Bogner, H. M. Wei, M. Lorenz, O. Oeckler, G. Benstetter, Y. Q. Fu, and M. Grundmann, “Transparent flexible thermoelectric material based on non-toxic earth-abundant p-type copper iodide thin film,” *Nature Communications*, vol. 8, p. 16076, July 2017.

- [10] J. A. Christians, R. C. M. Fung, and P. V. Kamat, "An Inorganic Hole Conductor for Organo-Lead Halide Perovskite Solar Cells. Improved Hole Conductivity with Copper Iodide," *Journal of the American Chemical Society*, vol. 136, pp. 758–764, Jan. 2014.
- [11] H. Zhu, A. Liu, and Y.-Y. Noh, "Transparent Inorganic Copper Bromide (CuBr) p-Channel Transistors Synthesized From Solution at Room Temperature," *IEEE Electron Device Letters*, vol. 40, pp. 769–772, May 2019.
- [12] W.-Y. Chen, L.-L. Deng, S.-M. Dai, X. Wang, C.-B. Tian, X.-X. Zhan, S.-Y. Xie, R.-B. Huang, and L.-S. Zheng, "Low-cost solution-processed copper iodide as an alternative to PEDOT:PSS hole transport layer for efficient and stable inverted planar heterojunction perovskite solar cells," *J. Mater. Chem. A*, vol. 3, no. 38, pp. 19353–19359, 2015.
- [13] A. Cowley, F. O. Lucas, E. Gudimenko, M. M. Alam, D. Danieluk, A. L. Bradley, and P. J. McNally, "Electroluminescence of  $\gamma$ -CuBr thin films via vacuum evaporation deposition," *Journal of Physics D: Applied Physics*, vol. 43, p. 165101, Apr. 2010.
- [14] D. Kim, M. Nakayama, O. Kojima, I. Tanaka, H. Ichida, T. Nakanishi, and H. Nishimura, "Thermal-strain-induced splitting of heavy- and light-hole exciton energies in CuI thin films grown by vacuum evaporation," *Physical Review B*, vol. 60, pp. 13879–13884, Nov. 1999.
- [15] A. Yanase and Y. Segawa, "Two different in-plane orientations in the growths of cuprous halides on MgO(001)," *Surface Science*, vol. 329, pp. 219–226, May 1995.
- [16] J.-L. Seguin, M. Bendahan, G. Lollmun, M. Pasquinelli, and P. Knauth, "Preparation of thin films of copper(I) bromide by r.f. sputtering: Morphology and electrical properties," *Thin Solid Films*, vol. 323, pp. 31–36, June 1998.
- [17] T. Tanaka, K. Kawabata, and M. Hirose, "Transparent, conductive CuI films prepared by rf-dc coupled magnetron sputtering," *Thin Solid Films*, vol. 281-282, pp. 179–181, Aug. 1996.
- [18] W. M. K. P. Wijekoon, M. Y. M. Lyktey, P. N. Prasad, and J. F. Garvey, "Characterization of copper iodide thin films fabricated via laser-assisted molecular-beam deposition," *Journal of Applied Physics*, vol. 74, pp. 5767–5772, Nov. 1993.
- [19] P. Sirimanne, M. Rusop, T. Shirata, T. Soga, and T. Jimbo, "Characterization of transparent conducting CuI thin films prepared by pulse laser deposition technique," *Chemical Physics Letters*, vol. 366, pp. 485–489, Dec. 2002.
- [20] V. Gottschalch, S. Blaurock, G. Benndorf, J. Lenzner, M. Grundmann, and H. Krautscheid, "Copper iodide synthesized by iodization of Cu-films and deposited using MOCVD," *Journal of Crystal Growth*, vol. 471, pp. 21–28, Aug. 2017.
- [21] C. Yang, M. Kneiß, M. Lorenz, and M. Grundmann, "Room-temperature synthesized copper iodide thin film as degenerate p-type transparent conductor with a boosted figure of merit," *Proceedings of the National Academy of Sciences*, vol. 113, pp. 12929–12933, Nov. 2016.

- [22] Y. Lee, J. W. DuMont, A. S. Cavanagh, and S. M. George, "Atomic Layer Deposition of  $\text{AlF}_3$  Using Trimethylaluminum and Hydrogen Fluoride," *The Journal of Physical Chemistry C*, vol. 119, pp. 14185–14194, June 2015.
- [23] M. Mäntymäki, J. Hämäläinen, E. Puukilainen, T. Sajavaara, M. Ritala, and M. Leskelä, "Atomic Layer Deposition of LiF Thin Films from  $\text{Li}(\text{thd})_3$ ,  $\text{Mg}(\text{thd})_2$ , and  $\text{TiF}_4$  Precursors," *Chemistry of Materials*, vol. 25, pp. 1656–1663, May 2013.
- [24] G. Popov, M. Mattinen, T. Hatanpää, M. Vehkamäki, M. Kemell, K. Mizohata, J. Räisänen, M. Ritala, and M. Leskelä, "Atomic Layer Deposition of  $\text{PbI}_2$  Thin Films," *Chemistry of Materials*, vol. 31, pp. 1101–1109, Feb. 2019.
- [25] T. Pilvi, T. Hatanpää, E. Puukilainen, K. Arstila, M. Bischoff, U. Kaiser, N. Kaiser, M. Leskelä, and M. Ritala, "Study of a novel ALD process for depositing  $\text{MgF}_2$  thin films," *Journal of Materials Chemistry*, vol. 17, no. 48, p. 5077, 2007.
- [26] G. Natarajan, P. S. Maydannik, D. C. Cameron, I. Akopyan, and B. V. Novikov, "Atomic layer deposition of  $\text{CuCl}$  nanoparticles," *Applied Physics Letters*, vol. 97, p. 241905, Dec. 2010.
- [27] P. S. Maydannik, G. Natarajan, and D. C. Cameron, "Atomic layer deposition of nanocrystallite arrays of copper(I) chloride for optoelectronic structures," *Journal of Materials Science: Materials in Electronics*, vol. 28, pp. 11695–11701, Aug. 2017.
- [28] R. Krumpolec, T. Homola, D. Cameron, J. Humlíček, O. Caha, K. Kuldová, R. Zazpe, J. Píkrýl, and J. Macak, "Structural and Optical Properties of Luminescent Copper(I) Chloride Thin Films Deposited by Sequentially Pulsed Chemical Vapour Deposition," *Coatings*, vol. 8, p. 369, Oct. 2018.
- [29] R. Heasley, C. M. Chang, L. M. Davis, K. Liu, and R. G. Gordon, "Vapor deposition of copper(I) bromide films via a two-step conversion process," *Journal of Vacuum Science & Technology A: Vacuum, Surfaces, and Films*, vol. 35, p. 01B109, Jan. 2017.
- [30] D. Ritter and K. Weiser, "Suppression of interference fringes in absorption measurements on thin films," *Optics Communications*, vol. 57, pp. 336–338, Apr. 1986.
- [31] M. Cesaria, A. P. Caricato, and M. Martino, "Realistic absorption coefficient of each individual film in a multilayer architecture," *Journal of Optics*, vol. 17, p. 025610, Feb. 2015.
- [32] T. K. Fai, *Investigating the Open-Circuit Voltage Deficit in  $\text{Cu}_2\text{ZnSn}(\text{S},\text{Se})_4$  Solar Cells*. PhD dissertation, Nanyang Technological University, Singapore, 2015.
- [33] R. Heasley, L. M. Davis, D. Chua, C. M. Chang, and R. G. Gordon, "Vapor Deposition of Transparent, p-Type Cuprous Iodide Via a Two-Step Conversion Process," *ACS Applied Energy Materials*, vol. 1, pp. 6953–6963, Dec. 2018.

- [34] P. Doppelt, "Copper CVD precursors and processes for advanced metallization," *Microelectronic Engineering*, vol. 37/38, pp. 89–95, 1997.
- [35] W. M. Haynes, *CRC Handbook of Chemistry and Physics*. 95th ed., 2014.
- [36] P. Doppelt and T. H. Baum, "Chemical Vapor Deposition of Copper for IC Metallization: Precursor Chemistry and Molecular Structure," *MRS Bulletin*, vol. 19, pp. 41–48, Aug. 1994.
- [37] O. Madelung, *Semiconductors: Data Handbook*. Springer, 2013. OCLC: 968555009.
- [38] T. Young, "An essay on the cohesion of fluids," *Philosophical Transactions of the Royal Society of London*, vol. 95, pp. 65–87, Jan. 1805.
- [39] W. Keesom, "Van der Waals attractive force," *Physikalische Zeitschrift*, vol. 22, pp. 129–141, 1921.
- [40] P. Debye, "Van der Waals cohesion forces," *Physikalische Zeitschrift*, vol. 21, pp. 178–187, 1920.
- [41] F. London, "The general theory of molecular forces," *Transactions of the Faraday Society*, vol. 33, p. 8, 1937.
- [42] D. K. Owens and R. C. Wendt, "Estimation of the surface free energy of polymers," *Journal of Applied Polymer Science*, vol. 13, pp. 1741–1747, Aug. 1969.
- [43] M. H. V. C. Adão, B. J. V. Saramago, and A. C. Fernandes, "Estimation of the Surface Properties of Styrene-Acrylonitrile Random Copolymers from Contact Angle Measurements," *Journal of Colloid and Interface Science*, vol. 217, pp. 94–106, Sept. 1999.
- [44] C. J. van Oss, *Interfacial Forces in Aqueous Media*. CRC Press, May 2006.
- [45] R. Heasley, *Vapor Deposition of Halide Perovskites and Hole-Transport Materials for Use in Thin-Film Photovoltaics*. PhD dissertation, Harvard University, Aug. 2017.
- [46] L. A. Girifalco and R. J. Good, "A Theory for the Estimation of Surface and Interfacial Energies. I. Derivation and Application to Interfacial Tension," *The Journal of Physical Chemistry*, vol. 61, pp. 904–909, July 1957.
- [47] P. Harding and J. Berg, "The Adhesion Promotion Mechanism of Organofunctional Silanes," *Journal of Applied Polymer Science*, vol. 67, pp. 1025–1033, 1998.
- [48] S. Babar, L. M. Davis, P. Zhang, E. Mohimi, G. S. Girolami, and J. R. Abelson, "Chemical Vapor Deposition of Copper: Use of a Molecular Inhibitor to Afford Uniform Nanoislands or Smooth Films," *ECS Journal of Solid State Science and Technology*, vol. 3, no. 5, pp. Q79–Q83, 2014.

# 4

## Toward Flexible Hybrid Polymer/Ceramic Dielectric Thin Films

### 4.1 ABSTRACT

Emerging flexible electronic devices will require dielectric coatings that are both flexible and heat-stable. The goal of this project is to invent new materials that meet these requirements and to de-



posit thin-film coatings of these materials atop devices of arbitrary geometry. Our approach has been to co-polymerize a hybrid organic-ceramic dielectric material using chemical vapor deposition (CVD). Specifically, alumina will be hybridized with polyimide. We have designed reaction chemistry, designed and built a CVD reactor, and deposited and characterized dielectric thin films. The research in this chapter has been supported by an internal research and development (IRAD) project at Draper Laboratory named Miniature-Multi-Wire Systems (MMS).

## 4.2 INTRODUCTION

### 4.2.1 MOTIVATION FOR HIGH-T FLEXIBLE DIELECTRIC COATINGS

Flexible electronics have been under development since the 1960s, when the first flexible solar panels were fabricated by thinning silicon wafers until they were thin enough to be relatively flexible (in this case,  $\approx 100 \mu\text{m}$ ) and attaching them to a plastic substrate.<sup>1,2</sup> Since then, the development of flexible electronics has expanded due to the many benefits promised by flexible electronics, including: the use of organic functional materials which can be chemically tuned to specify properties; thinning and therefore lightweighting, which facilitates mobility and transportation and may reduce cost; and use cases in wearable electronics and smart textiles or e-textiles, wherein components and interconnections are intrinsic to the fabric.<sup>3</sup> Currently, most research and development of flexible electronics in industry is for flexible displays and X-ray sensor arrays.<sup>4</sup> Pre-commercial research on flexible electronics varies widely in focus, with major efforts in conformally shaped electronics and elastically stretchable electronic surfaces.

An important emerging area wherein flexible electronics are required is electronic packaging, i.e. enclosures for electronic devices. Historically, the most common architecture in packaging electronics is an assembly of single- or multi-chip modules on a printed circuit board (PCB). Thus, complex circuits can be fabricated on a die, and these monolithic systems may be referred to as System on

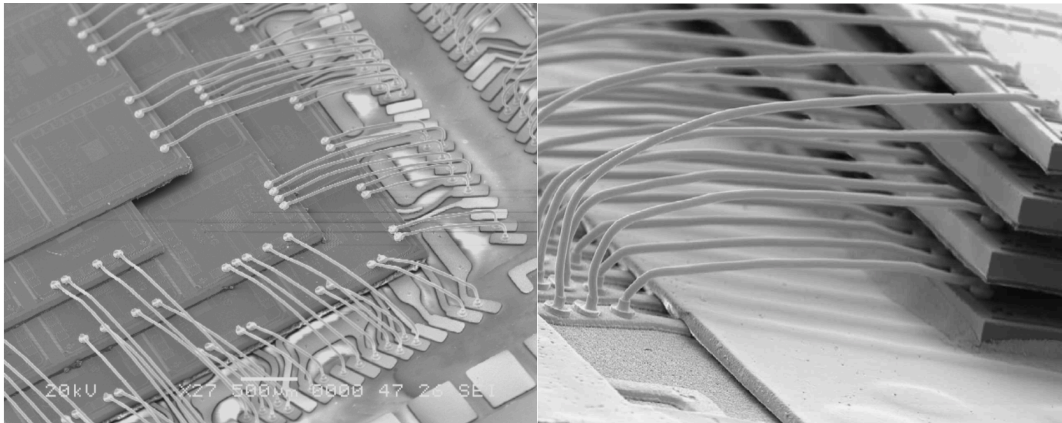


**Figure 4.1:** Example of stacked die, courtesy of Amkor:<sup>5</sup> wire bonding (left) and reverse wire bonding with gold studs on the die (right).

Chip (SoC). However, in some devices, modularity beyond what can be provided by SoC is desired. In the early 1990s, defense applications (often classified) required the integration of heterogeneous chip types. To enable these devices, a new advanced packaging platform has emerged which is known as System in Package (SiP). In this packaging platform, two or more dissimilar chips are integrated into the same package. These diverse chips to be integrated into one package may include microelectromechanical systems (MEMS), optical or radio frequency components, and biochemical components. One common way to integrate these diverse chips in SiP packages is to use die stacking. As shown in Figure 4.1, dies are stacked atop each other and then wire bonded to each other. In SoC packages, interconnects are often two-dimensional, but in SiP, the wires that interconnect the dies are three-dimensional and flexible, presenting new challenges for both electrical and mechanical performance of these wires. Although the early defense applications for SiP did not require the production of large volumes of devices, SiP is gaining popularity in the commercial world. The main driver of this growth is complex miniature devices from smartphones to pacemakers, and the broader world of “Internet of Things” devices. For such applications, new high-throughput fabrication processes are needed to enable large-scale production of these devices commercially.

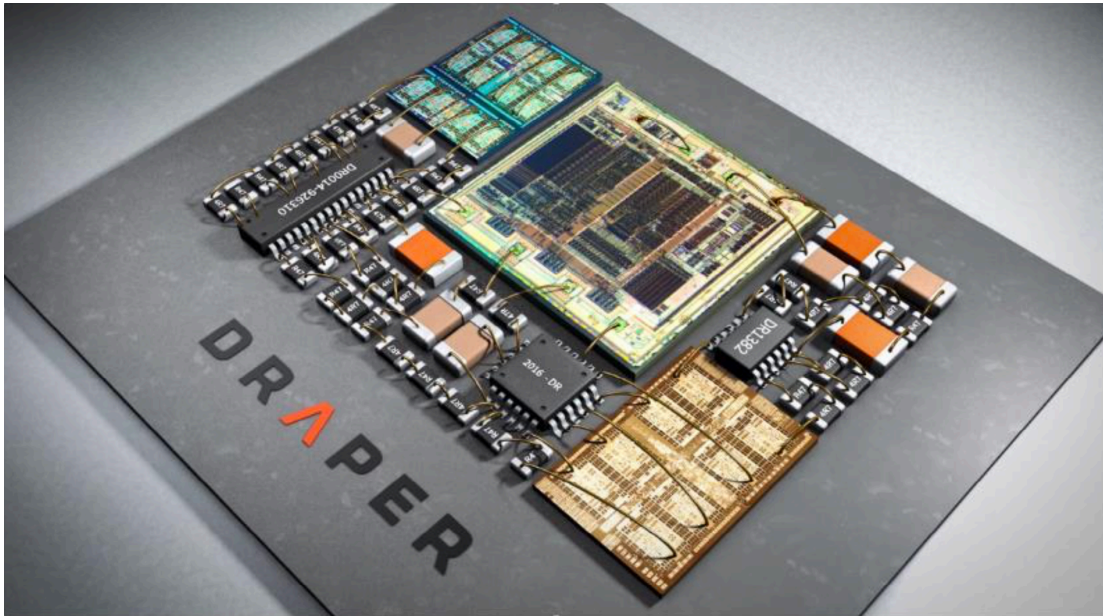


**Figure 4.2:** A simulated mock-up example of the Draper Miniature Multiwire Systems Technology. Components are fused to a substrate and interconnected via micro-coaxial cables using an automated bonder tool.

An internal research and development (IRAD) project at Draper named Miniature Multiwire Systems (MMS) was launched to use shielded micro-coaxial cables for all component interconnects. A coaxial cable, also known as a “coax,” is an electrical cable that has an inner “core” metal, surrounded by a tubular insulating layer, surrounded by an outer “shield” metal. In achieving the goal of micro coax cables, the MMS project will eliminate the time-consuming processes of laying out and fabricating the otherwise 2D interconnects for power and signal distribution. A mock-up example of an MMS-enabled device is shown in Figure 4.2. The micro-coaxial cables are first fabricated in a reel-to-reel process. Then, in a process similar to wire bonding, a tool spools the cables and strips the metal shield outer layer in order to bond the core and shield at both ends.<sup>6</sup> In these devices, both power and signals must be transmitted.

Coaxial cables may be used to transmit signals or power. In signal coaxial cables, data is carried in the core metal, and surrounding shield layers reduce attenuation loss. Power coaxial cables are

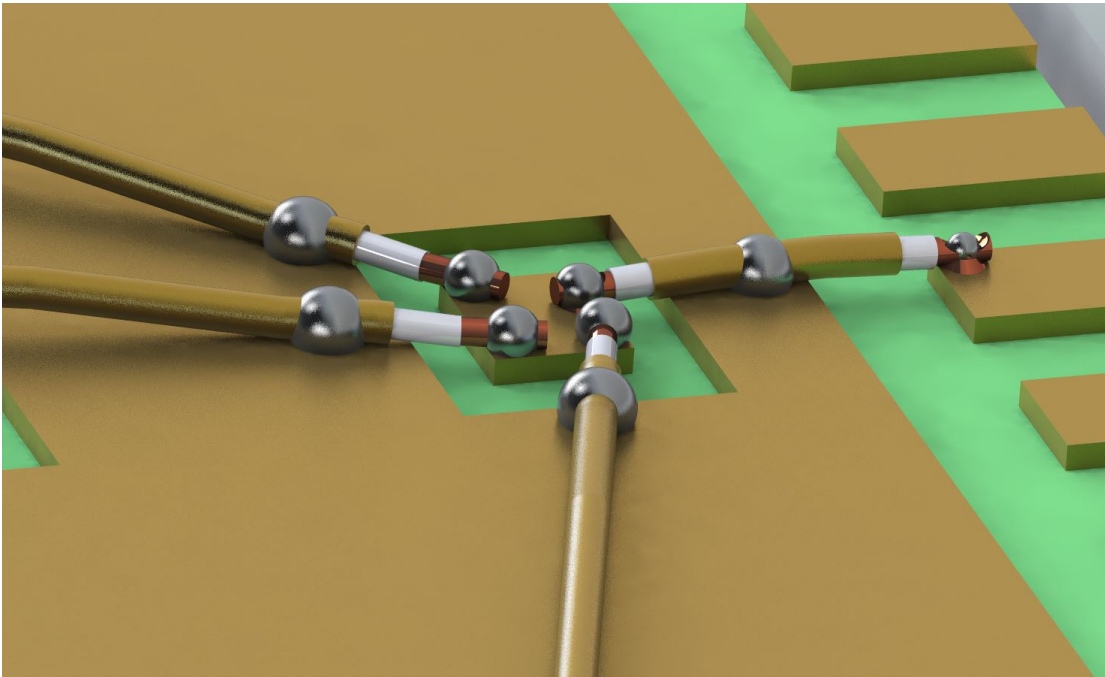


**Figure 4.3:** A simulated mock-up example of the Draper Miniature Multiwire Systems Technology. Separate electrical attachments to core and shield are shown.

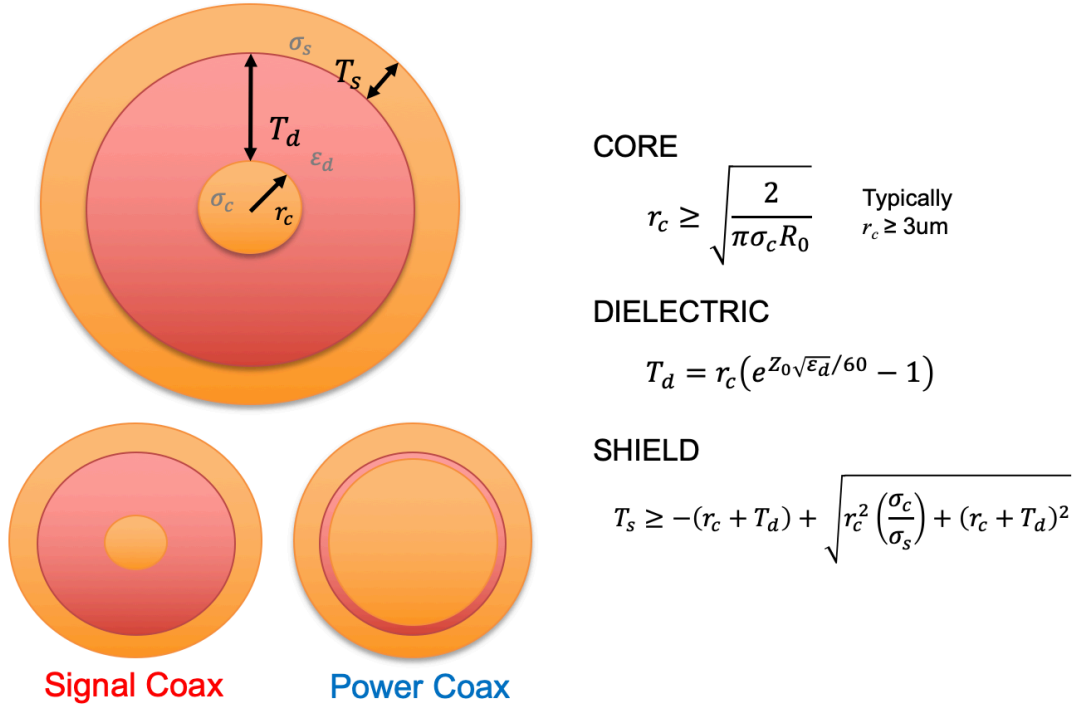
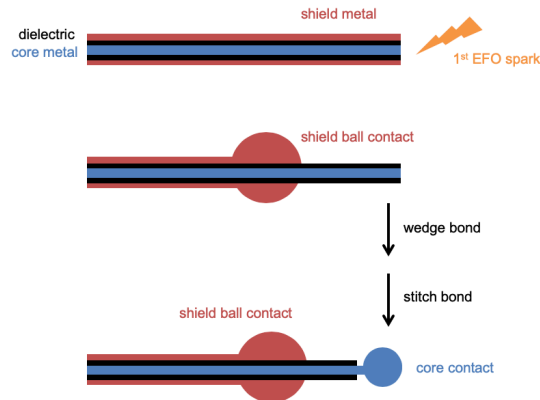


Figure 4.4: Signal and power coax will have different cross-sectional profiles because of their different functions.

configured solely for power distribution. Accordingly, signal coaxial cables and power coaxial cables have different performance metrics, leading to the use of different radii and materials, as shown in Figure 4.4. We focus in this thesis on power coaxial cables, aka “power coax.” These cables are used for power distribution. The technical drivers that determine the dimensions of the core include: mean coax length by power domain, number of connections per domain, material conductivity, skin depth and system impedance. The technical drivers that determine the dimensions of the dielectric include the dielectric constant and the core diameter. The technical drivers that determine the shield dimension include the core/shield conductivity ratio, the core diameter, and the skin depth.

Wiring interconnection technologies require a wire to be stripped and then bonded, creating electrical connections between different points and components. One such stripping technology proposed for power coax within the MMS project was the electric flame-off (EFO) method.<sup>7</sup> A



**Figure 4.5:** Coaxial cable before, during, and the electric flame-off process, reproduced from Meinhold et al.<sup>7</sup>

schematic of this method is shown in Figure 4.5. Typically, a first electrical spark is applied to the coaxial cable, melting and deforming the conductive shield layer locally, revealing the two inner layers. The most common conductive materials are copper and gold. The dielectric layers tend to be flexible polymers such as Parylene, polyurethane, and polyetherimide.

This thesis chapter is motivated by early work at Draper Laboratory using the EFO method on power coaxial wires using commercially available components. Although electrical insulation between the core and shield metals was desired, early attempts using EFO resulted in electrical connection – shorting – between the core and shield metals. The metal locally heats to roughly 1000 °C during the EFO process, a temperature at which organic insulators are known to decompose and become electrically conductive.<sup>8</sup> One strategy to solving this problem is to develop a method to deposit conformal dielectric coatings on wires, such that the dielectric will not become conductive when using the electric flame-off bonding method.

#### 4.2.2 REQUIREMENTS

##### MATERIAL PROPERTIES AND PERFORMANCE

There are several important qualities of the ideal dielectric coating for this application. The essential qualities are: (1) High mechanical strength and flexibility will enable the coated wire to be bent and spooled without the coating breaking or cracking (bend radius  $\approx 20 \times$  coax diameter), (2) the coating should be somewhat thin ( $\sim 500$  nm or less), (3) conformal, (4) pinhole-free, and (5) when the material is exposed to a local  $1000^\circ\text{C}$  spark for milliseconds, it should remain insulating after exposure to this spark and after bonding. One further quality that is not required but would be desirable is modularity at the molecular level because it would thereby be possible to tune the properties of the material by making slight changes to the molecular structure.

##### COATING PROCESS

Reproducibility is a foremost consideration for this project because application to electronic devices requires a high level of standardization and quality control. Additional factors include the amount of time required to apply the coating and the amortized cost of the coating. It is desirable that the dielectric coating process be compatible with reel-to-reel wire fabrication.

The choice of chemical vapor deposition (CVD) is appropriate because this technique is widely used to deposit conformal, pinhole-free, ultrathin materials reproducibly and with device-level quality. All else being equal, for this project we prefer the CVD variant, atomic layer deposition (ALD), in which precursor gases are evacuated from the chamber in between doses, leaving only surface-bound species. While ALD is slower than traditional CVD, ALD provides better control, which matched our desire for early process establishment with this project. Additionally, ALD processes are often able to be scaled to CVD after their initial development.

### 4.2.3 EXISTING DIELECTRIC COATINGS

To be used in a micro-coaxial cable compatible with EFO bonding, a thin film coating method/material must meet the requirements in Section 4.2.2. The overview in this section ascertains the shortcomings of existing dielectric coatings, motivating the development of a novel method/material.

In the field of systems engineering, a “tradespace” plot is commonly used by NASA, DARPA and others to analyze the complex resources, costs, and provisioning involved in large projects with multiple objectives. We developed a tradespace plot to analyze existing dielectric materials for suitability for this project. Parylene C and Kapton (the commercial name of a common polyimide) are popular choices as dielectric coatings for flexible electronic applications, because they have high flexibility. However, no organic dielectric will survive use temperatures above about 500 °C for extended periods of time (Figure 4.6). The requirements in Section 4.2.2 indicate that the coating used with EFO spark bonding must remain insulating after the application of a few milliseconds of exposure to 1000 °C heat. On the other hand, ceramic materials are found in the lower right-hand corner of this tradespace – they will survive the spark, but they are not flexible enough for the application. These drawbacks of the individual materials lead us to consider hybrid materials, whose organic component provides flexibility and whose inorganic component provides strength and prevents shorting even at the wire section exposed to an EFO spark, even if the organic section gets entirely decomposed in that section.

A few emerging hybrid dielectric coatings are fully or partially missing from Figure 4.6 because their parameter values have not yet been measured. These hybrid materials have been reviewed elsewhere, and three main categories exist: metalcones,<sup>9</sup> siloxane-based polymers,<sup>10</sup> and nanolaminates.<sup>11</sup> These materials are described next.

Metalcones are thin films grown by molecular layer deposition (MLD) by alternating pulses of the metalorganic precursors for ceramics with pulses of an organic “linker” molecule that bridges



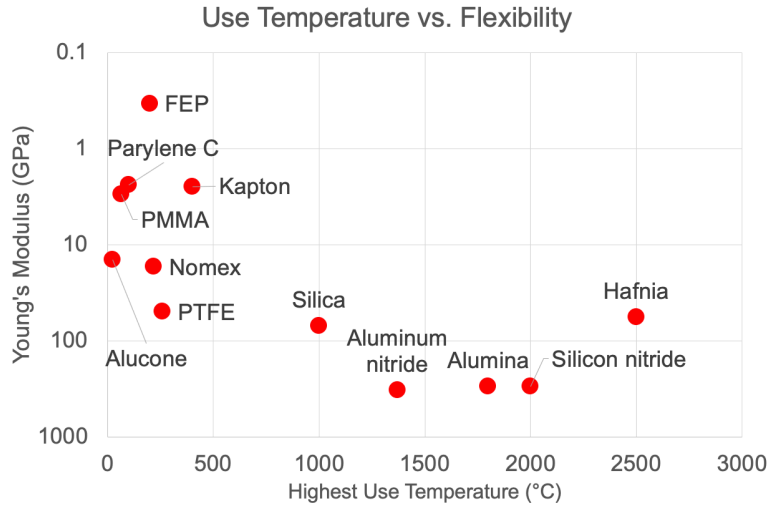


Figure 4.6: Temperature-Young's Modulus tradespace for common dielectric materials.

between the thin ceramic layers. The ceramics are typically oxides (e.g.  $\text{Al}_2\text{O}_3$ ,  $\text{ZnO}$ ) and the linker is often a diol, and thus the oxygen bridges covalently link the layers. However, two downsides of metalcones disqualify them for the purposes of the desired application. First, metalcones tend not to be very stable to exposure to ambient atmosphere since the linkers tend to hydrolyze. Second, metalcones are not as tunable as we desire. There is an upper limit on the flexible organic content of metalcones because the linker organic molecules cannot bond to each other (they are not polymers), so they must be bonded to a ceramic layer on either side. This gives a maximum organic:ceramic layer ratio of 1:1, and thus an upper limit on the organic content, and therefore the flexibility, of metalcones.

Siloxane-based polymers are beneficially highly thermally stable due to the Si heteroatoms.<sup>12</sup> These polymers are often used in high-temperature gas chromatography as thin-film polymer coatings, so-called “stationary phases,” which are coated onto silica capillary column walls. The most frequently used material is poly(dimethylsiloxane), PDMS, although many variations have been invented.<sup>10,13,14,15</sup> These materials are often prepared by typical solvent-based polymerization methods,

which would not be amenable to use with the MMS project, which requires ultrathin coating deposition on wires. However, recently siloxane polymers have been fabricated by advanced chemical vapor deposition methods.<sup>16,17</sup>

Nanolaminates are thin films composed of 2D nanosheets of disparate materials, alternating and often stacked between 5 and 10 sheets thick. Although most nanolaminates have been composed of two different inorganic materials (e.g.  $\text{TiO}_2\text{-Al}_2\text{O}_3$ ,  $\text{HfO}_2\text{-Ta}_2\text{O}_5$ , and  $\text{Al}_2\text{O}_3\text{-silicone}$ <sup>18,19</sup>), a few examples of organic–ceramic nanolaminates exist and are shown in Tables 4.2 (organic component is polymeric) and 4.1 (organic component is non-polymeric). While many of these examples are not desirable for our application because the polymers used are highly unstable to heat, there is one example of a polyimide based nanolaminate: the polyimide– $\text{Ta}_2\text{O}_5$  nanolaminate synthesized by Salmi et al.<sup>20</sup> The polyimide known as Kapton (see Figure 4.6) is desirable because it is one of the most heat-stable polymers. This polyimide– $\text{Ta}_2\text{O}_5$  material is very promising for the MMS application. The dielectric constant of  $\text{Ta}_2\text{O}_5$  is 26. For some MMS applications, a high dielectric constant is appropriate, but for others a low dielectric constant is appropriate. It would therefore be of interest to this project and of value to the literature to produce a nanolaminate whose dielectric constant is lower ( $\lesssim 4$ ). Moreover, Salmi et al.<sup>20</sup> did not study the temperature stability of their materials, so providing a new nanolaminate and studying its thermal properties would be of interest.

As summarized in Table 4.3, organic/inorganic nanolaminates have several advantages over “met-alcones,” namely their higher hydrolytic stability, thermal stability, and broader available range of composition.

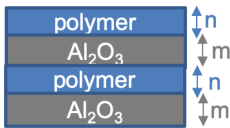
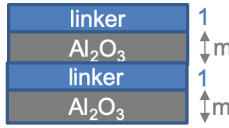
**Table 4.1:** Known vapor processes to prepare organic-inorganic nanolaminate thin films using non-polymer organic components. \*WVTR = water vapor transmission rate.

Ref	Year	Ceramic	Method	Organic	Method	Structure	Mechanical + Moisture Stability
<sup>21</sup>	2013	Alumina, Zinc oxide	ALD	7-octenyl-trichlorosilane	1 dose 7-OTS, then metalorganic precursor		
<sup>22</sup>	2017	Alumina	ALD	7-octenyl-trichlorosilane	1 dose 7-OTS, then metalorganic precursor	10-, 20-, and 40-nm organic layers (contain Si, Al) + 20nm Al <sub>2</sub> O <sub>3</sub> , ×5 dyads	E = 60 - 80 GPa; showed decrease in residual film stress compared to Al <sub>2</sub> O <sub>3</sub> ; WVTR* = 3 × 10 <sup>-7</sup> g/m <sup>2</sup> /day at RT, higher after bending

Table 4.2: Vapor methods for nanolaminates with polymers organic components.

Ref	Year	Ceramic	Method Organic	Method	Structure	Mechanical + Moisture Stability	Electrical + Thermal
23	2008	SiOCH	PECVD plasma-polymerized methylcyclohexane	PECVD	Multilayer stacks of 9 or 13 layers (total thickness 400 nm); 40 nm per material	Water vapor transmission rate (WVTR) was 0.8 g/m <sup>2</sup> /day	Low-K dielectric; Leakage current density = $1 \times 10^{-8}$ - $5 \times 10^{-8}$ A/cm <sup>2</sup> (at E = 1 MV/cm)
20	2009	Tantala	Polyimide (PMDA + DAH)	MLD	5 dyads (10 nm PI + 10 nm tantala), and other structures	Softness, elasticity, and plasticity increase w/ polyimide content	$1 \times 10^{-8}$ A/cm <sup>2</sup> at 1 MV/cm
24	2011	Zinc oxide	Polydiacetylene	1 dose HDD, then UV DEZ	100 nm thick ZnOPDA film	Water mostly on surface of films	Mat'l is an n-type semiconductor; Stable in air up to 400 °C
25	2012	Titania	Polydiacetylene	1 dose HDD, then UV	29-nm thick TiOPDA film (.6 nm TiOPDA + 2.3 nm TiO <sub>2</sub> )		Stable in air up to 400 °C
26	2015	Tantala	Polyimide (PMDA + DAH)	MLD	6 tantala, 6 PI layers, total of 105 nm (each 7.5 nm)		
27	2015	Alumina	PMMA, Novec, PI	Spin-coat	2, 4, or 8 layers, at 6, 12, and 24 nm thickness alumina. Polymer thickness 10 or 20 nm	Critical cracking strain increased by a factor of 2 by incorporation of polymers	Stable in air up to 400 °C

**Table 4.3:** Possible project options. Colors indicate favorable (green), neutral (yellow), and unfavorable (red) factors.  
 \*Dameron et al.<sup>28</sup>

	Polymer-based hybrid nanolaminate	Linker-based hybrid "metalcone"
Picture		
Impact	A few examples known (see Salmi et al.)	~60 examples known (all within last ~10 years)
Ease of fabrication	<ul style="list-style-type: none"> <li>Requires initiation (UV, chemical initiator, or thermal)</li> <li>Coupling chemistry must be well-controlled and matched between 2 materials</li> </ul>	<ul style="list-style-type: none"> <li>Typically <math>T_s</math> between 90 – 350 °C                             <ul style="list-style-type: none"> <li>matches temps of ALD of <math>Al_2O_3</math> from TMA/<math>H_2O</math></li> <li>could match ALD of AlN, above 200 °C</li> </ul> </li> </ul>
Material Properties Mechanical	Likely good – can vary n and m	Likely good (see Dameron et al.)
Ambient stability	Probably OK w/ choice of stable polymer	~ Linkers tend to be labile
Morphology	Unknown	Need to avoid porosity caused by double reactions
Dielectric (after 1000 °C)	Unknown, could be conductive if C content too high	Unknown, could be conductive if C content too high

#### 4.2.4 SPECIFIC AIMS

The specific aims of the research presented in this chapter are:

1. Benchmark the properties and performance of known commercially available CVD dielectrics ( $Al_2O_3$ ,  $AlSiO_x$ , parylene, and polyimide)
2. Design a dielectric material that meets the requirements in Section 4.2.2
3. Design the process chemistry and apparatus to deposit this designed material on substrates of arbitrary geometry
4. Built the apparatus to deposit this material
5. Deposit and characterize dielectric thin films on planar and wire substrates

### 4.3 RATIONALE FOR DESIGN OF HYBRID MATERIAL

In this chapter, our two-fold hypothesis is: (1) A hybrid organic-inorganic nanolaminate material that is thermally stable yet flexible and tough can be made; (2) such a material will meet the requirements of Section 4.2.2. Within the present section, we develop a research project to test these hypotheses. In particular, we first survey existing candidate ceramic (Section 4.3.1) and polymer CVD (Section 4.3.2) processes. We then narrow down from the two surveys by comparing the deposition temperature windows for the process in order to identify material pairs that could be deposited at a common deposition temperature (Section 4.3.3). Having narrowed down to a candidate pair to hybridize, we then consider and develop chemistry to link the two disparate materials.

#### 4.3.1 CERAMIC PROCESSES OVERVIEW

We identified ceramic materials that can be deposited by vapor methods. The following two sections represent reviews of the known vapor methods to deposit two candidate materials: aluminum nitride and aluminum oxide. We focused on these two ceramics over other ceramics that can be vapor-deposited because these vapor processes are well-studied. We do not here provide a full literature review of other ceramics that can be vapor deposited only at very high substrate temperatures above 500 °C, like boron nitride<sup>29</sup> and hafnia,<sup>30</sup> because we hypothesized that these high temperatures would not be commensurate with polymer vapor deposition, since polymers tend to decompose above 500 °C.

#### ALUMINUM NITRIDE

Aluminum nitride (AlN) is a dielectric material with a maximum use temperature of approximately 1370 °C (Figure 4.6). Specifically, in inert atmospheres, it is stable at very high temperatures, melting at 2200 °C. In contrast, in air, surface oxidation occurs above 700 °C. Even at room temperature,

surface oxide layers between 5-10 nanometers can be formed. The oxide protects the material from decomposition in air up to 1370 °C, and above this temperature, the bulk oxidizes. CVD processes to deposit AlN are shown in Table 4.4.

Table 4.4: CVD processes to deposit AlN.

Ref	Year	Method	Precursors		Substrate	Substrate temp (°C)	Bubbler temp (°C)	Carrier gas?	Composition
			Metal	Nonmetal					
<sup>31</sup>	1991	APCVD	Al <sub>2</sub> (NMe <sub>2</sub> ) <sub>6</sub>	NH <sub>3</sub>	Si, vitreous C, glass	200-250	100, 130	He	52-4% Al, 46-8% N, 1-5% O, no C
<sup>32</sup>	2000	CVD	Al <sub>2</sub> (NMe <sub>2</sub> ) <sub>6</sub>	NH <sub>3</sub>	ZnS:Cu phosphor particle	150 - 225	100	N <sub>2</sub>	20% Al, 70% N, 3% O, 4% Zn, 2% S
<sup>33</sup>	1989	CVD	dialkylAl azide			400			
<sup>34</sup>	1989	LPCVD	((CH <sub>3</sub> ) <sub>2</sub> AlNH <sub>2</sub> ) <sub>3</sub>	none		400 - 800	35-60		4-5% O, no C
<sup>35</sup>	1994	MOCVD	Al(CH <sub>3</sub> ) <sub>3</sub>	tBuNH <sub>2</sub>	Si(III) single wafer; glass	400-600	25	H <sub>2</sub>	6% O, 3% C
<sup>35</sup>	1994	MOCVD	Al(CH <sub>3</sub> ) <sub>3</sub>	iPrNH <sub>2</sub>	Si(III) single wafer; glass	400-600	25	H <sub>2</sub>	4% O, 17% C
<sup>36</sup>	1988	CVD	ClAlNH			≥ 450			probably Cl (according to Riedel study)
<sup>37</sup>	1987	CVD	Al(i-C <sub>4</sub> H <sub>9</sub> ) <sub>3</sub>	NH <sub>3</sub>		600 - 1400	200	none; H <sub>2</sub> atmosphere	2-3% C, 4-5% O
<sup>38</sup>	1987	CVD	Al(CH <sub>3</sub> ) <sub>3</sub>	NH <sub>3</sub>	carbon fibers (heated)	900 - 1400	?		<1% C and O



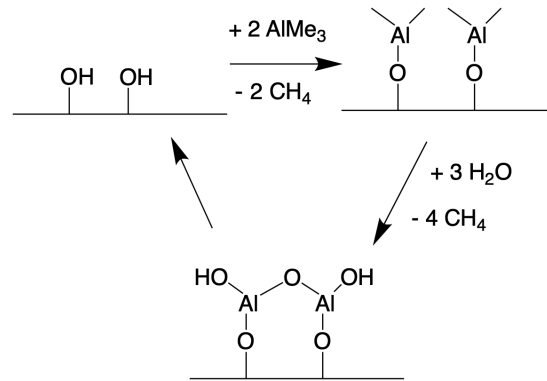


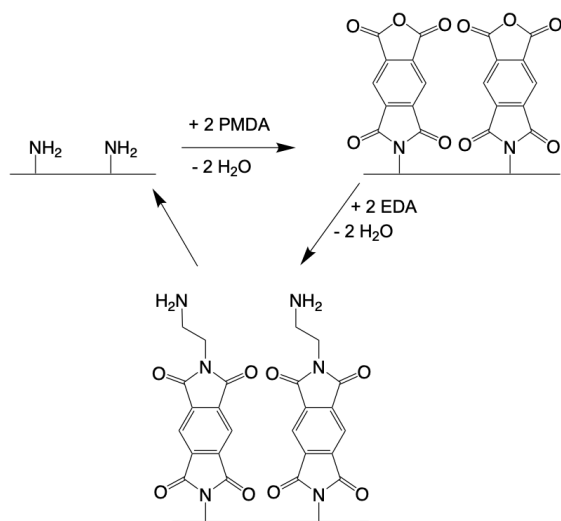
**Figure 4.7:** ALD cycle to produce Al<sub>2</sub>O<sub>3</sub> thin films, described in Miller et al.<sup>39</sup>

## ALUMINUM OXIDE (ALUMINA)

Alumina (Al<sub>2</sub>O<sub>3</sub>) is an electrical insulator with high use temperature of approximately 1800 °C (Figure 4.6). It can be deposited by atomic layer deposition, according to the self-limiting surface termination cycle shown in Figure 4.7. The substrate temperature range at which alumina can be vapor-deposited is 33 °C to 500 °C.<sup>39</sup> As a caveat, the alumina material properties are dependent on deposition temperature, with alumina materials having been deposited at a lower temperature having a higher hydroxyl (as opposed to oxide) content, a compositional feature that affects the film's properties.

### 4.3.2 POLYMERS OVERVIEW

Many polymers can be deposited by vapor deposition.<sup>40,41</sup> To narrow our search, we chose to focus on polymers with high decomposition temperatures, and using this selection criterion would enable us to create a material with higher use temperatures, matching the standards of some applications with respect to thermal cycling. Factors that increase the heat stability of organic polymers are described elsewhere<sup>42,43</sup> and include: aromatic rings, heteroatoms, 2-D or 3-D crosslinking, and

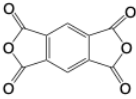
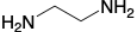
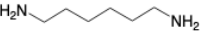
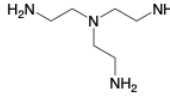
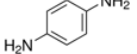
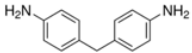
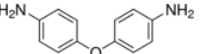
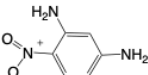


**Figure 4.8:** The mechanism proposed by Putkonen et al.<sup>45</sup> for MLD of PMDA and EDA to form polyimide.

a high degree of crystallinity. We constrained our search to polymers with thermal stability above about 300 °C. Thus, we did not explore the literature on known vapor processes to deposit polyurea, polythiourea, polyurethane, polyazomethine, polyester, or other polymers with relatively low thermal stability; the reader is referred to Zhou et al.<sup>44</sup> for further detail on the vapor deposition of these polymers. Additionally, we excluded from our search polymers that have a high decomposition temperature but for which there do not yet exist chemical vapor deposition processes, for example several siloxane polymers.<sup>15</sup>

Our search for vapor deposition techniques to deposit highly heat-stable polymers resulted in five polymer classes: polyimides (e.g. Kapton), parylenes, polynaphthalenes, polyfluoroethylenes (e.g. Teflon), and siloxanes. The most well-studied of these classes via vapor deposition were the polyimides. The polyimide polymerization process is shown in Figure 4.8. The formation of polyimides relies on a condensation reaction between two components: a dianhydride and a diamine (or, less commonly, a diisocyanate). The most commonly used dianhydride is pyromellitic dianhydride (PMDA), and many diamines have been used, all shown in Table 4.5. The other four classes

**Table 4.5:** MLD processes to deposit polyimides. Data from Putkonen et al.,<sup>45</sup> Salmi et al.,<sup>20</sup> Yoshimura et al.,<sup>48</sup> and González et al.<sup>49</sup>

First Auth	Abrv.	Chemical Name	Structure	T <sub>m</sub> (°C)	T <sub>b</sub> (°C)	T <sub>dub</sub> (°C)
<b>Dianhydride</b>						
Putkonen, Salmi, etc.	PMDA	pyromellitic dianhydride		283	397	~200
<b>Diamines</b>						
Putkonen	EDA	ethylene diamine		8.5	118	25
Salmi	DAH	diaminohexane		39-42	199-204	40
none	TAEA	tris(2-aminoethyl)amine, "tren"		-16	265	unknown
Putkonen	PDA	<i>p</i> -phenylenediamine		138-143	267	100
Putkonen	MDA	methylenedianiline		88-92	249-253	100?
Yoshimura, Putkonen, Gonzalez	ODA	4,4'-oxydianiline		188-192	396.6-397	150
Yoshimura	DNB	2,4-diaminonitrobenzene		161	276	not given

of polymer had less literature precedent in terms of vapor deposition techniques. Methods to make these same polymers were excluded (e.g. vapor phase pyrolysis and redeposition to make Teflon films<sup>46,47</sup>). The vapor deposition processes for parylenes, polynaphthalenes, polyfluoroethylenes, and siloxanes are overviewed in Table 4.6.

#### 4.3.3 MATCHING OF CERAMIC AND ORGANIC PROCESS PARAMETERS

In order to further narrow down the ceramic and organic materials for our hybrid material, we next considered that the reported literature deposition temperatures of the ceramics and polymers may not match. For example, aluminum nitride can only be deposited above 150 °C, but parylene can

**Table 4.6:** MLD processes to deposit polymers.  $T_d$  is the decomposition temperature of the polymer and  $T_{sub}$  is the substrate temperature. Data from Lu et al.,<sup>46</sup> Wary et al.,<sup>50</sup> Lang et al.,<sup>47</sup> Sharangpani et al.,<sup>51,52</sup> and Murthy et al.<sup>16</sup>

1st Auth	Abrv.	Chemical Name	Monomer Structure	Polymer Structure	Proc	$T_d$ (°C)	$T_{sub}$ (°C)
Lu	Parylene-N	Poly(p-xylylene)			MLD	?	~30 to 70
Lu, Wary	Parylene-F (AF)	Poly(tetrafluoro-p-xylylene)			MLD	520-530	~ -15 to 25
Lu, Lang	Polynaphthalene	Poly(naphthalene-N)			VDP	530	350
Lang	Polynaphthalene F	Poly(naphthalene-F)			VDP	138-143	267
Sharangpani	Teflon AF 1600	Teflon AF 1600 (Dupont)			UV + DLI CVD	360	200
Murthy	PV3D3	Poly(1,3,5-trivinyl-1,3,5-trimethylcyclotrisiloxane)			iCVD	?	360-520

**Table 4.7:** Ceramic and polymer vapor deposition process temperature windows.

		T Low	T High	Functionalization
<b>Ceramics</b>	AlN	200	600	N
	Al <sub>2</sub> O <sub>3</sub>	33	500	O
<b>Polymers</b>	PMDA-DAH	160	190	N-O
	PMDA-EDA	160	170	N-O
	PMDA-ODA	160	170	N-O
	PMDA-PDA	160	170	N-O
	PMDA-DNB	50	80	N-O
	P-V3D3	360	520	Si-O
	Teflon	400	450	F
	Polynaphthalene-F	350	370	F
	Teflon AF 1600	200	350	F
	Parylene-F	-20	25	F
	Polynaphthalene-N	350	370	none
	Parylene-N	0	30	none

only be deposited below 30 °C, so it will be impossible to quickly deposit several alternating layers of these two materials. The table of possible substrate temperatures for the CVD ceramic and MLD polymer processes are shown in Table 4.7. We include a column, labeled Functionalization, identifying the heteroatom that reacts during the vapor deposition cycle or, if no heteroatom reacts, the only existing heteroatom in the structure. We hypothesized that matching functionalization between the ceramic and polymer would be advantageous for two reasons: (1) it would increase the probability that the organic and inorganic precursors would react, forming a covalent bond between layers, and (2) a covalent bond between layers would increase adhesion between layers (as opposed to physisorption or other physical, non-chemical interactions between layers).

Thus, although the fluorinated polymers have heat stability, it was difficult to imagine that there would be strong adhesion between Teflon layers and ceramic layers. We focused therefore on the polyimides, because: (1) their nitrogen and oxygen functionalization made them more appealing for reaction with AlN or Al<sub>2</sub>O<sub>3</sub> precursors; (2) there is a wide variety of polyimide chemistries avail-

able via vapor deposition, and (3) polyimide vapor deposition is well-studied and well-established. Polyimide is deposited at temperatures between 160 - 190 °C, but vapor deposition of polyimide at or above 200 °C has not been observed.<sup>45</sup> We next considered which of the two ceramics, AlN or Al<sub>2</sub>O<sub>3</sub>, might be better suited to nanolaminate deposition with polyimides.

Aluminum nitride is typically deposited at high temperatures, between 200 and 600 °C, as shown in detail in Table 4.4 and summarized in Table 4.7. We found one reference which described the deposition of an alumina-like material below 200 °C, but this film, deposited at 150 °C, had a composition that was pure alumina; it contained Zn, O, and S.<sup>32</sup> The lowest-temperature relatively pure AlN films were deposited at 200 °C by Gordon, Hoffman, and Riaz.<sup>31</sup> Therefore, the deposition temperature windows of AlN and polyimide do not overlap.

Aluminum oxide, however, has a wide temperature window between 33 - 500 °C. For this project, we envision depositing an Al<sub>2</sub>O<sub>3</sub>-polyimide nanolaminate at a substrate temperature between 160 - 190 °C, and then annealing the film at 300 °C to drive out water from both layers, fully imidizing the polyimide organic layer and reducing the hydroxyl content of the alumina layer.

#### 4.3.4 SELECTING ORGANIC COMPONENTS

##### CHOOSING POLYIMIDE ORGANIC COMPONENTS

Our next task was to select polyimide monomers. As shown in Figure 4.8 the formation of polyimides relies on a condensation reaction between two components: a dianhydride and a diamine (or, less commonly, a diisocyanate). The most common dianhydrides are pyromellitic dianhydride (PMDA), benzoquinonetetracarboxylic acid dianhydride, and naphthalene tetracarboxylic acid dianhydride. We chose to focus on PMDA because it has been well-established in vapor deposition techniques. To select a diamine for our project, we first considered the properties of several diamines, some of which have previously been used in polyimide vapor deposition, shown in Table

4.5.

One main criterion for diamine selection for this project is the stability of the polymer to heat exposure. As described in Section 4.3.2, the higher the aromatic content and cross-linking of the polymer, typically the more heat-stable. Accordingly, oxydianiline (ODA), methylene diamine (MDA), phenylene diamine (PDA), and diaminobiphenylene (DBP) may provide polyimides that are more heat-stable than the simpler and common ethylene diamine (EDA) would. The thermal stability of polyimide grown using DABP is very high, and those grown using MDA and ODA are also quite high. TAEA has never been used in polyimide to our knowledge, but we imagine cross-linking to enable higher stability than EDA. A second criterion for precursor selection is Young's modulus: the modulus of the PMDA-ODA polyimide is  $\sim 3$  GPa, and those of other polyimides are similar. Another factor in the choice of diamine is the amount of literature precedent for its use and specifically whether it has successfully been used in vapor deposition. Given that this hybrid material is complex, and our project timeline was limited, we desired to use precursors that had previously been reported. ODA and PDA have the most data, while TAEA has not yet been used as a vapor deposition precursor. ODA is a major component of Kapton, the polyimide with the most publicly available data. Given these trade-offs and criteria, we selected the well-studied ODA for the hybrid organic/inorganic material. We also selected TAEA to use in a separate, "polyimide-only" reactor for more exploratory research, in order to hopefully develop a new cross-linked polyimide that could be both a useful material in its own right and a candidate for our hybrid nanolaminate structure. The TAEA research was conducted primarily by Mr. Xian Gong and Mr. Dawei Xi.

Our proposed reaction scheme to produce a hybrid material of PMDA-ODA polyimide and  $\text{Al}_2\text{O}_3$  is shown in Figure 4.9. After deposition of  $m$  organic layers of polyimide, we may end the polyimide layer with a pulse of either ODA or PMDA. In planning the reaction sequence, we hypothesized that surface termination of the previous layer will affect deposition of the subsequent material. Indeed, in studying the literature of hybrid organic-inorganic nanolaminates, we found

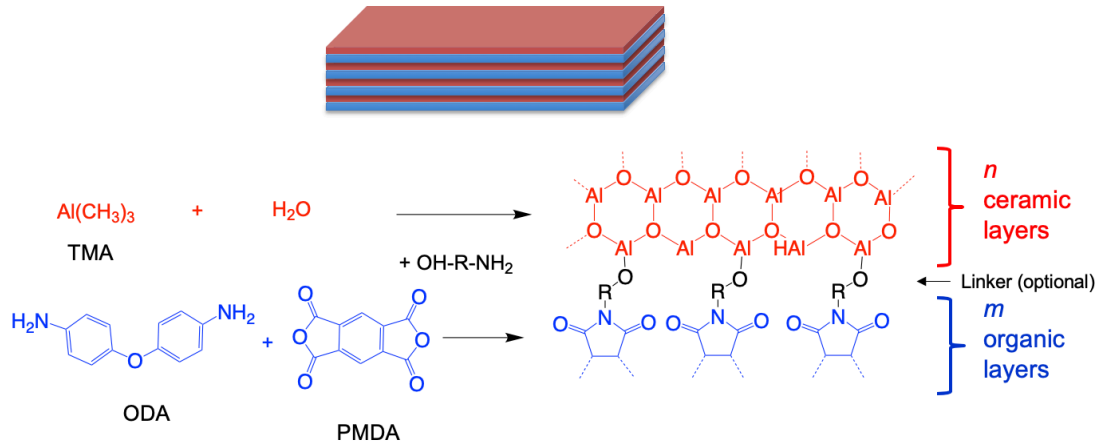


Figure 4.9: Proposed reaction scheme to produce hybrid material.

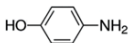
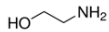
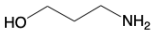
indications that the organic and inorganic layers may not adhere well to each other. For example, Salmi et al. used PMDA and diaminohexane (DAH) as the polyimide precursors. They report that “polyimide growth must be ended with a PMDA pulse. If ended with DAH, the following  $\text{Ta}_2\text{O}_5$  growth was less reproducible. This implies low reactivity of  $\text{Ta}(\text{OEt})_5$  with amine groups.” We may apply these findings to our desired material. We propose an optional linker molecule may promote or enable the growth of the polymer on the ceramic surface and vice-versa, via covalent linkage. In particular, we hypothesize that the following functional groups will be appropriate. Consider a bi-functional linker molecule, which has  $-\text{OH}$  at one site and  $-\text{NH}_2$  at another. As shown in Figure 4.9, this linker should be able to bond to each layer, linking them covalently.

#### LINKER MOLECULE

Considering which linker molecule ( $\text{HO}-\text{R}-\text{NH}_2$ ) would be ideal, we note again that we considered aromatic rings and cross-linkers to increase thermal stability. In addition, in the alucone literature it has been observed that long linkers ( $\geq 6$  carbon aliphatic chains) undergo a “double reaction”: both functional groups can react with the surface, forming a surface bridge that prevents



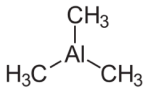
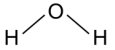
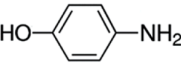
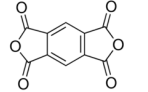
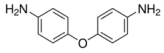
**Table 4.8:** List of candidate linker molecules.

Chemical name	Structure	T <sub>m</sub> (°C)	T <sub>b</sub> (°C)	Appearance
4-aminophenol (4AP)		185-189	284	light brown/beige powder or crystals
ethanolamine		11	170	clear, colorless liquid
3-amino-1-propanol		10	184	colorless viscous liquid

further growth of material up from that site. Moreover, these double reactions create pores, and, because they block a site, they slow or completely destroy film growth. We considered trifunctional linkers which would promote cross-linking, but for simplicity in the first prototype decided to investigate heterobifunctional (O, N) linkers. Another important factor is hydrolytic stability, as linker chemistry has been observed to strongly impact material hydrolytic stability.<sup>53</sup> One proposed solution to this issue is to ensure that the nanolaminate's final, top layer is Al<sub>2</sub>O<sub>3</sub>, which has been used previously as a water barrier layer. Another proposed solution to prevent H<sub>2</sub>O ingress is fluorination or partial fluorination of the linker. However, because fluorination of the linker molecule may also reduce its reactivity with the other precursors, we avoided fluorination in our design. Some linker options are shown in Table 4.8. We decided to use 4-aminophenol (4AP) as our first linker to test for several reasons. It was previously paired with zinc oxide to form a “zincone” by vapor deposition, with a bubbler temperature of 111 °C and a substrate temperature of 220 °C. Its rigidity and aromatic ring make it a candidate for enhanced thermal stability.

In conclusion, we envision selecting PMDA and ODA for initial polyimide depositions, and providing reactor functionality for an optional linker, e.g., 4-aminophenol. Overall, the precursors selected for this project are shown in Table 4.9. The value proposition for this material is shown in Figure 4.10, highlighting that our material may enable access to a previously inaccessible set of characteristics on the Young's Modulus-Temperature stability tradespace. Although we do not expect

Table 4.9: Proposed precursors for this project.

	Role	Abrv.	Chemical Name	Structure	T <sub>m</sub> (°C)	T <sub>b</sub> (°C)	T <sub>bub</sub> (°C)
Al <sub>2</sub> O <sub>3</sub>	Al source	TMA	Trimethylaluminum				25
	O source	H <sub>2</sub> O	Water		0	100	25
	Linker	4AP	4-aminophenol		185-189	284	111
Kapton Poly-imide	Anhydride	PMDA	pyromellitic dianhydride		283	397	200
	Diamine	ODA	4,4'-oxydianiline		188-192	396.6-397.01	150

that the organic component will be fully resistant to decomposition at high temperatures for long, we are targeting use with the EFO spark method as previously described.

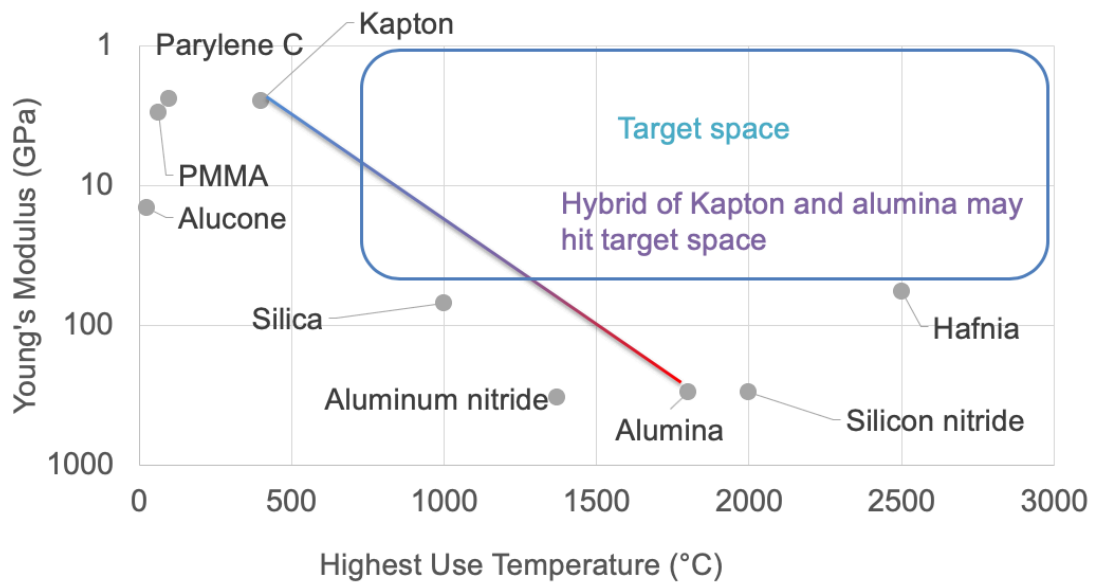


**Figure 4.10:** A hybrid of Kapton polyimide and alumina may have a relatively low Young's modulus (~10-70) but still be resistant to electrical shorting after an EFO spark at 1000 °C. Though the polymer layer may graphitize and become a conductive char, if the alumina layers are intact, then we hypothesize a shorting path will not form through all the dielectric layers, from core metal to shield metal.

#### 4.4 REACTOR APPARATUS

Several low-pressure CVD reactors were used to collect the data in this chapter:

1. *Home-built polyimide reactor*: is described in the PhD dissertation of Dr. Lu Sun.<sup>54</sup> This reactor was modified with a new triamine (TAEA) and then used to deposit PMDA-TAEA polyimide thin films by MLD.
2. *Savannah reactor*: is a Savannah 200 Thermal ALD reactor produced by Veeco/CNT and maintained in the Center for Nanoscale Systems (CNS) at Harvard University. Its reference at the CNS is “ALD-1”. It was used to deposit aluminum silicate thin films.
3. *Parylene reactor*: is a PDS 2010 parylene coater produced by Specialty Coating Systems (SCS) and maintained in the Tufts Micro and Nano Fabrication Facility. It was used to deposit Parylene C.
4. *Home-built hybrid reactor*: was constructed by the author of this thesis for the MMS program. It was used to deposit alumina films, and attempts to deposit polyimide films and hybrid alumina/polyimide films. The design, hardware, and software for this reactor are described in this section.

##### 4.4.1 REACTOR DESIGN AND RATIONALE

We first describe several constraints for reactor design:

1. The reactor must use a finite and preferably limited number of ovens to house and heat the many (at least 4) precursors for this project.

2. Both ODA and PMDA are not very volatile (see Figure 4.16 in Section 4.6) and we proposed that they would need a carrier gas, which requires extra independent carrier gas regulator and lines.
3. It is desired that mutually reactive precursors (like the TMA/water pair or the PMDA/ODA pair) be delivered in separate lines until they reach the reactor furnace. If they pre-mix anywhere, they can react and deposit material, clogging the line or the valves in the line.
4. Precursors should be maintained above their respective “dew points” along the length of the tubing. One way to ensure this constraint is met is to ensure that the precursor flows from lower to higher temperature. This constraint prevents precursors from re-condensing in the lines before reaching the reactor chamber.

The reactor diagram shown in Figure 4.11 was proposed and built after several iterations. The precursor manifold contains three main lines: one for TMA/PMDA, one for ODA/water, and one for the linker molecule. This design allows independent temperature control of the (optional) linker molecule from ODA/PMDA. It is capable of open- and closed-valve operation, and we leak-tested it to an onboard leak rate  $< 4$  mtorr/min. In the next subsections we describe the reactor design choices and apparatus in greater detail.

#### 4.4.2 ELECTRONICS AND SOFTWARE

A python program was written by a previous lab member, Dr. Harbing Lou, to control pneumatic ALD valves. The computer was connected to an Arduino MEGA 2560, which was connected to a breadboard. This breadboard was connected to two six-air-valve assemblies (Humphrey Products, part no. HA040-4E1-PSL, 4 cm) which had Teflon tubing connecting each of the 12 valve air nozzles to one ALD valve. This electronic control system for the pneumatics was constructed in the lab previously.

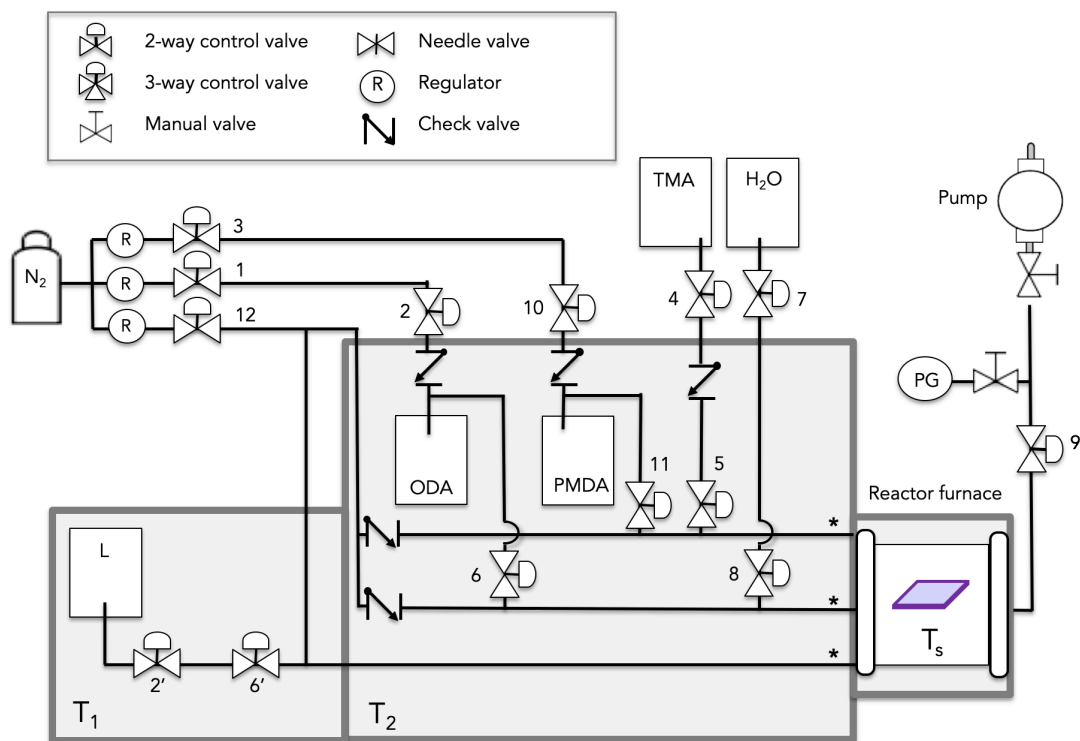


**Figure 4.11:** Hybrid reactor diagram. \*Asterisks are indicated where three one-way valves (aka “check valves”) were installed in an initial iteration of this reactor design, which were removed as described in the text. Although we did not install a linker in the course of the experiments reported in this chapter, we designed the reactor flexibly for potential future incorporation of a precursor into oven #1: the “L” box in oven #1 is a placeholder for a linker molecule, for example 4-aminophenol (4AP).

### 4.4.3 MANIFOLD

#### GAS LINES

A so-called carrier gas is an inert gas (in this case  $N_2$ ) pulsed into a precursor container at higher pressure than the precursor vapor pressure. The carrier gas raises the total pressure in the container, thus enabling the pump to move precursor molecules from the container into the reactor chamber at a higher rate. This effect is quantified in Figure 4.12. It is important in this process that the gases mix thoroughly, so that the gas pumped out from the bubbler contains precursor vapor.

Nitrogen was provided to the reactor via plumbing to house nitrogen which was then purified by Entegris inert gas purifiers (model no. CE500KFL4R) and regulated via an inert gas regulator (Matheson, Airgas, and TESCOM styles were all used). We had the most success with TESCOM single-stage absolute pressure regulators (e.g. model number 64-5040KRT01) because its welded VCR fittings did not leak as easily as other NPT-type fittings (sealed via white Teflon tape) with other regulators.

The precursor lines were made from quarter-inch outer diameter 316 stainless steel tubing. Silver soldering (torch brazing) was used to attach VCR glands to either end of the tubes, which were connected with male/female VCR nuts. Precursors were stored in glass bubblers with airtight copper gaskets and connected via flexible stainless steel tubing to the precursor manifold. The precursor bubblers were maintained at room temperature or oven temperature. Bubbler holders were machined by milling a hole out of  $6'' \times 3''$  rectangular tubing. These holders allowed the bubbler to be suspended so that no part of the glass was touching the oven, thus enabling uniform heating of the bubbler by the oven.

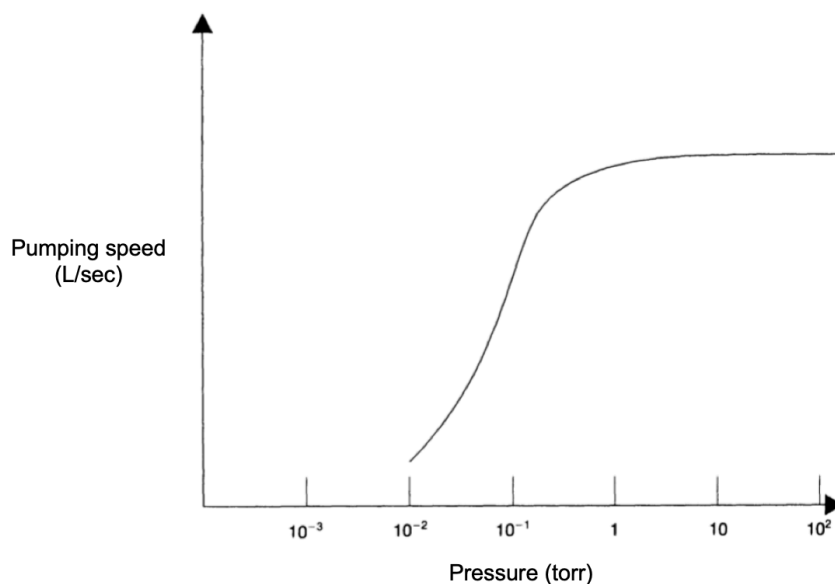


**Figure 4.12:** Pumping speed of a rotary pump is greater with higher gas pressure and lower as the pressure approaches the “ultimate pressure” of the pump. Figure adapted from Sivaram.<sup>55</sup>

## VALVES

Swagelok ALD valves were used to provide pulse gases within the precursor manifold. The typical Swagelok ALD valves are rated to approximately 110 °C, which was appropriate for valves outside the ovens and in the left oven. However, we additionally purchased four high-temperature Swagelok ALD valves (part number SS-HBVVCR4-C) for use inside the right oven, which we expected may need to reach approximately 190 °C to adequately volatilize PMDA and ODA, according to the results in Section 4.6. For all Swagelok ALD valves, Teflon tubing was used to connect the valve to a positive pressure nitrogen manifold.

In the reactor diagram shown in Figure 4.11, asterisks indicate where three one-way valves (aka “check valves”) were installed in an initial iteration of this reactor design. However, when alumina depositions were run in closed-valve mode, Al<sub>2</sub>O<sub>3</sub> deposition inside the check valves caused their malfunction. Accordingly, we proceeded both to remove the (clogged) check valves, and conduct



alumina depositions in open-valve mode, to prevent backflow of gases from the reactor chamber into the precursor manifold lines.

#### 4.4.4 CHAMBER AND EXHAUST

Oven #1 (left of Figure 4.11) was a Yamato DX 300 Gravity Convection Oven. Oven #2 (center of Figure 4.11) was a slightly larger, Yamato DX 400 Gravity Convection Oven. The reactor tube furnace (right of Figure 4.11) was a Lindberg/Blue M three-zone tube furnace. To open and close the exhaust to the chamber, instead of a typical Swagelok ALD valve, an MDC Vacuum large pneumatic butterfly valve was used (model no. 311074, AngleValve, NW40, HV, Pneumatic). The reactor chamber was connected to the pump via stainless steel flexible tubing, 1.5" inner diameter (Kurt J. Lesker bellows tubing 48", part no. MH-QF-C48). The reactor pump was an oil-sealed two-stage rotary vane pump (Edwards RV-12). The reactor pressure gauge was a convection-enhanced Pirani pressure gauge and accompanying electrical readout (Kurt J. Lesker).

### 4.5 MATERIALS AND METHODS

#### 4.5.1 SUBSTRATES

Films were deposited on several substrate types. Two substrate types were purchased: 12.7 mm diameter high purity vitreous carbon planchets (Ted Pella) and 1 × 1 in. Si substrates with a 300-nm surface layer of SiO<sub>2</sub> grown by wet oxidation (University Wafer). We prepared two more substrate types in-house, by adding surface layers to the SiO<sub>2</sub>/Si substrates. Four surface layers were prepared using a Denton E-beam evaporator: 5 nm of Ti or Cr as an adhesion layer were followed by 200 nm of Pt or Au or Cu or Al. Another surface layer we prepared using an STS PECVD<sub>27</sub>: 40 nm of SiN<sub>x</sub> was deposited from 35 sccm SiH<sub>4</sub> and 55 sccm NH<sub>3</sub>, in the presence of 1960 sccm N<sub>2</sub> on high-frequency mode (13.56 MHz), with the power supply at 20 W. The vitreous carbon planchets

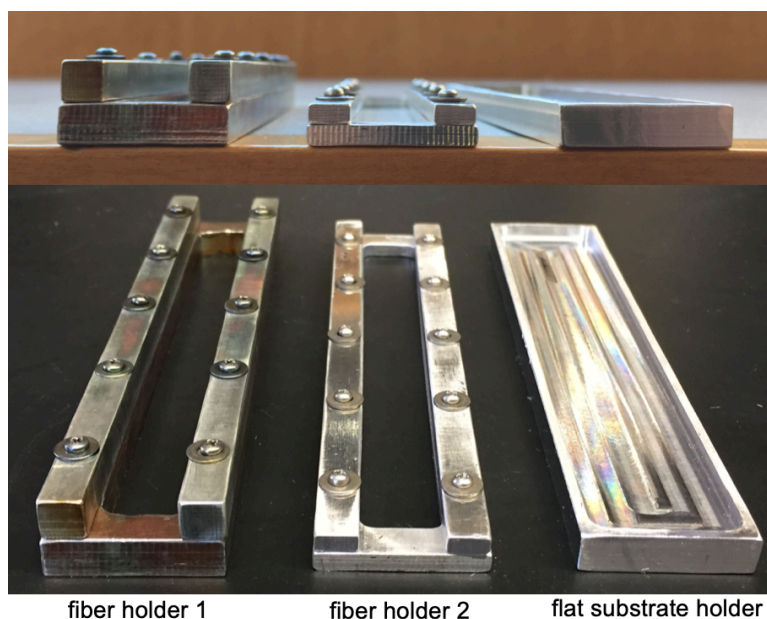


**Figure 4.13:** Several substrate holders were machined to meet the physical requirements of the various deposition chambers. Three are shown here as examples.

received no subsequent treatment prior to CuBr deposition. All of the other 4 substrate types were treated with solvent washes of semiconductor-grade acetone and isopropanol (BDH,  $\geq 99\%$ ). Furthermore, the metal and SiO<sub>2</sub>/Si substrates were then treated with UV-ozone for 5 min to promote the formation of surface hydroxyl groups and clean the surface of organic contaminants.

Several holders were machined to suspend wires to vapor-deposit dielectric coatings coaxially as shown in Figures 4.13 and 4.14.

#### 4.5.2 VAPOR DEPOSITION OF ALUMINUM SILICATE FILMS

Aluminum silicate films were deposited in the Savannah reactor in CNS. Trimethylaluminum (TMA), tris-*tert*-butoxysilanol, and water precursors were dosed using the standard open-valve pulse sequence of 3 cycles per minute with nitrogen purge gas flowing constantly. The outer heater was set to 170 °C and the center heater was set to 200 °C. In this system, TMA and water are held at

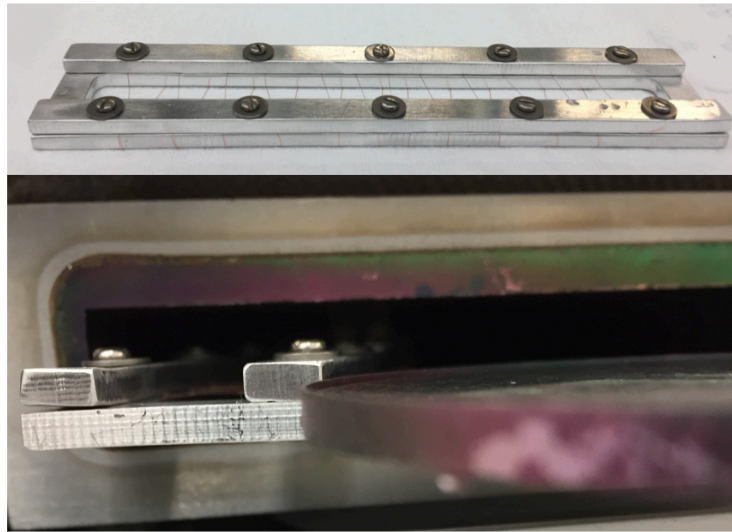


**Figure 4.14:** Wires were suspended on custom built holders and inserted into the various CVD reactors.

room temperature, and the silicon tris-*tert*-butoxysilanol is held at 110 °C.

#### 4.5.3 VAPOR DEPOSITION OF PARYLENE FILMS

The Tufts Micro and Nano Fabrication facility Parylene reactor was used to deposit parylene films. The standard operating procedure is as follows: first the dimer is weighed and placed into the furnace, which heats to 175 °C to vaporize the dimer. Then a furnace pyrolyzes the dimer into the monomer at 690 °C. Then the monomer vapor is released from a “flute” style tube into the coating chamber, which is maintained via 35 °C, where parylene coating occurs. The gases from the chamber pass through a liquid cold trap to re-condense excess material, before reaching the pump and exhaust. Optionally, samples may be pre-treated with a compound promoting parylene adhesion before parylene deposition. This compound is typically a silane such as  $\gamma$ -methacryloxypropyltrimethoxysilane, known also as A-174. Typically, samples are soaked for 5 minutes in a mixture of 100 mL isopropanol, 100 mL of H<sub>2</sub>O, and 1 mL of A-174. The samples must then be rinsed and blown dry.

#### 4.5.4 VAPOR DEPOSITION OF ALUMINA FILMS

Trimethylaluminum (TMA, 97%) was purchased from Sigma-Aldrich and used as received. In a N<sub>2</sub> glovebox, TMA was transferred into a metal bubbler with a glass window. Deionized (DI) water was obtained from the lab DI water tap. Both TMA and H<sub>2</sub>O precursors were stored at room temperature sitting atop the reactor tube furnace in bubbler holders. Alumina films were deposited on thermally-grown SiO<sub>2</sub>/Si substrates. The ALD recipes used to prepare alumina films (200, 400, and 600 cycles) are given in the Appendix and described briefly here:

1. Valves 9 and 12 are open continuously for the entire recipe (“open valve” mode), purging all three manifold lines with nitrogen constantly.
2. Purge N<sub>2</sub> through reactor for 3 hours during furnace warm-up.
3. Open valves 4 and 7 for one second to introduce both TMA and H<sub>2</sub>O into trap volumes.
4. Wait one second to prevent the possibility of ALD valves in the same line being open simultaneously. (Valves 9 and 12 still open: this is a 1-second purge).
5. Open valve 5 for 1 second to introduce TMA into the reactor.
6. Purge for 30 seconds (valves 9 and 12 open).
7. Open valve 8 for 1 second to introduce H<sub>2</sub>O into the reactor.
8. Purge for 60 seconds (valves 9 and 12 open).
9. Repeat *n* times (200, 400, or 600).

#### 4.5.5 VAPOR DEPOSITION OF POLYIMIDE FILMS

All chemicals were purchased from Sigma Aldrich and used as received: 4-aminophenol (4AP,  $\geq 98\%$ ), 4,4'-oxydianiline (ODA) purified by sublimation (99%), pyromellitic dianhydride (PMDA, 97%), and tris(2-aminoethyl)amine (TAEA). Glass bubblers of the chemicals were assembled in a nitrogen glove box using standard bubbler parts (e.g. MDC Vacuum, Cambridge Valve & Fitting).

**PMDA-ODA POLYIMIDE** ODA and PMDA were installed into the hybrid reactor as shown in Figure 4.11. Attempts to grow polyimide films were conducted with substrates of platinum, gold, silicon nitride, and thermally-grown  $\text{SiO}_2/\text{Si}$ . Eight different MLD recipes were used to attempt to prepare PMDA-ODA polyimide films, which are described in Table 4.11 in the Results section.

**PMDA-TAEA POLYIMIDE** Growth of PMDA-TAEA polyimide films was conducted in a dedicated “polyimide reactor.” The layout of this reactor is described in the dissertation of Dr. Lu Sun<sup>54</sup> and it was repurposed to house TAEA by Xian Gong and Christina Chang. In this reactor, the PMDA bubbler was held at 150 °C and the TAEA was held at between 90 °C and 110 °C. Recipes are described in the forthcoming PhD dissertation by Mr. Xian Gong.

#### 4.5.6 CAPACITOR DEVICES

Metal-insulator-metal (MIM) sandwich structures are simple capacitors. This simple device structure enables the detection of leakage current through a dielectric, as well as measurement of the “breakdown voltage” or “breakdown field” of the dielectric. A diagrammatic cross-section of the MIM device is shown in Figure 4.15. First, a conductive silicon wafer ( $1-10 \Omega \cdot \text{cm}$ ) was placed in a thermal evaporation chamber along with copper ingots and a chromium rod. Then, 5 nm of Cr adhesion layer and 200 nm of Cu thin film were evaporated. Next, the dielectric of interest was vapor-deposited. Finally, the MIM structure was completed by thermally evaporating 200 nm-thick

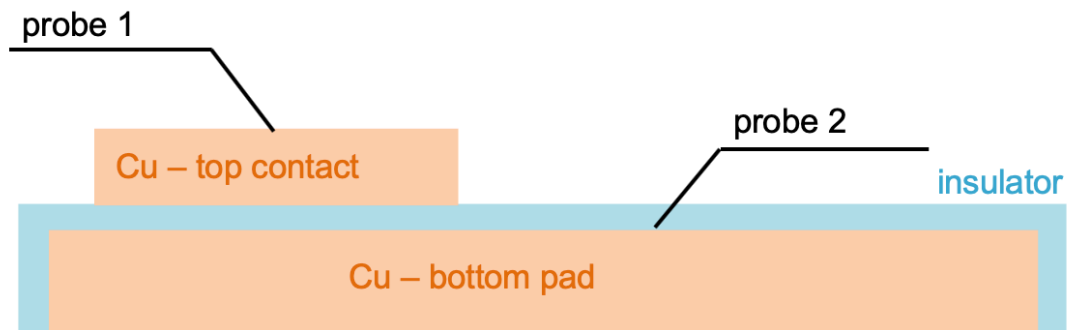


**Figure 4.15:** Metal-insulator-metal device configuration. Probe 1 contacts the top copper layer and probe 2 contacts the bottom copper layer.

Cu contact pads through shadow masks with 4 sizes of pad diameters (0.004", 0.020", 0.015", and 0.020").

#### 4.5.7 CHARACTERIZATION TECHNIQUES

Electron microscopy was performed in a Zeiss Supra 55 scanning electron microscope (SEM). Spectroscopic ellipsometry was performed using a Woollam spectroscopic ellipsometer (WVASE32). X-ray reflectivity (XRR) patterns were recorded in a Bruker D8 Discover X-ray diffractometer using Cu K $\alpha$  radiation ( $\lambda = 1.542 \text{ \AA}$ ). X-ray photoelectron spectroscopy (XPS) was performed on a Thermo Scientific K-Alpha spectrometer equipped with a monochromated Al K $\alpha$  X-ray source, 12 kV electron beam, and Ar<sup>+</sup> sputtering gun. XPS depth profiles were collected by sputtering at 500 eV for 50 seconds per level, unless otherwise stated. Fourier-transform infrared spectroscopy (FTIR) was performed on a Bruker Lumos FT-IR microscope using ATR mode. Leakage current and breakdown voltage measurements were carried out on a 4-point probe station connected to a 4156c parameter analyzer (Keysight Technologies). Finally, two TGA instruments were used to characterize the chemicals used in this chapter:

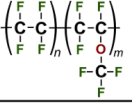
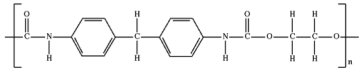
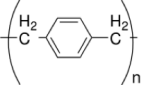
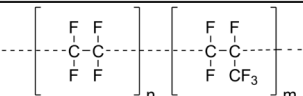
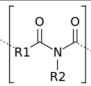
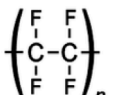
1. Harvard TGA: This is a TA Instruments model Q50, located in a nitrogen glove box, equipped with a nitrogen flow stream.
2. Draper TGA: This is a TA Instruments model Q500, operated by Henry Raczkowski at Draper Laboratory. It is equipped with both air and nitrogen flow streams. Thus, test conditions are either oxidative (40% N<sub>2</sub> and 60% ambient air) or inert atmosphere (100% N<sub>2</sub>).

## 4.6 RESULTS AND DISCUSSION

### 4.6.1 COMMERCIAL WIRE THERMAL DECOMPOSITION CHARACTERIZATION

In order to benchmark the thermal performance of commercially-available polymer coatings on metal wires, a series of six commercial wire samples were obtained, as listed in Table 4.10. TGA was performed at Draper Lab on these six samples by Henry Raczkowski in oxidative mode. The decomposition onset temperatures were estimated from TGA traces and are summarized in Table 4.10. The highest use temperatures in Table 4.10 are all general values, not provided by the manufacturers of the specific wires. Accordingly, we do not necessarily expect the two temperatures to match. Moreover, we expected that the recommended use temperatures would be significantly lower than the onset temperature of decomposition, because users should expect a significant lifetime at any recommended use temperature before decomposition. We found this trend was true for four of the six coatings: polyurethane, Parylene-N, FEP, and PTFE. However, for polyimide and PFA, we found the onset of decomposition temperature according to TGA was lower than the highest reported use temperature. We rationalize these findings as follows. For the CFW polyimide-coated wire, it may be the case that the particular polyimide structure used is not Kapton, whereas we report in Table 4.10 the highest use temperature for Kapton, a very thermally stable polyimide. For the Hitachi PFA-coated wire, the TGA trace feature leading to the identification of the reported onset temperature at 100 °C is most likely adsorbed H<sub>2</sub>O. Overall, among these commercial coatings, PTFE is the most

Table 4.10: TGA results indicating the decomposition onset temperature of 6 commercially available polymer wires.

Polymer	Mfgr	Structure	$T_{d,onset}$ (°C)	$T_{highest\ use}$ (°C)
PFA Perfluoroalkoxy alkane	Hitachi		100	260
Polyurethane	CFW		220	93
Parylene-N	SCS		250	160
FEP Fluorinated ethylene propylene	Alpha		330	200
Polyimide	CFW		340-350	400 (Kapton)
PTFE	Alpha		400	260

thermally stable ( $T_d \approx 400$  °C), and polyimide is second-most stable ( $T_d \approx 340$ - $350$  °C).

#### 4.6.2 ORGANIC PRECURSOR CHARACTERIZATION

Ramp TGA experiments were performed on  $\sim 10$  mg samples of ODA, PMDA, TAEA, and 4-aminophenol (4AP). The temperature was held constant for about 10 minutes in  $10$  °C temperature intervals. We extracted the rate of mass loss at each temperature. As a rule of thumb, solid CVD precursors can be used under conditions where their sublimation rate is greater than about  $0.1$  mg/min; these precursors still typically need a carrier gas. Because sublimation is a thermally activated process, Figure 4.16 and similar plots may be plotted as Arrhenius plots, namely assuming the Arrhenius equation  $k = A \exp(-E_a/RT)$  and plotting  $\ln(k)$  versus  $1/T$ . Because for the purpose of setting up this project, we needed simply to understand at what temperature these chemicals sublime at a rate



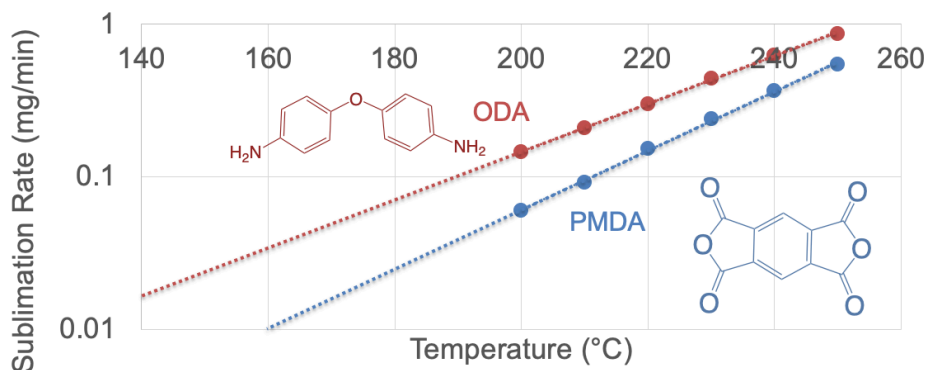


**Figure 4.16:** TGA data analyzed for evaporation rate between 200 and 240 °C for PMDA and ODA precursors.

of about 0.1 mg/min, we do not here provide further analysis of  $k$ .

The ODA and PMDA TGA data are plotted together in Figure 4.16. Based on this plot and the rule of thumb of 0.1 mg/min, we suggest an oven temperature of about 200 °C and carrier gases for both ODA and PMDA. Their similar volatilities indicate that PMDA and ODA may be used in the same oven, informing our hybrid reactor design.

The TGA data for ODA are re-plotted in Figure 4.17 along with TGA data for TAEA for comparison. TAEA is much more volatile, and these results suggest that TAEA can be used without a carrier gas above about 70 °C.

The ramp TGA data and mass loss rate graphs for 4AP are shown in Figure 4.18. The ramp experiment (Figure 4.18 left) is consistent with pure material, because all mass is lost in the experiment with no residue. We also conducted an isothermal stepped experiment on another sample of 4AP, and our analysis (Figure 4.18 right) suggests that 4-aminophenol could be used with a carrier gas at a temperature of about 160 °C. Thus, we suggest that 4AP be stored in a different oven from PMDA and ODA.

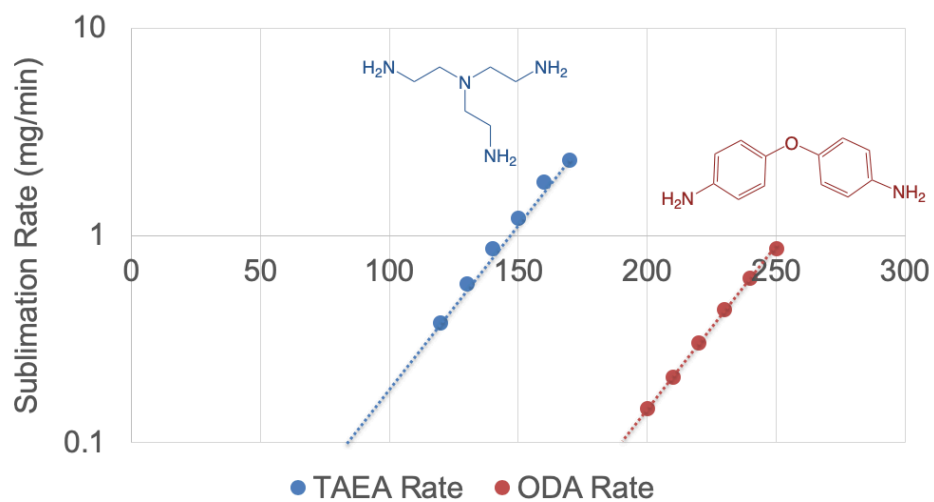


Figure 4.17: TGA data analyzed for evaporation rate for TAEA and ODA precursors.

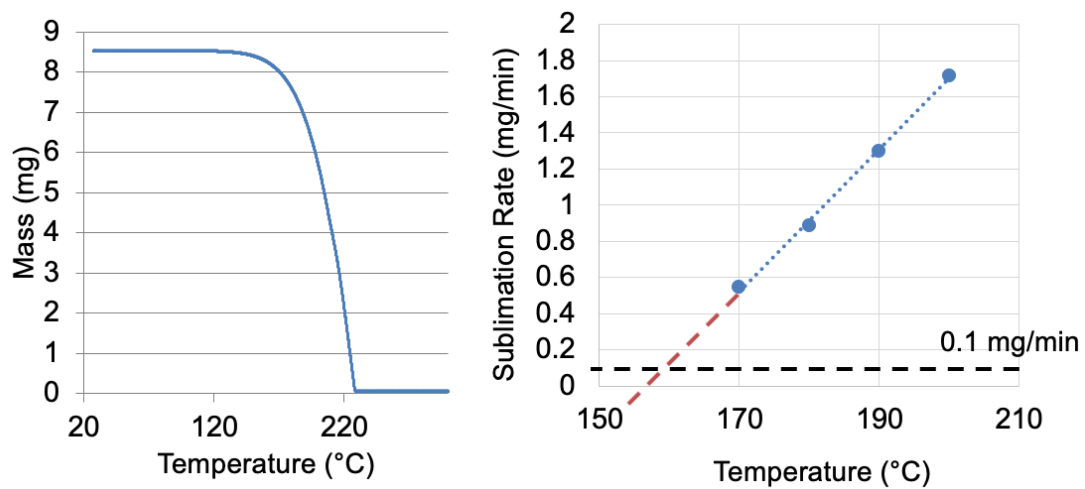


Figure 4.18: TGA ramp and data analyzed for evaporation rate between 170 and 200 °C for 4AP precursor.

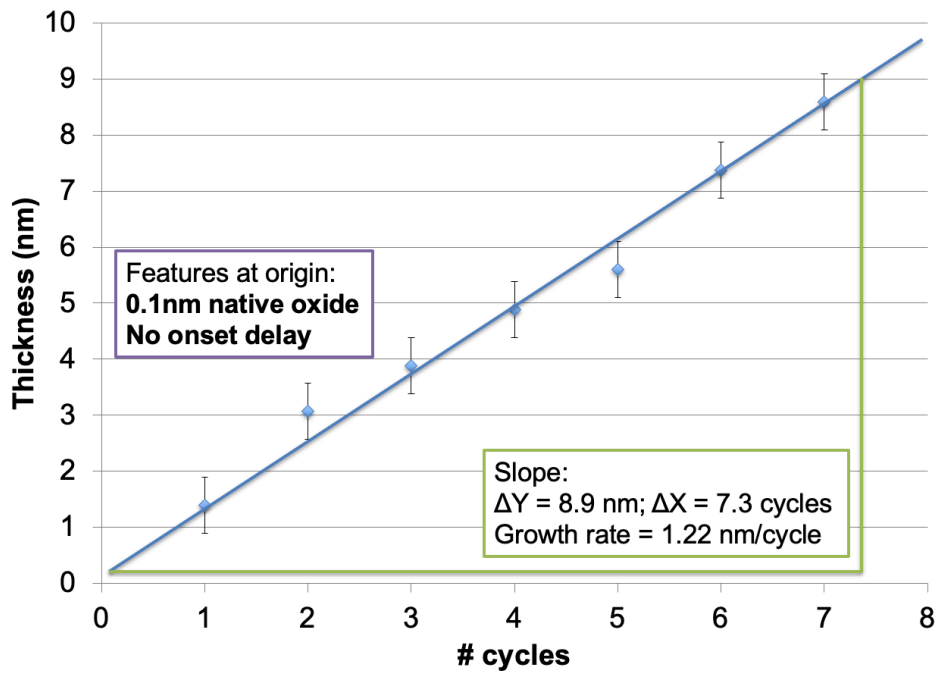
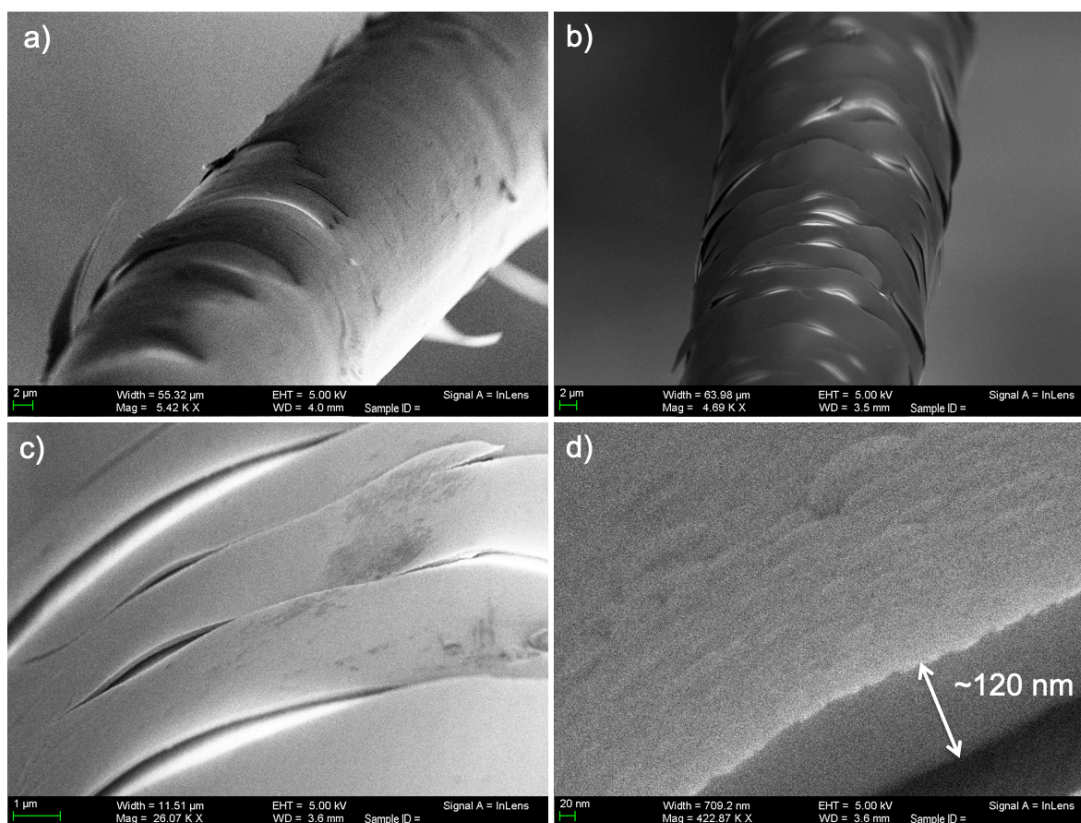


Figure 4.19: Aluminum silicate thin films grown in Savannah reactor indicate a growth rate of 12.2 Å per cycle.

#### 4.6.3 GROWTH CHARACTERISTICS OF ALUMINUM SILICATE FILMS

Aluminum silicate thin films were grown using the Savannah reactor on thermal oxide wafers and copper wires. A range of film thicknesses was first grown on thermal oxide wafers and assessed with spectroscopic ellipsometry to benchmark the film growth per cycle. As shown in Figure 4.19, we extracted a growth per cycle of 12.2 Å per cycle. The y-intercept gave a predeposition film thickness of approximately 0.1 nm, representing the expected  $\sim 1$  Å native oxide, and furthermore implying no delay of growth onset. Our results match the reference growth rate given in the tool standard operating procedure, which is 10-15 Å/cycle.

Because of the known brittleness of ceramics, we expected the aluminum silicate thin films to be inflexible and not to meet the flexibility requirements for the MMS project. We carried out preliminary qualitative mechanical assessment of 120-nm thick aluminum silicate coatings deposited



**Figure 4.20:** 120 nm-thick aluminum silicate thin films were grown on 25 micron diameter Cu wires. SEM micrographs depict cracking in the film after light handling. Image (d) is a close-up of image (c), showing that the cross-sectional thickness of the film is 120 nm.

on bare 25 μm diameter Cu wires. The wires were then dismantled from the custom holder and mounted onto an SEM stub for imaging. Due just to this light handling, cracks formed throughout the thin film coating, as shown in Figure 4.20. These results confirm our expectation that ceramics will be too brittle for the MMS project without an organic component.

#### 4.6.4 GROWTH CHARACTERISTICS OF ALUMINA FILMS

Alumina films were grown in the hybrid reactor at a substrate temperature of 160 °C using the open-valve recipes described in the Materials & Methods (Section 4.5). The film thicknesses were

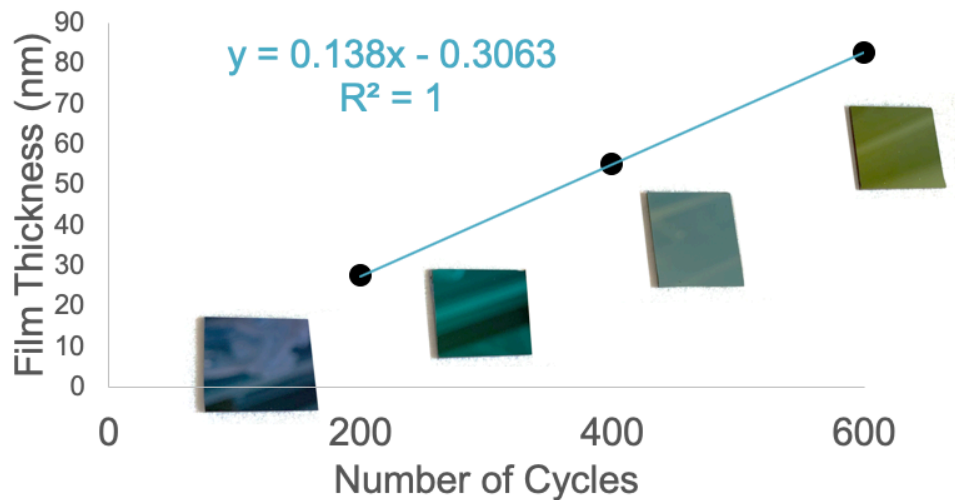


**Figure 4.21:** The thicknesses of three alumina films grown in the hybrid reactor were measured by XRR. We extract a growth per cycle of 1.4 Å per cycle.

measured by XRR. The growth per cycle was 1.4 Å per cycle, as shown in the plot in Figure 4.21. The plot is overlaid with photographs of the bare SiO<sub>2</sub>/Si substrate and three alumina films atop SiO<sub>2</sub>/Si. Although alumina is not a colored material, these films show the expected color change consistent with film growth of thicknesses in the visible light spectral region. XPS depth profiling compositional analysis indicated stoichiometric Al<sub>2</sub>O<sub>3</sub>, as shown in Figure 4.22.

#### 4.6.5 GROWTH OF PMDA-TAEA POLYIMIDE FILMS

PMDA-TAEA polyimide films were grown in the home-built polyimide reactor (described in Section 4.5). This work was done jointly with Mr. Xian Gong. First, a series of PMDA-TAEA films was grown at three different substrate temperatures: 170 °C, 200 °C, and 230 °C. These films were measured by XRR to determine film thickness and calculate growth per cycle, as shown in Figure 4.23a. Growth per cycle monotonically decreased with increasing substrate temperature, consistent with results for other MLD polyimides.<sup>45</sup> Although the reason for this decrease is not commented upon

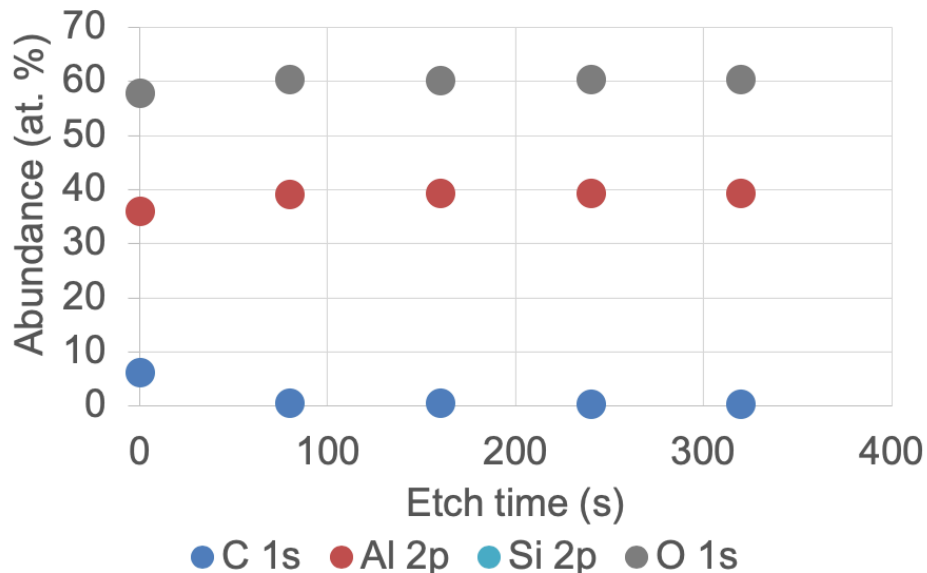


**Figure 4.22:** Alumina thin films grown in hybrid reactor have  $\text{Al}_2\text{O}_3$  stoichiometry, as determined by XPS. Depth profiling was carried out using monatomic Ar sputtering.

in the literature, we presume it may be related to monomer desorption at these higher temperatures, since a low residence time of the monomers on the surface could result in fewer productive polymerization reactions per time. Our substrate temperature tests did not extend below  $170^\circ\text{C}$  because the PMDA is held in an oven at  $170^\circ\text{C}$ . As described earlier, it is undesirable for volatilized precursor gases to re-condense in the reactor, so we chose not to hold the substrate at temperatures lower than  $170^\circ\text{C}$ . Thus, we selected a substrate temperature of  $170^\circ\text{C}$  as our highest growth rate, “optimal” temperature. Next, using a substrate temperature of  $170^\circ\text{C}$ , we systematically varied the TAEA dose time and measured the growth per cycle as a function of TAEA dose time, as shown in Figure 4.23b. This graph is consistent with “saturation,” the expected behavior for surface-limited growth when purging and evacuation of gases occurs in between precursor pulses.

After the films were grown, imidization via annealing was monitored by FTIR, as shown in Figure 4.24. We attribute the disappearance of the broad feature at  $1650\text{ cm}^{-1}$  after annealing to the full

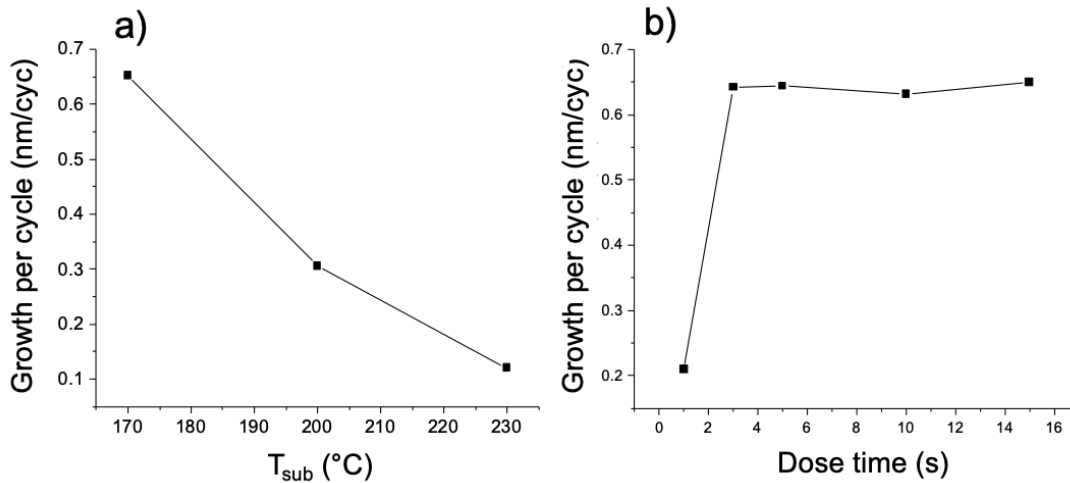


**Figure 4.23:** Growth characteristics of PMDA-TAEA films. (a) Growth per cycle decreases as a function of substrate temperature between  $T_s = 170$  °C to 230 °C; (b) Growth per cycle as a function of TAEA dose time exhibits saturation behavior.

imidization of the film after annealing in  $N_2$  atmosphere for 30 minutes at 350 °C. This evidence is preliminary work and it is our intention to to revisit FTIR characterization in more experimental detail.

#### 4.6.6 GROWTH OF PMDA-ODA POLYIMIDE FILMS

Attempts to grow polyimide films were conducted in the home-built hybrid reactor using the recipes described in Table 4.II. At the bottom of the table is the most highly applicable reference, Putkonen et al.,<sup>45</sup> in which the authors used a very short purge time of between 1-3 seconds, and did not report using a carrier gas, for PMDA and ODA precursors to form polyimide by vapor deposition. Attempting to replicate conditions used by Putkonen and others, we carried out eight different depositions, labeled #1 through #8, each for at least 50 cycles. We evacuated the bubblers after loading to remove headspace nitrogen from the nitrogen glove box. Then, we verified that gas was indeed pulsed into the reactor for all recipes for both precursors, using test pulses and the pressure

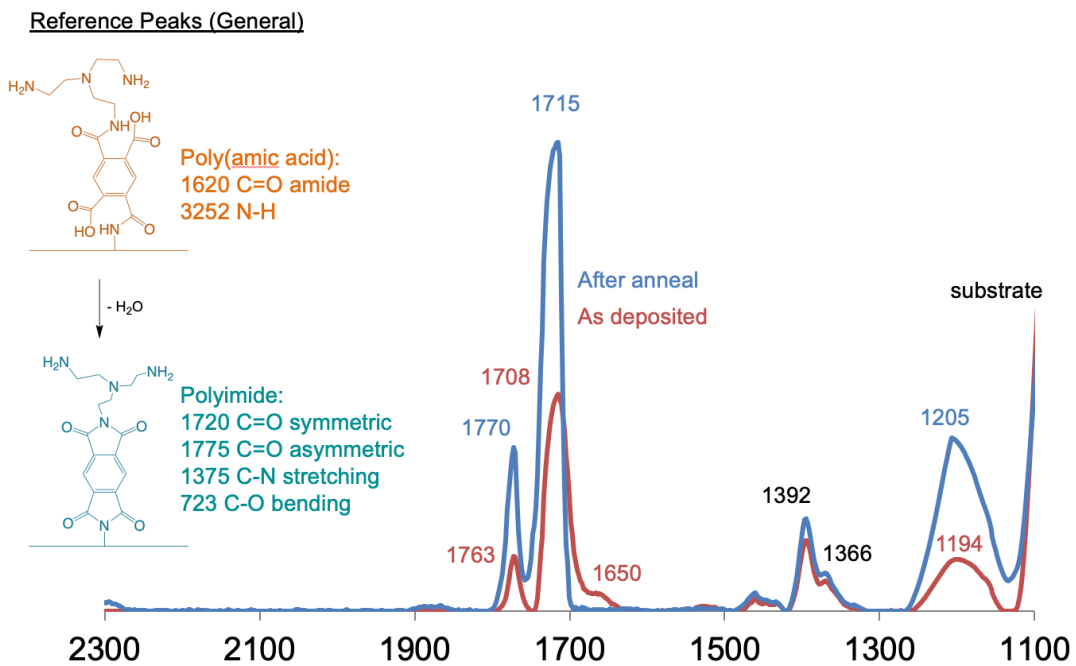


**Figure 4.24:** FTIR spectra of PMDA-TAEA film as-deposited (red) and after 30 minute anneal at 350 °C (blue) for two different films initially made during the same deposition batch. Spectra are un-normalized with arbitrary units. The general frequencies for several bonds in poly(amic acids) (orange) and polyimides (teal) are given for reference.



gauge attached to the reactor chamber. However, this gas is a mixture of carrier gas and, hopefully, precursor vapor. When we conducted control experiments to detect precursor vapor without carrier gas, we detected a very small (on the order of 5 mtorr) pressure rise at the pressure gauge attached to the tube furnace. We further verified the temperature of the oven (150 °C for oven #2) and the reactor tube furnace (160 °C). However, none of our depositions #1-8 produced any polyimide film. We hypothesize that these oven and tube furnace temperatures, although they are consistent with the literature<sup>45</sup> and in the dedicated polyimide reactor, for PMDA-TAEA depositions, may be too low to enable deposition. We base this hypothesis on our TGA data, from which we reason that we should expect less than 0.01 mg/min evaporation of PMDA at 150 °C. Our work is ongoing to deposit PMDA-ODA polyimide, with future directions given in Section 4.7.

#### 4.6.7 ELECTRICAL CHARACTERIZATION OF DIELECTRIC FILMS

Three film types were characterized electrically: aluminum silicate, manganese silicate, and parylene. Aluminum silicate films and parylene films were deposited using the methods described in Section 4.5. Metal-insulator-metal (MIM) capacitor devices were made according to the procedure described in Section 4.5, and the films' leakage current density (J) was measured as a function of applied bias (V). Manganese silicate thin films were deposited by Dr. Lu Sun via methods described in her PhD dissertation.<sup>54</sup> She measured the films' leakage current density versus bias using the same MIM structure and procedure. For all films, J-V curves from the four different contact pad sizes (between 10 to 12 MIM structures per film) were averaged, and the standard deviation in these measurements is given as the error bars in Figure 4.25. Manganese silicate and aluminum silicate perform similarly. For both materials, as expected, the thicker, 400-nm films insulate more strongly than the 130-nm films.

In order to compare the materials, we divide the applied bias by the film thickness to determine the applied electric field in units of V/nm. According to the data in Figure 4.26, at an applied field

Table 4.11: Attempted depositions of PMDA-ODA polyimide.

Deposition ID	Carrier Gas Pressure (torr)	# Exposures per Precursor per Cycle	Exposure Time per Reactant (s)		Purge & Evacuation Time (s)	
			Total	Breakdown	Total	Breakdown
#1	10	1	10	10 s dose	160	40 s purge
				no wait		120 s evac
#8	10	1	15	5 s dose	13	3 s purge
				10 s wait		10 s evac
#2	0.1	1	10	10 s dose	160	40 s purge
				no wait		120 s evac
#4	0.1	3	1	1 s dose	160	40 s purge
				no wait		120 s evac
#3	none	1	1	1 s dose	160	40 s purge
				no wait		120 s evac
#5	none	1	15	5 s dose	30	20 s purge
				10 s wait		10 s evac
#6	none	1	15	5 s dose	30	no purge
				10 s wait		30 s evac
#7	none	1	15	5 s dose	10	no purge
				10 s wait		10 s evac
Putkonen et al.	none	1	3 s PMDA / 2 s ODA		1.3-3.0 s purge	

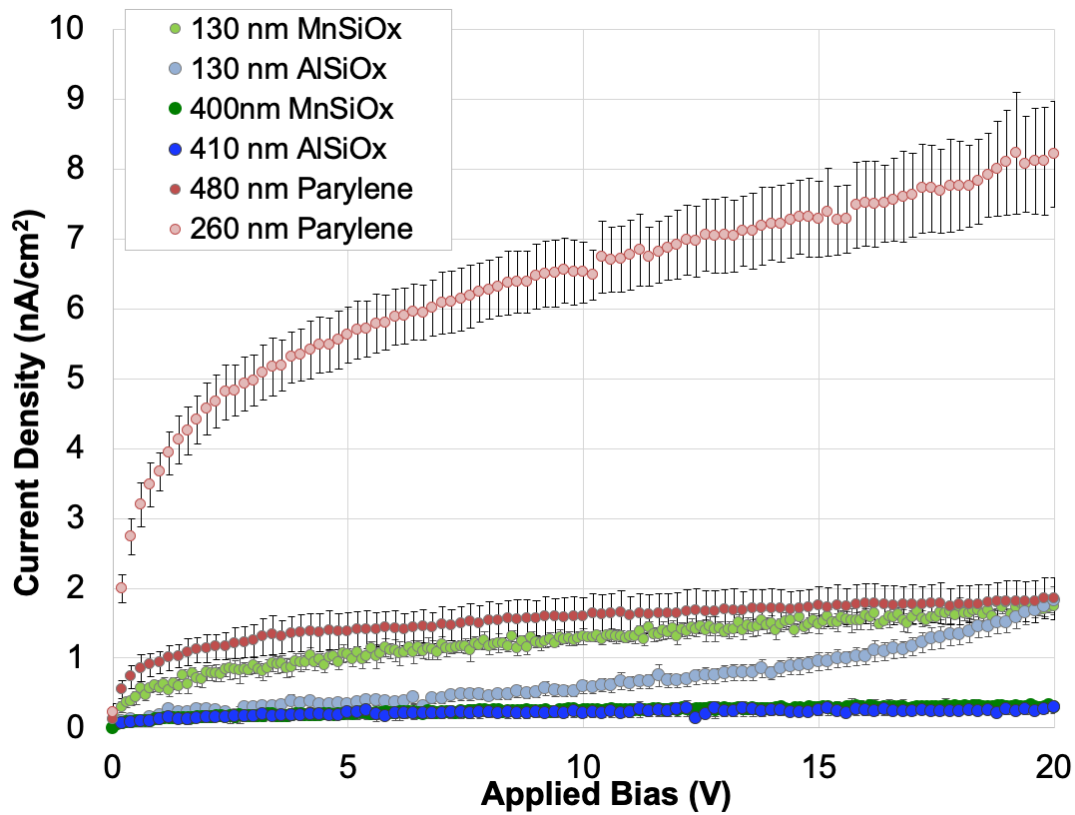


Figure 4.25: Leakage current density through dielectric films as a function of applied bias.

of 2 V/m, parylene experiences a leakage current density of 5.6 nA/cm<sup>2</sup>, whereas aluminum silicate experiences a leakage current density more than an order of magnitude lower, 0.2 nA/cm<sup>2</sup>.

#### 4.6.8 HYBRID FILMS

Work is ongoing to deposit PMDA-ODA polyimide in the hybrid reactor, as will be described in Future Work (Section 4.7). Meanwhile, we used software to predict parameters of interest for the hybrid material. Parameters for the hybrid material were predicted using the CES Selector Software, shown in Figure 4.27. In this software, a 6-layer nanolaminate was modeled consisting of three 10-nm polyimide layers interleaved between three 10-nm alumina layers. Thus, for this modeled mate-

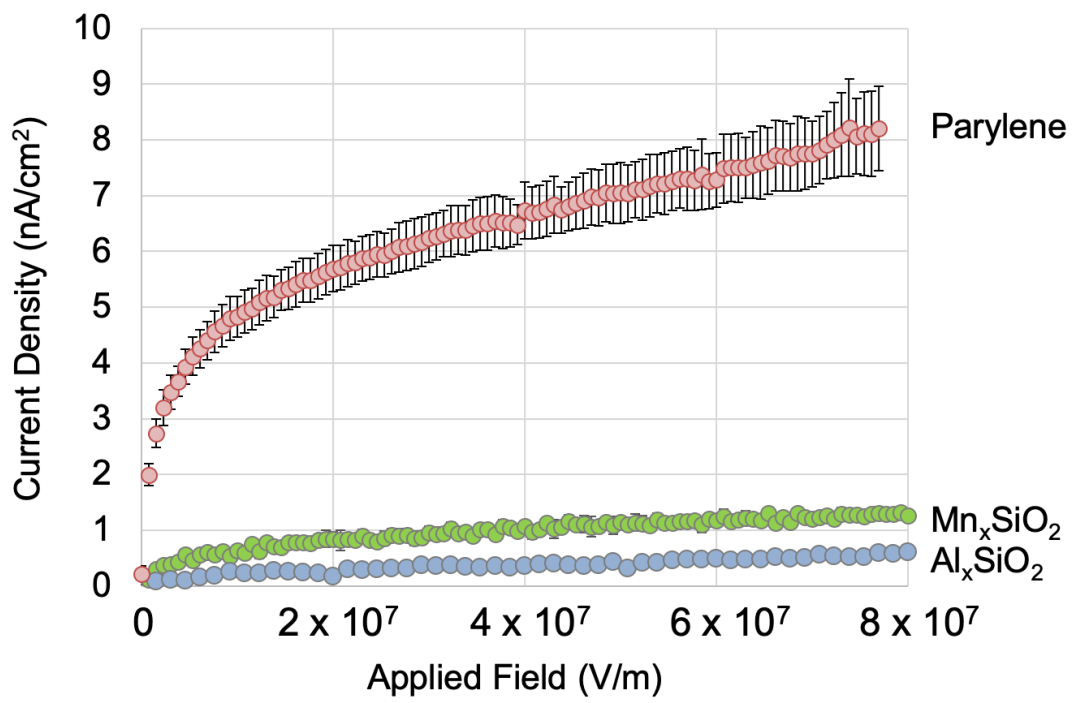


Figure 4.26: Leakage current density through dielectric films as a function of applied field.

rial, the organic:inorganic layer ratio is 1:1 (with respect to layer thickness). The predicted dielectric constant was 7 and the predicted Young's Modulus is 200 GPa.

Based on these predictions, the dielectric constant of the hybrid material is dominated by that of alumina (9.1) as opposed to that of Kapton polyimide (3.9). Similarly, the Young's modulus of the hybrid material is dominated by that of alumina (300 GPa) as opposed to that of Kapton polyimide (2.5 GPa). Returning to the targeted properties for this research project, we desire a relatively flexible material, whose Young's modulus is around 10-70 (see Figure 4.10), while still being resistant to electrical shorting after the EFO spark of 1000 °C. These modeled results suggest that we may target organic:inorganic layer thickness ratios that are higher than 1:1, reducing the Young's modulus from the modeled  $\sim 200$  value to closer to the target  $\sim 10-70$ . There is literature precedent for such tunability of the Young's modulus.<sup>20,56</sup> Future directions for experimental work toward this hybrid nanolaminate material are given in the next section.

#### 4.7 CONCLUSION AND FUTURE WORK

In this chapter, we completed central aspects of each of the Specific Aims listed in Section 4.2.4. A significant portion of the work was to survey and assemble the literature across disparate materials and methods in order to develop a well-formed proposal for a novel hybrid material of interest. We concluded that a PMDA-ODA/ $\text{Al}_2\text{O}_3$  hybrid nanolaminate thin film fabricated via molecular layer deposition/chemical vapor deposition would meet the requirements for our application and add to the field. Another significant portion of the work in this chapter was to build a vapor deposition reactor capable of depositing the desired material. We were able to deposit alumina, and we made some progress toward the deposition of PMDA-ODA polyimide.

There are several future directions that may enable the deposition of PMDA-ODA polyimide. First, the PMDA and ODA precursors may be contaminated or otherwise functioning poorly, and

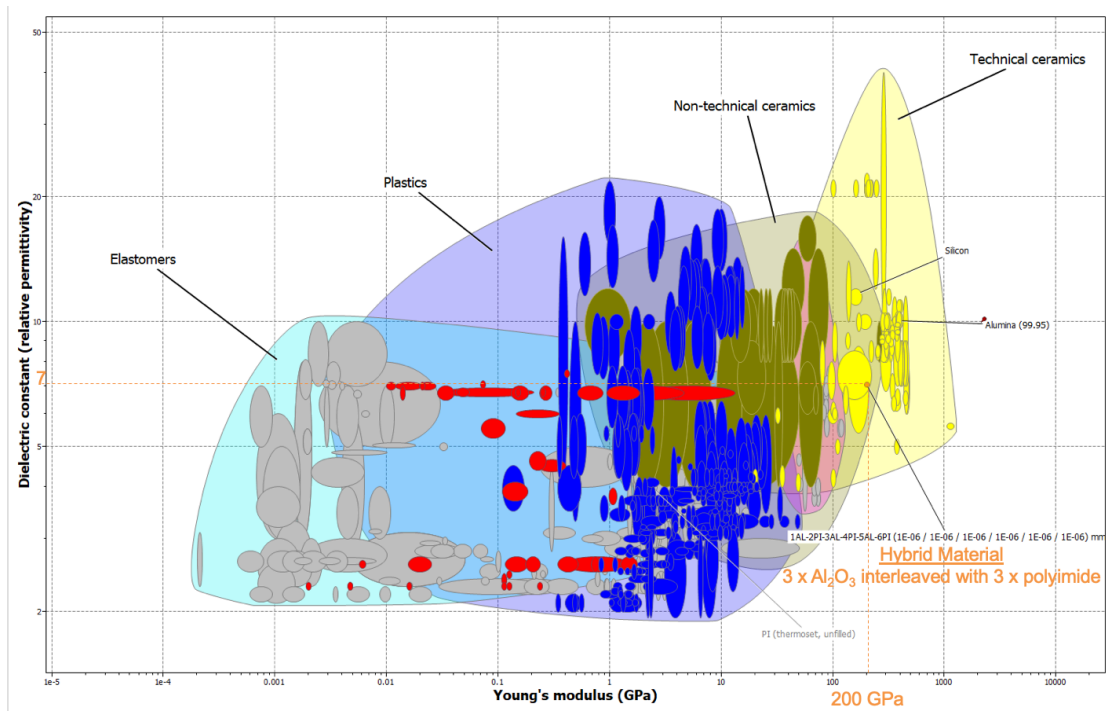


Figure 4.27: Rough estimate of predicted parameters for hybrid material.

we suggest replacing these precursor bubblers with fresh material. Second, it is possible that PMDA and ODA are both entering the reactor furnace but that they react in the first few inches of the reactor chamber before reaching the film. In this case, it may be possible to increase PMDA and ODA coverage by increasing the bubbler temperatures and therefore vapor pressures. We may alternatively extend the sample holder to see if deposition is occurring in this short inlet region. Third, it is possible that our recipe purge times are too long, and the precursors are being entirely removed from the reactor deposition chamber. We find this possibility unlikely, given that the PMDA-TAEA polyimide reactor uses a similar pump and nitrogen (carrier, purge) pressures, and identical pulse sequencing and purge times, and it successfully produced a PMDA-containing polymer material at a range of oven temperatures, including a PMDA precursor temperature of 150 °C. However, each reactor is different, especially with respect to trap volumes and reactor chamber volume, and these parameter differences could give rise to a difference in reactor performance. In a similar vein, a fourth future direction would be to change the carrier gas pressures for the precursors. Both 0.1 torr and 10 torr gas pressures were investigated, in addition to several conditions without carrier gas. Future work could expand the range of explored carrier gas pressures, and, especially, set two different carrier gas pressures for the different precursors. These aforementioned future work suggestions are already being explored by our research team, and we are optimistic that technical troubleshooting will lead to the deposition of PMDA-ODA polyimide via vapor deposition.

After the deposition of PMDA-ODA polyimide is functional, future work would include a detailed study of the polyimide/alumina nanolaminate films. The work plan for the nanolaminate research would include optimization of the growth process, elemental and chemical characterization, thermal characterization, mechanical characterization, and electrical characterization. Growth on both planar and wire substrates will be carried out. Next, each of these future studies is described briefly.

First, the growth process of the hybrid material should be optimized across substrate temper-

atures, gas flow rates, and precursor bubbler temperatures. SEM should be used to indicate film morphology in both plan-view and cross-section. The number of cycles will be varied for each of the two materials, in order to determine the number of cycles that enables full film closure. From SEM cross-section and other thickness measurements (XRR, ellipsometry), the growth rate of the polyimide and of the hybrid materials can be extracted. A wide variety of organic:inorganic cycle ratios should be explored, e.g. from 0% to 25% to 50% to 75% to 100% organic.

Next, elemental and chemical characterization of the films should be carried out on flat substrates. Both high-resolution XPS depth profiling and RBS bulk measurements should be taken to determine the film elemental composition. FT-IR should be conducted to confirm stretching frequencies and the degree of imidization of the film.

Then, thermal and mechanical data should be taken to assess the hybrid material against the commercial materials benchmarked in this chapter. For example, at a variety of organic:inorganic ratios, a film should be deposited and the TGA thermal decomposition profile taken. Mechanical analysis should include the measurement of the Young's modulus: films of a variety of organic:inorganic ratios should be grown to approximately 200 nm thick, and nanoindented 20-100 nm into the film, to extract the Young's modulus. Other mechanical measurements that will be of interest for these materials include tensile strength measurement (Instron), a bend radius test, and thermomechanical analysis (TMA).

Additionally, electrical characterization of the hybrid material will be carried out to assess its performance as a dielectric for the MMS application. Dielectric constant as a function of material ratio will be measured, as well as leakage current density vs. applied bias MIM devices. Reliability testing of MIM devices can also be performed by a "SILC" (stress-induced leakage current) test, in which the film is held at a constant voltage (e.g. approximately 1 V or 10 V) and constant temperature (e.g. 25 °C to 300 °C). A given application of this material may have a set "MALC" (maximum allowable leakage current), and this reliability test can not only determine cumulative charge passed through



the material as a function of time, but also can enable the extraction of the time needed to exceed the MALC, and thus a statistical lifetime of the dielectric layer. Finally, micro-coaxial cable fabrication using the optimized hybrid material, and electrical characterization of this coax, should be carried out in collaboration with Draper Laboratory.

Taken together, these conducted and future work present a compelling path forward for the development of a method to produce hybrid organic-inorganic coatings that may serve as high-temperature stable, flexible dielectric coatings.

## References

- [1] R. L. Crabb and F. C. Treble, "Thin Silicon Solar Cells for Large Flexible Arrays," *Nature*, vol. 213, no. 5082, pp. 1223–1224, Mar. 1967.
- [2] K. A. Ray, "Flexible Solar Cell Arrays for Increased Space Power," *IEEE Transactions on Aerospace and Electronic Systems*, vol. AES-3, no. 1, pp. 107–115, Jan. 1967.
- [3] M. Stoppa and A. Chiolerio, "Wearable Electronics and Smart Textiles: A Critical Review," *Sensors*, vol. 14, no. 7, pp. 11 957–11 992, Jul. 2014.
- [4] W. S. Wong and A. Salleo, Eds., *Flexible Electronics: Materials and Applications*, ser. Electronic Materials : Science & Technology. New York: Springer, 2009, oCLC: ocn403337454.
- [5] R. W. Johnson, M. Strickland, and D. Gerke, "3-D Packaging: A Technology Review," Auburn University, Tech. Rep., 2005.
- [6] C. Gray Haley, A. Duwel, A. Kopa, S. Davis, A. Magyar, B. Smith, M. Meinhold, S. Barron, G. Romano, R. Morrison, and H. Zhang, "Wiring system," United States of America Patent US20 180 098 437A1, 2016.
- [7] M. Meinhold, C. Gray Haley, and S. Barron, "Electric-flame-off stripped micro coaxial wire ends," United States of America Patent WO 2019/036 353, 2017.
- [8] T. D. Burchell, Ed., *Carbon Materials for Advanced Technologies*. Amsterdam ; New York: Pergamon, 1999, oCLC: ocm42274752.
- [9] S. M. George, B. H. Lee, B. Yoon, A. I. Abdulagatov, and R. A. Hall, "Metalcones: Hybrid Organic–Inorganic Films Fabricated Using Atomic and Molecular Layer Deposition Techniques," *Journal of Nanoscience and Nanotechnology*, vol. 11, no. 9, pp. 7948–7955, Sep. 2011.
- [10] G. M. Day, A. I. Hibberd, J. Habsuda, and G. J. Sharp, "Thermally Stable Siloxane Polymers for Gas Chromatography," in *Synthesis and Properties of Silicones and Silicone-Modified Materials*, S. J. Clarson, J. J. Fitzgerald, M. J. Owen, S. D. Smith, and M. E. Van Dyke, Eds. Washington, DC: American Chemical Society, Mar. 2003, vol. 838, pp. 127–136.

- [11] J. Azadmanjiri, C. C. Berndt, J. Wang, A. Kapoor, V. K. Srivastava, and C. Wen, "A review on hybrid nanolaminate materials synthesized by deposition techniques for energy storage applications," *J. Mater. Chem. A*, vol. 2, no. 11, pp. 3695–3708, 2014.
- [12] C. L. Beyler and M. M. Hirschler, "Thermal decomposition of polymers," in *SFPE Handbook of Fire Protection Engineering*, 2nd ed. National Fire Protection Association, 2002, pp. 111–131.
- [13] H. D. Zhu, S. W. Kantor, and W. J. MacKnight, "Thermally Stable Silphenylene Vinyl Siloxane Elastomers and Their Blends," *Macromolecules*, vol. 31, no. 3, pp. 850–856, Feb. 1998.
- [14] F. Gao, F. Huang, L. Tang, and L. Du, "Synthesis and characterization of poly (multidimethylsiloxane-1, 4-ethynylenephenyleneethynylene) s," *Polymer journal*, vol. 43, no. 2, pp. 136–140, 2011.
- [15] P. R. Dvornic and R. W. Lenz, "Exactly alternating silarylene—siloxane polymers: 6. Thermal stability and degradation behaviour," *Polymer*, vol. 24, no. 6, pp. 763–768, Jun. 1983.
- [16] S. K. Murthy, B. D. Olsen, and K. K. Gleason, "Initiation of Cyclic Vinylmethylsiloxane Polymerization in a Hot-Filament Chemical Vapor Deposition Process," *Langmuir*, vol. 18, no. 16, pp. 6424–6428, Aug. 2002.
- [17] W. E. Tenhaeff and K. K. Gleason, "Initiated and Oxidative Chemical Vapor Deposition of Polymeric Thin Films: iCVD and oCVD," *Advanced Functional Materials*, vol. 18, no. 7, pp. 979–992, Apr. 2008.
- [18] S. K. Sahoo, R. P. Patel, and C. A. Wolden, "Hybrid nanolaminate dielectrics engineered for frequency and bias stability," *Journal of Applied Physics*, vol. 114, no. 7, p. 074101, Aug. 2013.
- [19] R. P. Patel, D. Chiavetta, and C. A. Wolden, "Dielectric performance of hybrid alumina-silicone nanolaminates synthesized by plasma enhanced chemical vapor deposition," *Journal of Vacuum Science & Technology A: Vacuum, Surfaces, and Films*, vol. 29, no. 6, p. 061508, Nov. 2011.
- [20] L. D. Salmi, E. Puukilainen, M. Vehkamäki, M. Heikkilä, and M. Ritala, "Atomic Layer Deposition of Ta<sub>2</sub>O<sub>5</sub>/Polyimide Nanolaminates," *Chemical Vapor Deposition*, vol. 15, no. 7-9, pp. 221–226, Sep. 2009.
- [21] J. Huang, M. Lee, A. Lucero, and J. Kim, "Organic-Inorganic Hybrid Nano-laminates Fabricated by Ozone-assisted Molecular-atomic Layer Deposition," *Chemical Vapor Deposition*, vol. 19, no. 4-6, pp. 142–148, Jun. 2013.
- [22] K. H. Yoon, H. S. Kim, K. S. Han, S. H. Kim, Y.-E. K. Lee, N. K. Shrestha, S. Y. Song, and M. M. Sung, "Extremely High Barrier Performance of Organic–Inorganic Nanolaminated Thin Films for Organic Light-Emitting Diodes," *ACS Applied Materials & Interfaces*, vol. 9, no. 6, pp. 5399–5408, Feb. 2017.

- [23] S. M. Park, D. J. Kim, S. I. Kim, and N.-E. Lee, "Single-chamber plasma enhanced chemical vapor deposition of transparent organic/inorganic multilayer barrier coating at low temperature," *Journal of Vacuum Science & Technology A: Vacuum, Surfaces, and Films*, vol. 26, no. 4, pp. 949–955, Jul. 2008.
- [24] S. Cho, G. Han, K. Kim, and M. M. Sung, "High-Performance Two-Dimensional Polydiacetylene with a Hybrid Inorganic–Organic Structure," *Angewandte Chemie International Edition*, vol. 50, no. 12, pp. 2742–2746, Mar. 2011.
- [25] K.-H. Yoon, K.-S. Han, and M.-M. Sung, "Fabrication of a new type of organic-inorganic hybrid superlattice films combined with titanium oxide and polydiacetylene," *Nanoscale Research Letters*, vol. 7, no. 1, p. 71, 2012.
- [26] A. Autere, L. Karvonen, A. Säynätjoki, M. Roussey, E. Färm, M. Kemell, X. Tu, T. Liow, G. Lo, M. Ritala, M. Leskelä, S. Honkanen, H. Lipsanen, and Z. Sun, "Slot waveguide ring resonators coated by an atomic layer deposited organic/inorganic nanolaminate," *Optics Express*, vol. 23, no. 21, p. 26940, Oct. 2015.
- [27] R. Lewis, J. Slaughter, and Y. C. Lee, "Improved Flexibility of Alumina Ultrathin Barrier Films by Nano-Lamination," in *Volume 2: Advanced Electronics and Photonics, Packaging Materials and Processing; Advanced Electronics and Photonics: Packaging, Interconnect and Reliability; Fundamentals of Thermal and Fluid Transport in Nano, Micro, and Mini Scales*. San Francisco, California, USA: ASME, Jul. 2015, p. V002T02A030.
- [28] A. A. Dameron, D. Seghete, B. B. Burton, S. D. Davidson, A. S. Cavanagh, J. A. Bertrand, and S. M. George, "Molecular Layer Deposition of Alucone Polymer Films Using Trimethylaluminum and Ethylene Glycol," *Chemistry of Materials*, vol. 20, no. 10, pp. 3315–3326, May 2008.
- [29] J.-S. Li, C.-R. Zhang, B. Li, F. Cao, and S.-Q. Wang, "Boron nitride coatings by chemical vapor deposition from borazine," *Surface and Coatings Technology*, vol. 205, no. 12, pp. 3736–3741, Mar. 2011.
- [30] T. S. Yang, K.-S. An, E.-J. Lee, W. Cho, H. S. Jang, S. K. Park, Y. K. Lee, T.-M. Chung, C. G. Kim, S. Kim, J.-H. Hwang, C. Lee, N.-S. Lee, and Y. Kim, "Chemical Vapor Deposition of  $\text{HfO}_2$  Thin Films Using the Novel Single Precursor Hafnium 3-Methyl-3-pentoxide,  $\text{Hf}(\text{mp})_4$ ," *Chemistry of Materials*, vol. 17, no. 26, pp. 6713–6718, Dec. 2005.
- [31] R. G. Gordon, D. M. Hoffman, and U. Riaz, "Atmospheric pressure chemical vapor deposition of aluminum nitride thin films at 200–250 C," *Journal of materials research*, vol. 6, no. 1, pp. 5–7, 1991.
- [32] K. A. Klinedinst and R. F. Clark, "Nitride coated particle and composition of matter comprised of such particles," US Patent 6 064 150, May, 2000.

- [33] D. C. Boyd, R. T. Haasch, D. R. Mantell, R. K. Schulze, J. F. Evans, and W. L. Gladfelder, "Organometallic azides as precursors for aluminum nitride thin films," *Chemistry of Materials*, vol. 1, no. 1, pp. 119–124, 1989.
- [34] X. Chen, L. Liu, P. Y. Yu, and S. S. Mao, "Increasing Solar Absorption for Photocatalysis with Black Hydrogenated Titanium Dioxide Nanocrystals," *Science*, vol. 331, no. 6018, pp. 746–750, Feb. 2011.
- [35] A. C. Jones, J. Auld, S. A. Rushworth, D. J. Houlton, and G. W. Critchlow, "Investigations into the growth of AlN by MOCVD using tri-tert butylaluminium as an alternative aluminium source," *Journal of Materials Chemistry*, vol. 4, no. 10, p. 1591, 1994.
- [36] D. M. Schleich, "Method for production of high purity aluminum nitrides," US Patent 4 767 607, Aug., 1988.
- [37] K. Tsuchida, Y. Takeshita, A. Yamane, and A. Kato, "Preparation of AlN Powders by Vapor Phase Reaction of Al(iBu)<sub>3</sub>-NH<sub>3</sub> System," *Yōgho Kyokaishi*, vol. 95, pp. 1198–1201, 1987.
- [38] B. Armas and C. Combescure, "Chemical Vapor Deposition of Si<sub>3</sub>N<sub>4</sub> and AlN on Carbon-Fibers," *Proc. 10th Int. Conf. CVD*, p. 1060, 1987.
- [39] D. C. Miller, R. R. Foster, S.-H. Jen, J. A. Bertrand, S. J. Cunningham, A. S. Morris, Y.-C. Lee, S. M. George, and M. L. Dunn, "Thermo-mechanical properties of alumina films created using the atomic layer deposition technique," *Sensors and Actuators A: Physical*, vol. 164, no. 1-2, pp. 58–67, Nov. 2010.
- [40] K. K. Gleason, Ed., *CVD Polymers: Fabrication of Organic Surfaces and Devices*. Weinheim: Wiley-VCH-Verl, 2015, oCLC: 897131556.
- [41] V. J. B. J. Kumar and M. Bergkvist, "CVD Polymers for the Semiconductor Industry," *CVD Polymers: Fabrication of Organic Surfaces and Devices*, pp. 391–414, 2015.
- [42] S. D. Bruck, *Thermally Stable Polymeric Materials*. ACS Publications, 1965.
- [43] P. J. DiNunno, N. F. P. Association, and Society of Fire Protection Engineers, Eds., *SFPE Handbook of Fire Protection Engineering*, 2nd ed. Quincy, Mass: NFPA, National Fire Protection Ass, 1995, oCLC: 635607232.
- [44] H. Zhou and S. Bent, "Fabrication of Organic Interfacial Layers by Molecular Layer Deposition: Present Status and Future Opportunities," in *CVD Polymers: Fabrication of Organic Surfaces and Devices*. John Wiley & Sons, 2015.
- [45] M. Putkonen, J. Harjuoja, T. Sajavaara, and L. Niinistö, "Atomic layer deposition of polyimide thin films," *J. Mater. Chem.*, vol. 17, no. 7, pp. 664–669, 2007.

- [46] T. M. Lu and J. A. Moore, "Vapor deposition of low-dielectric-constant polymeric thin films," *MRS Bulletin*, vol. 22, no. 10, pp. 28–31, 1997.
- [47] C. I. Lang, G. R. Yang, J. A. Moore, and T. M. Lu, "Vapor Deposition Of Very Low K Polymer Films, Poly(Naphthalene), Poly(Fluorinated Naphthalene)," *MRS Proceedings*, vol. 381, Jan. 1995.
- [48] T. Yoshimura, S. Tatsuura, and W. Sotoyama, "Polymer films formed with monolayer growth steps by molecular layer deposition," *Applied Physics Letters*, vol. 59, no. 4, pp. 482–484, Jul. 1991.
- [49] J. P.-P. González, A. Lamure, and F. Senocq, "Polyimide (PI) films by chemical vapor deposition (CVD): Novel design, experiments and characterization," *Surface and Coatings Technology*, vol. 201, no. 22-23, pp. 9437–9441, Sep. 2007.
- [50] J. Wary, R. Olson, and W. Beach, "Vacuum-Deposited Parylene AF-4: A Thermally Stable, Low Dielectric Constant Polymer for Interlayer Dielectric Use," *1996 Proceedings, Second International Dielectrics for VLSI/ULSI Multilevel Interconnection Conference*, pp. 207–213, Feb. 1996.
- [51] R. Sharangpani and R. Singh, "Chemical Vapor Deposited Teflon Amorphous Fluoropolymer as an Interlevel Dielectric Material for Low Power Integrated Circuits," *MRS Proceedings*, vol. 476, Jan. 1997.
- [52] —, "A Comparative Study of Spin-On and Chemical Vapor Deposited Teflon Amorphous Fluoropolymer Thin Films," *Journal of the Electrochemical Society*, vol. 144, no. 8, pp. 2924–2928, 1997.
- [53] Y. Wada, K. Iyoki, A. Sugawara-Narutaki, T. Okubo, and A. Shimojima, "Diol-Linked Microporous Networks of Cubic Siloxane Cages," *Chemistry - A European Journal*, vol. 19, no. 5, pp. 1700–1705, Jan. 2013.
- [54] L. Sun, "Atomic Layer Deposition of Manganese Silicate, Molecular Layer Deposition of Polyimide and Their Applications," PhD Dissertation, Harvard University, Sep. 2018.
- [55] S. Sivaram, *Chemical Vapor Deposition: Thermal and Plasma Deposition of Electronic Materials*. Springer Science & Business Media, 1995, oCLC: 913809655.
- [56] B. H. Lee, B. Yoon, V. R. Anderson, and S. M. George, "Alucone Alloys with Tunable Properties Using Alucone Molecular Layer Deposition and Al<sub>2</sub>O<sub>3</sub> Atomic Layer Deposition," *The Journal of Physical Chemistry C*, vol. 116, no. 5, pp. 3250–3257, Feb. 2012.

**T**HIS DISSERTATION WAS TYPESET  
using L<sup>A</sup>T<sub>E</sub>X, originally developed by  
Leslie Lamport and based on Donald  
Knuth's T<sub>E</sub>X. The body text is set in 11 point  
Egenolff-Berner Garamond, a revival of Claude  
Garamont's humanist typeface.